

# Probing gravity waves in the middle atmosphere using infrasound from explosions

Ekaterina Vorobeva<sup>1</sup>, Jelle Daniel Assink<sup>2</sup>, Patrick Joseph Espy<sup>1</sup>, Toralf Renkwitz<sup>3</sup>, Igor Petrovich Chunchuzov<sup>4</sup>, and Sven Peter Näsholm<sup>5</sup>

<sup>1</sup>Norwegian University of Science and Technology

<sup>2</sup>KNMI

<sup>3</sup>Leibniz-Institute of Atmospheric Physics (LG)

<sup>4</sup>Institute of Atmospheric Physics

<sup>5</sup>NORSAR

February 27, 2023

## Abstract

This study uses low-frequency, inaudible acoustic waves (infrasound) to probe wind and temperature fluctuations associated with breaking gravity waves in the middle atmosphere. Building on an approach introduced by Chunchuzov et al., infrasound recordings are used to retrieve effective sound-speed fluctuations in an inhomogeneous atmospheric layer that causes infrasound backscattering. The infrasound was generated by controlled blasts at Hukkakero, Finland and recorded at the IS37 infrasound station, Norway in the late summers 2014 - 2017. Our findings indicate that the analyzed infrasound scattering occurs at mesospheric altitudes of 50 - 75 km, a region where gravity waves interact under non-linearity, forming thin layers of strong wind shear. The retrieved fluctuations were analyzed in terms of vertical wave number spectra, resulting in approximate  $kz$ -3 power law that corresponds to the “universal“ saturated spectrum of atmospheric gravity waves. The  $kz$ -3 power law wavenumber range corresponds to vertical atmospheric scales of 33 - 625 m. The fluctuation spectra were compared to theoretical gravity wave saturation theories as well as to independent wind measurements by the Saura medium-frequency radar near Andøya Space Center around 100 km west of IS37, yielding a good agreement in terms of vertical wavenumber spectrum amplitudes and slopes. This suggests that the radar and infrasound-based effective sound-speed profiles represent low- and high-wavenumber regimes of the same “universal“ gravity wave spectrum. The results illustrate that infrasound allows for probing fine-scale dynamics not well captured by other techniques, suggesting that infrasound can provide a complementary technique to probe atmospheric gravity waves.

# Probing gravity waves in the middle atmosphere using infrasound from explosions

Ekaterina Vorobeva<sup>1,2</sup>, Jelle Assink<sup>3</sup>, Patrick Joseph Espy<sup>1</sup>, Toralf Renkowitz<sup>4</sup>,  
Igor Chunchuzov<sup>5</sup>, Sven Peter Näsholm<sup>2,6</sup>

<sup>1</sup>Department of Physics, Norwegian University of Science and Technology, Trondheim, Norway

<sup>2</sup>NORSAR, Kjeller, Norway

<sup>3</sup>R&D Seismology and Acoustics, Royal Netherlands Meteorological Institute (KNMI), De Bilt, The

Netherlands

<sup>4</sup>Leibniz Institute of Atmospheric Physics, University of Rostock, Kühlungsborn, Germany

<sup>5</sup>Obukhov Institute of Atmospheric Physics, Moscow, Russia

<sup>6</sup>Department of Informatics, University of Oslo, Oslo, Norway

## Key Points:

- Ground-based infrasound recordings of explosions are used to retrieve effective sound speed fluctuations in the mesosphere
- Vertical wave number spectra of the retrieved fluctuations agree with the “universal” gravity wave saturation spectrum
- Infrasound from 49 explosions and radar data show that remote sensing of the middle atmosphere is possible via ground-based infrasound data

---

Corresponding author: Ekaterina Vorobeva, [ekaterina.vorobeva@ntnu.no](mailto:ekaterina.vorobeva@ntnu.no)

**Abstract**

This study uses low-frequency, inaudible acoustic waves (infrasound) to probe wind and temperature fluctuations associated with breaking gravity waves in the middle atmosphere. Building on an approach introduced by Chunchuzov et al., infrasound recordings are used to retrieve effective sound-speed fluctuations in an inhomogeneous atmospheric layer that causes infrasound backscattering. The infrasound was generated by controlled blasts at Hukkakero, Finland and recorded at the IS37 infrasound station, Norway in the late summers 2014 – 2017. Our findings indicate that the analyzed infrasound scattering occurs at mesospheric altitudes of 50 – 75 km, a region where gravity waves interact under non-linearity, forming thin layers of strong wind shear. The retrieved fluctuations were analyzed in terms of vertical wave number spectra, resulting in approximate  $k_z^{-3}$  power law that corresponds to the “universal” saturated spectrum of atmospheric gravity waves. The  $k_z^{-3}$  power law wavenumber range corresponds to vertical atmospheric scales of 33–625 m. The fluctuation spectra were compared to theoretical gravity wave saturation theories as well as to independent wind measurements by the Saura medium-frequency radar near Andøya Space Center around 100 km west of IS37, yielding a good agreement in terms of vertical wavenumber spectrum amplitudes and slopes. This suggests that the radar and infrasound-based effective sound-speed profiles represent low- and high-wavenumber regimes of the same “universal” gravity wave spectrum. The results illustrate that infrasound allows for probing fine-scale dynamics not well captured by other techniques, suggesting that infrasound can provide a complementary technique to probe atmospheric gravity waves.

**Plain Language Summary**

This study analyzes inaudible acoustic waves (infrasound) detected in Norway following explosions during disposal of military equipment in Finland. We show that infrasound reflects off small-scale structures in the middle atmosphere (within 50-75 km altitude) and we use signals recorded to retrieve so-called effective sound-speed profiles, a proxy of small-scale variations in temperature and horizontal wind. Spectral analysis of the retrieved altitude profiles reveals a power law associated with gravity waves. Such waves are important in the transfer of energy between atmospheric layers and are generated, for example, by upward air flow over mountain ranges. The vertical scales to which infrasound is sensitive to, are estimated to range from 33 to 625 m. Comparisons between spectra obtained using radar and infrasound show good agreement in terms of amplitudes and slopes. This suggests that the radar and infrasound-based effective sound-speed profiles represent different regimes of the same “universal” gravity wave spectrum. This study uses a large, consistent infrasound dataset and independent radar data to show that remote sensing of fine-scale wind and temperature variations in a region of the middle atmosphere for which very few observations are available, is possible by means of ground-based infrasound measurements.

**1 Introduction**

This study investigates the use of acoustic waves to probe fine-scale wind and temperature structures of the middle atmosphere (i.e. stratosphere and lower mesosphere). Atmospheric infrasound, i.e. low-frequency sound waves in the inaudible frequency range (< 20 Hz) can be generated by both natural (e.g., volcanoes, earthquakes, thunder) and artificial (e.g., rocket launches, sonic booms, blasts) sources. Once generated, infrasound waves can propagate in the atmosphere over long distances as the energy is ducted by waveguides formed by vertical gradients in temperature and wind (Brekhovskikh, 1960; Diamond, 1963). In addition to the source characteristics, infrasound waves also provide information about the medium through which they propagate, and can therefore serve

68 as a tool for atmospheric remote sensing (e.g., Le Pichon et al., 2005; Assink et al., 2019;  
69 Smets & Evers, 2014; Chunchuzov et al., 2022).

70 Probing the middle atmosphere by means of ground- and space-based remote sens-  
71 ing techniques contributes to a better representation of this region in atmospheric mod-  
72 els. The latter allows for improved weather forecasts due to the dynamical coupling be-  
73 tween different atmospheric layers (Shaw & Shepherd, 2008). The resolution of the at-  
74 mospheric model products, and therefore the scales of atmospheric processes resolved,  
75 strongly depends on available computational capabilities and the scientific problem. For  
76 example, high-resolution limited-area models routinely in use at national meteorologi-  
77 cal services (e.g., Bengtsson et al., 2017) have high horizontal resolution of several kilo-  
78 meters, however, the model top is typically in the lower stratosphere ( $\sim 10$  hPa, or 30  
79 km). In contrast, global numerical weather prediction models (NWP) and general cir-  
80 culation models (GCMs) with model tops raised into the mesosphere and above (Stocker  
81 et al., 2014) have lower resolution and are unable to resolve atmospheric processes at scales  
82 smaller than 10 kilometers in operational NWP (Bauer et al., 2015) and tens of kilome-  
83 ters in GCMs (H.-L. Liu et al., 2014; Becker et al., 2022). While not fully resolvable by  
84 models, these subgrid-scale processes can be observed by various observational techniques,  
85 including radar, lidar and rocket measurements (Rapp & Lübken, 2004; Le Pichon et al.,  
86 2015; Schäfer et al., 2020; Strelnikov et al., 2019).

87 One such subgrid-scale phenomenon is atmospheric gravity waves (GWs). Gener-  
88 ated in the lower atmosphere, GWs propagate into the middle atmosphere with increas-  
89 ing amplitude due to the decrease in air density with altitude, until they ultimately be-  
90 come unstable and break. When breaking, GWs generate small-scale eddies or turbu-  
91 lence which in turn interact with other atmospheric waves (Fritts & Alexander, 2003).  
92 The transfer of energy and momentum between different atmospheric layers is an im-  
93 portant function of atmospheric waves. For example, the middle atmospheric meridional  
94 circulation is primarily GW-driven (Fritts & Alexander, 2003) and breaking mesospheric  
95 GWs play an important role in the wintertime polar stratospheric downward motion (Garcia  
96 & Boville, 1994; Wicker et al., 2023). Momentum deposited by GWs (or GW drag) can  
97 modify atmospheric circulation patterns at lower altitudes, therefore affecting the weather  
98 and its prediction (McFarlane, 1987). This highlights the need for GW probing and for  
99 improvement of GW representation in NWP and GCMs. Efforts are also being made to  
100 develop GW-resolving GCMs stretching up to the edge of the thermosphere (e.g. H.-L. Liu  
101 et al., 2014; Becker et al., 2022).

102 GWs interact with other atmospheric waves in various ways, including wave-wave  
103 interaction and wave-breaking (Fritts & Alexander, 2003), and cause the presence of lo-  
104 calized, three-dimensional small-scale fluctuations in temperature and wind fields. These  
105 have been observed in the middle atmosphere by in-situ, ground- and space-based in-  
106 struments (e.g., Fritts & Alexander, 2003; Tsuda, 2014; Selvaraj et al., 2014; Bossert et  
107 al., 2015; Miller et al., 2015; Podglajen et al., 2022). The vertical scales of these fluctu-  
108 ations are significantly smaller than the horizontal scales, and have characteristic ver-  
109 tical length scales ranging from tens of meters to tens of kilometers (Gardner et al., 1993).  
110 The presence of such small-scale atmospheric fluctuations is known to affect propaga-  
111 tion and scattering of infrasound waves (Chunchuzov & Kulichkov, 2020). Moreover, it  
112 has been demonstrated by Bertin et al. (2014) and Lalande and Waxler (2016) that in-  
113 frasound waveguides are very sensitive to GW induced small-scale fluctuations in wind  
114 and temperature (see also Brissaud et al. (2023)). This implies the importance of account-  
115 ing for fine-scale atmospheric structures when modelling infrasound propagation (Drob  
116 et al., 2013; Hedlin & Drob, 2014; Chunchuzov et al., 2022). On the other hand, this also  
117 suggests that infrasound observations can be used to probe small-scale atmospheric fluctu-  
118 ations, thereby addressing the need for an enhanced observations of GWs (Cugnet et  
119 al., 2019).

The purpose of the current study is to quantify GW activity using a dataset of infrasound recordings from distant ground-based explosions. These signals have been recorded at a ground-based microbarometer array in Norway, every day during the period of mid-August to mid-September for the years 2014-2017. We apply a method that allows for the retrieval of so-called effective sound speed fluctuations in an inhomogeneous layer in the middle atmosphere. The method was developed over several years by Chunchuzov (2002); Chunchuzov et al. (2013, 2015, 2022); Chunchuzov and Kulichkov (2020). Based on the retrieved effective sound speed fluctuations for each event, we calculate the corresponding vertical wavenumber spectrum, and further interpret this in terms of power spectral density (PSD) slope and amplitude. The retrieved GW spectra are further compared to independent wind radar observations as well as to both linear and non-linear theoretical GW saturation models (Dewan & Good, 1986; S. A. Smith et al., 1987; Chunchuzov et al., 2015).

We exploit an infrasound dataset of signals generated by ground-based blasts in Hukkakero, Finland. These signals are detected at 321 km distance from the source, at microbarometer array IS37 in Northern Norway. This dataset has several attractive features making it suitable for atmospheric probing studies. First, the explosive events take place during August and September which is during the atmospheric transition from summer to winter, when the zonal component of the stratospheric winds reverses from westward to eastward (Waugh & Polvani, 2010; Waugh et al., 2017). Second, the known locations of the source and receiver together with the transient nature of the blasts make it possible to clearly identify arrivals from both stratospheric and from mesospheric – lower thermospheric (MLT) altitudes. Finally, yet importantly, the recurring nature of explosive events allows us to study day-to-day variability of the middle atmosphere dynamics.

The paper is organized as follows. A background on infrasound sensitivity to atmospheric structure, infrasound signal processing terminology, and previous studies exploiting Hukkakero explosion-related data is provided in Sect. 2. Section 3 describes the infrasound dataset, signal pre-processing, the SD-WACCM-X atmospheric model used, and the ray-tracing simulations conducted. Its subsection 3.4 elaborates the effective sound speed retrieval methodology. The obtained results are shown in Sect. 4, also further discussed in Sect. 5 including vertical wavenumber spectrum comparison to independent radar measurements and theoretical models.

## 2 Background

### 2.1 Sensitivity of infrasound to atmospheric structure

Infrasound propagation is sensitive to spatial variations in temperature and wind (e.g., Waxler & Assink, 2019). In the direction of propagation, the wind and temperature related propagation effects can approximately be modelled using the concept of effective sound speed,  $C_{\text{eff}}(z)$ , defined as:

$$C_{\text{eff}}(z) = \sqrt{\gamma RT} + \mathbf{u} \cdot \hat{n}, \quad (1)$$

where,  $\gamma$ ,  $R$ ,  $T$ ,  $\mathbf{u}$  and  $\hat{n}$  correspond to the adiabatic index, the gas constant, the absolute temperature, the horizontal wind speed vector and the direction of propagation, respectively. In the infrasound-related context, it is often appropriate to approximate  $\sqrt{\gamma R} \approx 20 \text{ m s}^{-1} \text{ K}^{-1/2}$ . For cases where ground-to-ground propagation is of interest, it is convenient to introduce the effective sound speed ratio, which is obtained by normalizing  $C_{\text{eff}}(z)$  by its value on the ground and which is analogous to the more familiar refractive index. From classical ray theory, acoustic signals that originate from the ground are expected to traverse in waveguides between the ground and the altitudes for which the  $C_{\text{eff}}$  ratio exceeds unity.

164 The celerity is defined as the source-receiver great-circle distance divided by the  
 165 infrasound travel time (i.e., the difference between the arrival time and origin time). The  
 166 celerity can hence be considered as the average group speed of a guided acoustic wave.  
 167 When the origin time and location are known, celerity-based models can be used to pro-  
 168 vide information about the infrasound waveguide through which an acoustic wave prop-  
 169 agated. Infrasonic paths with a substantial vertical component have a group speed that  
 170 is significantly lower than the speed of sound. Conversely, infrasound guided by tropo-  
 171 spheric waveguides (that propagates in the troposphere) has a celerity near the local sound  
 172 speed. Typical celerities for different waveguides are 310–330 m/s for tropospheric ar-  
 173 rivals, 280–320 m/s for stratospheric arrivals, and 180–310 m/s for mesospheric and  
 174 thermospheric arrivals (e.g., Nippress et al., 2014; Lonczaga, 2015).

## 175 2.2 Infrasound array processing

176 An infrasound array is a group of microbarometers distributed in space but installed  
 177 close enough so that the received sensor signals are sufficiently coherent to estimate the  
 178 wavefront parameters of the dominant plane wave arriving at the array. This is done us-  
 179 ing array signal processing techniques that delay and sum sensor traces according to a  
 180 model for the inter-element delays. This spatial filtering allows for reducing incoherent  
 181 noise and for separating acoustic signals from different directions of arrival. Identifica-  
 182 tion of the signals of interest is typically based on the observed back-azimuth, apparent  
 183 velocity, and average inter-sensor coherence. The back-azimuth represents the direction  
 184 from which the plane wave arrives at the array and is measured in degrees clockwise from  
 185 the North. The apparent velocity is the velocity the plane wave appears to travel at hor-  
 186 izontally along the array. This parameter is estimated based on the time delays between  
 187 sensors (as well as back-azimuth) and contains information about the angle of incidence  
 188  $\theta$  of the plane-wave,  $v_{\text{app}} = c / \sin \theta$  where  $c$  is the local sound speed. There is no unique  
 189 relationship between apparent velocity and altitude from which signal arrives, however  
 190 higher values of apparent velocity would normally indicate arrival from higher altitudes.  
 191 The combination of back-azimuth and travel time allows for signal identification and in-  
 192 frasound source location, while  $v_{\text{app}}$  helps to identify the incidence angle of the ray-path  
 193 at the ground.

## 194 2.3 The Hukkakero blasts in infrasound studies

195 The site of Hukkakero, Finland (67.94° N, 25.84° E; Fig. 1), has been of particu-  
 196 lar interest for infrasound related studies over the past years. At Hukkakero, blasts re-  
 197 lated to the disposal of military explosives occur yearly since 1988 in August-September,  
 198 typically once a day with a yield of around 20 tons of TNT equivalent (Gibbons et al.,  
 199 2015). In addition to generating an atmospheric pressure wave, these explosions produce  
 200 clear seismic signals which allow for the accurate estimation of origin time and location  
 201 by means of seismic localization techniques (Gibbons et al., 2020). Blixt et al. (2019)  
 202 showed that the ARCES seismic array in northern Norway records, besides the seismic  
 203 waves also the ground-coupled airwaves associated with Hukkakero explosions. These  
 204 explosions are also well-represented in event bulletins like the comprehensive European  
 205 Infrasound Bulletin (Pilger et al., 2018, Fig. 10), as well as in the Comprehensive Nuclear-  
 206 Test-Ban Treaty (CTBT) bulletin products.

207 Infrasound signals that originated from Hukkakero explosions have been exploited  
 208 in several atmospheric probing studies. Blixt et al. (2019) analyzed 30 years of Hukkakero  
 209 explosions detected at the ARCES/ARCI seismo-acoustic array (Norway) in terms of back-  
 210 azimuth deviation due to cross-wind (the component of wind perpendicular to the di-  
 211 rection of propagation) influence along the propagation path. The resulting cross-wind  
 212 estimates obtained showed a good agreement with the European Centre for Medium-Range  
 213 Weather Forecasts (ECMWF) Reanalysis (ERA)-Interim model. Amezcua et al. (2020)  
 214 presented a way to implement an off-line assimilation of infrasound data into atmospheric

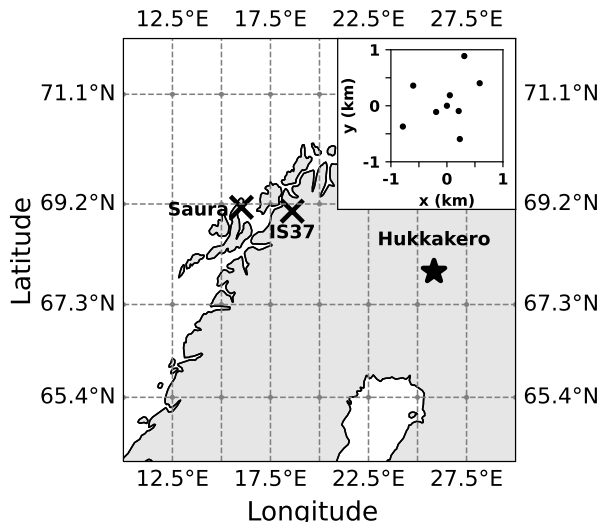


**Figure 1.** Location of all sources of data used in this study: Hukkakero explosion site, IS37 infrasound array, and Saura medium-frequency radar. The SD-WACCM-X atmospheric model grid is displayed on the map as gray dashed lines. The IS37 array layout is shown in the inset.

215 models using Ensemble Kalman filters. The study extends the approach by Blixt et al.  
 216 (2019), demonstrating that assimilation of back-azimuth deviation allows for corrections  
 217 to atmospheric winds at tropospheric and stratospheric altitudes. Based on the same dataset,  
 218 Vera Rodriguez et al. (2020) developed an extended inversion methodology that uses in-  
 219 frasound observations to update atmospheric wind and temperature profiles on the ba-  
 220 sis of the ERA5 re-analysis ensembles.

221 Still, Hukkakero related infrasound signals have not previously been used to probe  
 222 small-scale atmospheric inhomogeneities.

### 223 3 Materials and Methods

#### 224 3.1 Infrasound dataset and signal pre-processing

225 This study exploits Hukkakero explosions and the associated signals recorded at  
 226 infrasound array IS37 that is located at  $\sim 320$  km distance in Bardufoss, Norway (69.07°  
 227 N, 18.61° E; Fig. 1). This 10-element array is part of the International Monitoring Sys-  
 228 tem (IMS) for the verification of the CTBT (Marty, 2019). The region is also host to  
 229 a cluster of additional seismo-acoustic monitoring stations (Gibbons et al., 2015). Dur-  
 230 ing the years 2014 – 2017, 57 explosions took place at Hukkakero, however 8 of them  
 231 (the three last explosions in 2014 and the five last explosions in 2016) were significantly  
 232 weaker (Gibbons et al., 2015) and are therefore not considered in the current study. Ori-  
 233 gin times of the analyzed 49 explosions are tabulated in Appendix A.

234 For each explosion, the back-azimuth and apparent velocity of the dominant wave-  
 235 front were estimated using a conventional time-domain array processing technique (Melton  
 236 & Bailey, 1957). The detection of coherent infrasound over the array is based on the eval-  
 237 uation of the so-called Fisher ratio. The Fisher ratio corresponds to a probability of de-  
 238 tection of a coherent signal with a specific signal-to-noise ratio (SNR). The associated  
 239 inter-element time-delays are used to form the so-called best-beam, for which the indi-  
 240 vidual array recordings are time-aligned before summation. Details on the particular im-

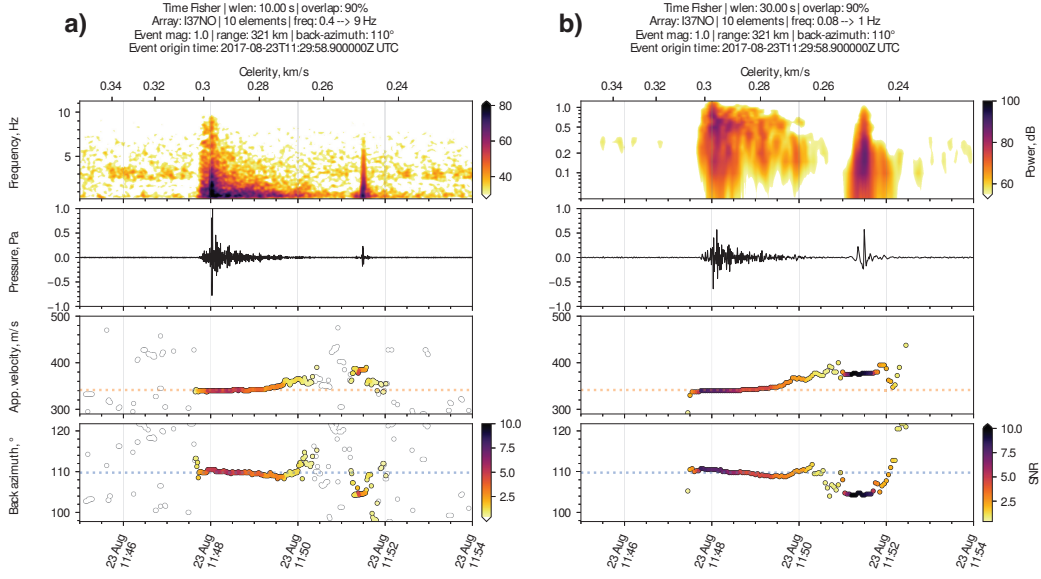


**Figure 2.** Array processing results for a Hukkakero explosion on 23 August 2017, processed between a) 0.4 – 9 Hz and b) 0.08 – 1.0 Hz. Top panel: spectrogram displayed in decibel. Second panel: the best-beam trace with an orange dashed line indicating the sound speed on the ground ( $\approx 340$  m/s). Third panel: apparent velocity. Bottom panel: the back-azimuth, where the blue dashed line corresponds to the great-circle back-azimuth ( $110^\circ$ ) towards Hukkakero.

241 plementation can be found in Evers (2008). The beam waveforms were processed in two  
 242 partly overlapping frequency bands to highlight the key trace features, 0.4–9 Hz and  
 243 0.08 – 1.0 Hz. Figure 2 shows array analysis results for one explosion filtered in both  
 244 frequency bands. Note, the contribution of ocean ambient noise (“microbaroms”) around  
 245 0.2 Hz (Vorobeve et al., 2021; De Carlo et al., 2020) and wind noise at low frequencies  
 246 is negligible compared to the explosion contributions.

247 Fig. 3 shows a compilation of IS37 infrasound signals from the 49 explosions ex-  
 248 ploited in the current study. The first arrivals are detected between 17.5–19 minutes  
 249 (celerity of 281–314 m/s) after the explosion (Fig. 3a) and feature energy in a broad  
 250 frequency band (Fig. 2a). Typically, the waveform consists of a main arrival with a sig-  
 251 nificantly larger amplitude, followed by a coda (“tail”) with progressively increasing ap-  
 252 parent velocity with values within the 340–360 m/s. These ranges of celerities and ap-  
 253 parent velocities are typical for stratospheric arrivals (Nippress et al., 2014; Lonzaga, 2015)  
 254 which generally refract or reflect near the stratopause. Similarly extended wave trains  
 255 have been observed in far-field infrasound recordings following large detonations (Fee et  
 256 al., 2013; Lalande & Waxler, 2016; Green et al., 2018), and it was assumed that these  
 257 wave trains originate from interactions with atmospheric perturbations caused by GWs.

258 After this first wave train, a later arrival can in many cases be observed between  
 259 approximately 20–23 min after the explosion (a celerity range of 232–267 m/s). Figs. 2b  
 260 and 3b show the signals in a pass-band between 0.08 – 1.0 Hz. This arrival is charac-  
 261 terized by a low-frequency U-shaped waveform, has higher apparent velocity values (i.e.,  
 262  $> 360$  m/s) and larger back-azimuth deviations compared to the first arrival. All of these  
 263 characteristics are typical of arrivals returning from the lower thermosphere (Le Pichon  
 264 et al., 2005; Assink et al., 2012, 2013; Green et al., 2018; Blom & Waxler, 2021).

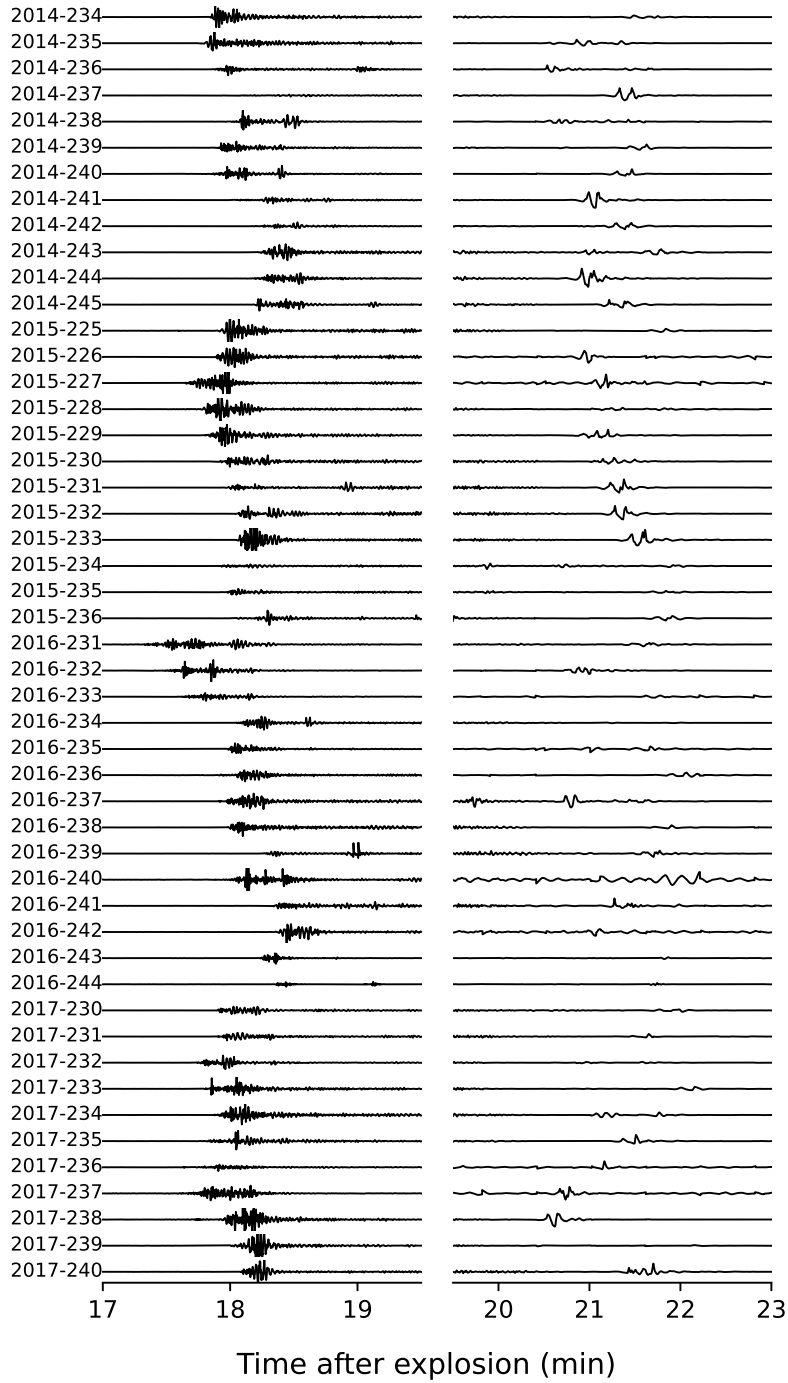


**Figure 3.** Infrasonic signals from 49 Hukkakero explosions that occurred in the time period 2014-2017. The signals have been recorded at infrasound array IS37 between (left) 17 – 19.5 minutes and (right) 19.5 – 23 minutes. The data are band-pass filtered between (left) 0.4 – 9 Hz and (right) 0.08 – 1 Hz. The y-axis of each trace has  $\pm 1$  Pa limit. The left-hand side labels display the year and the day-of-year when events took place.

265 A closer look at Figure 3 further reveals that several of the events feature an ar-  
 266 rival between the stratospheric and thermospheric arrivals, see also Gibbons et al. (2019,  
 267 Fig. 10.7). Although the current study only exploits the stratospheric arrivals for atmo-  
 268 spheric probing, it is worth noting the potential for further analysis and probing based  
 269 on later arrivals in the wavetrains, for example as demonstrated in Chunchuzov et al.  
 270 (2011).

### 271 3.2 The SD-WACCM-X atmospheric model

272 In this study, the Whole Atmosphere Community Climate Model with thermosphere  
 273 and ionosphere extension (WACCM-X; H.-L. Liu et al., 2018) is used as a model atmo-  
 274 sphere. The particular version is the *specified dynamics*, SD-WACCM-X, version v2.1  
 275 (Sassi et al., 2013), for which the temperature and winds are nudged by the Modern-Era  
 276 Retrospective analysis for Research and Applications, Version 2 (MERRA-2; Gelaro et  
 277 al., 2017) from the ground up to  $\sim 50$  km. Above that altitude, WACCM-X is free-running.  
 278 While WACCM-X extends up to about 500–700 km altitude (145 levels), we only con-  
 279 sider the altitude region relevant for infrasound propagation, which is up to 140 km al-  
 280 titude. The model has grid cells of  $1.9^\circ \times 2.5^\circ$  in latitude-longitude and a 3-h tempo-  
 281 ral resolution (see the Data availability Section). For a detailed description of chemical  
 282 and physical processes and parameterizations included in the model, see the studies by  
 283 H.-L. Liu et al. (2018); J. Liu et al. (2018).

284 The WACCM-X model has been validated against observations and empirical mod-  
 285 els and has shown a good agreement in thermospheric composition, density and tidal am-  
 286 plitudes (H.-L. Liu et al., 2018). The SD-WACCM-X model has been found to be rep-  
 287 resentative of the Earth’s atmosphere in studies of different atmospheric phenomena: e.g.,  
 288 elevated-stratopause events (Siskind et al., 2021; Orsolini et al., 2017), dynamics (Kumari  
 289 et al., 2021), atmospheric tides (Pancheva et al., 2020; Zhang et al., 2021; van Caspel  
 290 et al., 2022). In contrast to other models routinely used for infrasound propagation, SD-  
 291 WACCM-X provides a single consistent atmospheric model covering the altitude region  
 292 relevant for long-range infrasound propagation, with a suitable spatio-temporal resolu-  
 293 tion. In particular, WACCM should provide a more physical description of the MLT re-  
 294 gion when compared to atmospheric specifications that are typically used for thermo-  
 295 spheric arrival modeling, such as the HWM/MSIS climatological models (Drob, 2019).

296 Due to the proximity of the source to the receiver, the atmosphere can be approx-  
 297 imated as a 1-D layered medium without time dependence. To avoid interpolation in space  
 298 and time, we extract pressure, temperature, zonal and meridional winds from the grid  
 299 node closest to the explosion site (Fig. 1) and the time step closest to the explosion ori-  
 300 gin time. The atmospheric conditions for all 49 Hukkakero events are presented in Fig. 4.  
 301 Zonal and meridional winds in the stratosphere (20–50 km) are weak and have abso-  
 302 lute values of up to 18 m/s. Their variation from explosion to explosion is negligible with  
 303 standard deviation of 1–5 m/s. This can be explained by the summer-to-winter transi-  
 304 tion in the stratospheric polar vortex where zonal wind is reversing from the westward  
 305 summer circulation to the eastward winter circulation (Vaugh & Polvani, 2010; Vaugh  
 306 et al., 2017). In contrast, atmospheric winds in the mesosphere - lower thermosphere (50–  
 307 120 km) reach values of up to 100 m/s and vary strongly between explosions (standard  
 308 deviation of up to 33 m/s) (A. K. Smith, 2012).

309 Figure 4 also shows  $C_{\text{eff}}(z)$  ratio profiles (see Sect. 3.1) that have been computed  
 310 using the SD-WACCM-X model (see Sect. 2). It can be seen that around 50 km altitude  
 311 the ratio is close but does not exceed unity for most profiles, except for the events on  
 312 13 and 14 Aug 2015 (days 225 and 226). This indicates that the presence of a strong strato-  
 313 spheric waveguide for the Hukkakero-IS37 configuration in late summer is rather rare and  
 314 therefore (strong) stratospheric returns would not be expected at IS37. In contrast, the  
 315 effective sound speed ratio exceeds unity around lower thermosphere in all cases. This

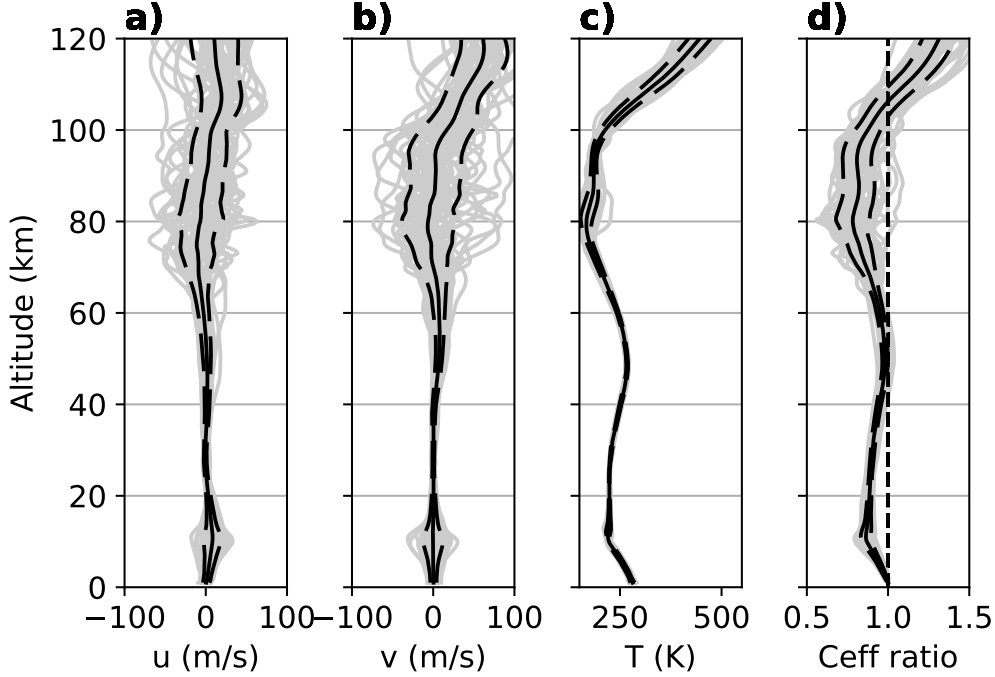


**Figure 4.** SD-WACCM-X atmospheric specifications for the 49 analyzed Hukkakero explosions, extracted at the grid point closest to the site around the time of the explosion. a) zonal wind, b) meridional wind, c) temperature, d) effective sound speed ratio.

316 can be attributed to the strong temperature gradient, which guarantees the presence of  
 317 a thermospheric waveguide.

318 The effects of small-scale atmospheric fluctuations on stratospheric arrivals is particu-  
 319 larly enhanced during periods of the year when the  $C_{\text{eff}}$  ratio near the stratopause  
 320 is close to unity (Assink et al., 2014). Under these conditions, the small perturbations  
 321 (e.g., gravity waves induced wind and temperature perturbations) can cause conditions  
 322 favorable for i) refraction or ii) reflection. The propagation effects (refraction or reflec-  
 323 tion) strongly depend on the vertical scale of the atmospheric fluctuations in compar-  
 324 ison to the infrasonic wavelength. For relatively large vertical scales, refraction of infra-  
 325 sonic waves can be simulated with ray theory, showing variations in travel time and back-  
 326 azimuth (Kulichkov, 2010). In contrast, infrasound scattering (or partial reflection) on  
 327 vertical scales comparable to the infrasonic wavelength is a full-wave effect that cannot  
 328 be simulated using ray theory. However, several studies (Chunchuzov & Kulichkov, 2020;  
 329 Green et al., 2018; Blixt et al., 2019) have reported observations of partial reflections from  
 330 stratospheric altitudes in the region where no stratospheric rays are predicted (i.e., the  
 331 shadow zone).

### 332 3.3 Ray-tracing using the SD-WACCM-X model

333 For each of the analyzed Hukkakero events, we simulated infrasound propagation  
 334 through its SD-WACCM-X atmospheric profile using the InfraGA ray tracer in 2-D Carte-  
 335 sian mode (see the Data availability Section for links and references). Rays were launched  
 336 from the location of Hukkakero in the direction of IS37 with inclination angles ranging  
 337 from 0 to 60 degrees measured from the horizontal.

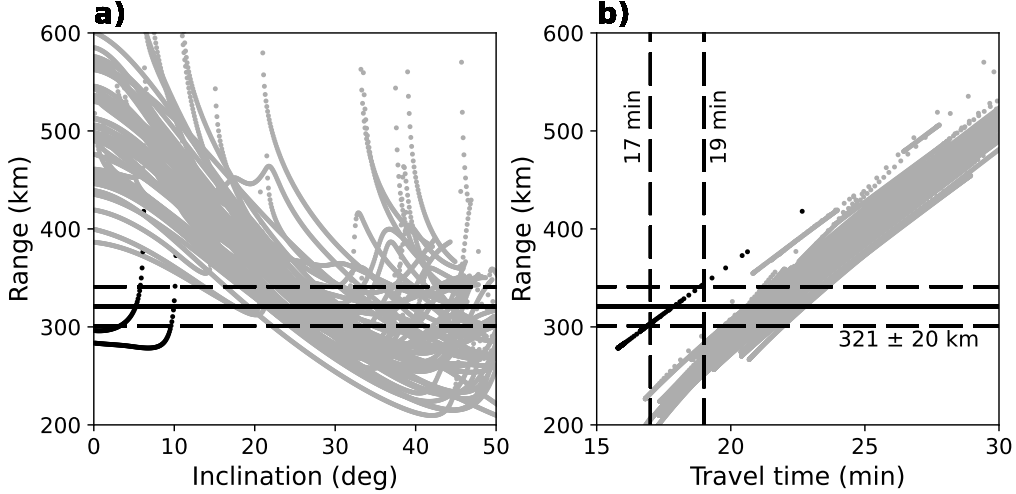


**Figure 5.** The first ground intercept information predicted by InfraGA for all explosive events. a) Eigenray departure inclination versus the distance from the source, b) travel time versus distance from the source. The eigenray turning height is color coded ( $< 60$  km - black dots,  $\geq 60$  km - gray dots). The Hukkakero-IS37 great-circle distance and the tolerance distance interval considered for ground intercept are indicated as a solid black line and dashed black lines, respectively. Observed travel time of the first arrival at IS37 is between 17 and 19 min (dashed black lines).

338 Fig. 5a shows ray departure inclination angle against distance from Hukkakero for  
 339 refracted paths predicted by ray theory. Almost all of the predictions correspond to ther-  
 340 mospheric refracted paths with turning heights in the lower thermosphere, near  $\sim 100$   
 341 km (gray dots). As was mentioned before, these thermospheric arrivals are often observed  
 342 at IS37 station Fig. 3. Fig. 5b shows the corresponding travel time (in min) for these rays.  
 343 Stratospheric arrivals with arrival times between 17-19 min that correspond to our ob-  
 344 servations (Fig. 3) are only predicted for two events that occurred on 13 and 14 August  
 345 2015 (days 225 and 226). It follows from analysis of the SD-WACCM-X profiles (Fig. 4),  
 346 that for these two days the  $C_{\text{eff}}(z)$  ratio exceeds unity in the stratosphere.

347 From the ray-tracing simulations, it can be concluded that i) IS37 is located in a  
 348 stratospheric shadow zone (i.e. there is no refraction-supported stratospheric duct) for  
 349 the vast majority of cases and ii) refracted infrasound reaches the station via thermo-  
 350 spheric ducts. Therefore, it is presumed that the stratospheric signals arrive at IS37 sta-  
 351 tion after being partially reflected in the middle atmosphere (Kulichkov, 2010; Chunchu-  
 352 zov et al., 2011).

353 Fig. 6 illustrates the raypaths of a stratospheric and a thermospheric arrival at IS37  
 354 for the analyzed Hukkakero events. The  $C_{\text{eff}}(z)$ -ratio profile shown in the figure is com-  
 355 puted based on the SD-WACCM-X model for 22 August 2017 at 12:00 UTC. The only  
 356 arrival predicted by ray tracing is a thermospheric refracted ray that propagates up to  
 357 113 km and is predicted to arrive at IS37 after  $\sim 22$  minutes, which matches the ob-  
 358 servations (see Fig. 3).

359 The reflected rays are not predicted by the classical ray theory but are instead con-  
 360 structed using a mirroring procedure akin to the approach in, e.g., Blixt et al. (2019).  
 361 We trace all rays until they reach the midpoint between Hukkakero and IS37 and then

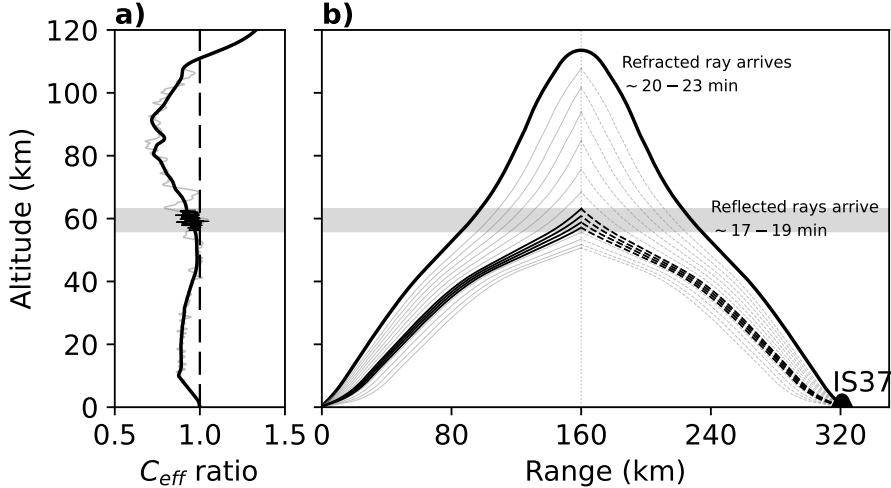


**Figure 6.** A schematic representation of infrasound raypaths from Hukkakero to IS37 relevant to this study. a) Effective sound speed ratio in direction of IS37 with a conceptual gravity wave perturbations (gray) and inhomogeneous layer of  $C_{\text{eff}}(z)$  fluctuations (black). b) Thermospheric ducting simulated by ray theory and explaining later arrivals (20-23 min) with U-shape (thick black line). Earlier arrivals (17-19 min) that are not predicted by ray theory can be explained by infrasound being scattered by small-scale  $C_{\text{eff}}(z)$  fluctuations in an atmospheric layer (dashed black lines).

362 mirror them to continue the path back to the surface. Due to acoustic reciprocity, this  
 363 is a valid approach in a range-independent medium. It is hypothesized that these rays  
 364 have scattered from an atmospheric layer with small-scale fluctuations in wind and  
 365 temperature. The travel time is then estimated as twice the propagation time to the mid-  
 366 point. The altitude range of the reflective layer is defined from the two rays that match  
 367 best the observed beginning and ending of the processed infrasound signal. In case of  
 368 a large discrepancy between the predicted and observed travel time for the lower bound-  
 369 ary, we calculate the lower layer altitude as  $z_j = z_{\text{top}} - C_{\text{eff}}(t_{\text{end}} - t_{\text{obs},j})$ , assuming a  
 370 constant effective sound speed in the layer. Here  $z_{\text{top}}$  is the upper boundary of the re-  
 371 flective layer obtained from ray tracing calculations,  $t_{\text{obs},j}$  is a set of discrete times de-  
 372 scribing the observed travel time of the arrival,  $t_{\text{end}}$  is the end of the analyzed signal win-  
 373 dow.

### 374 3.4 Effective sound speed retrieval

375 We applied the approach of Chunchuzov et al. (2015) to retrieve fine-scale effec-  
 376 tive sound-speed variations in the middle atmosphere. This method was designed to be  
 377 applied to stratospheric and thermospheric arrivals in the shadow zone, assuming that  
 378 infrasound was scattered from inhomogeneous atmospheric layers with fine-scale  $C_{\text{eff}}(z)$   
 379 fluctuations. It was demonstrated in (Chunchuzov et al., 2013) that temperature vari-  
 380 ations contribute relatively little to the effective sound-speed fluctuations ( $\sim 20\%$ ) com-  
 381 pared to wind variations ( $\sim 80\%$ ). Therefore, we associate  $C_{\text{eff}}(z)$  fluctuations with vari-  
 382 ations in horizontal wind.

383 This section presents the salient details behind the algorithm for the retrieval pro-  
 384 cedure, and provides a description of the main underlying assumptions. For a more de-

385 tailed derivation of the equations and discussion of the method, we refer to (Chunchuzov  
 386 et al., 2015; Chunchuzov & Kulichkov, 2020; Chunchuzov et al., 2022). For convenience,  
 387 most nomenclature and designations used in the current study are the same as in these  
 388 original studies.

389 The fine-scale effective sound-speed inversion approach is based on:

- 1) The assumption that infrasound is scattered or partially reflected at the midpoint between the source and receiver in a moving atmospheric layer with vertical fluctuations in the effective refractive index,

$$\varepsilon(z) = -2(\Delta c + \Delta u \sin \theta_0)/(c_1 \cos^2 \theta_0), \quad (2)$$

390 where  $\Delta c$  are the sound speed fluctuations;  $\Delta u$  is the projection of wind fluctu-  
 391 ations on the source-receiver radius vector;  $c_1$  is the average sound speed in the  
 392 layer; and  $\theta_0$  is the angle of incidence on the layer at altitude  $z$ . The effective re-  
 393 fractive index,  $\varepsilon(z)$ , is assumed to be non-zero only inside the moving layer. A de-  
 394 tailed derivation of Eq. 2 is provided in Appendix B.

- 2) The relationship between the vertical profile of the effective refractive index fluctu-  
 395 ations,  $\varepsilon(z)$ , and the scattered signal waveform,  $p'(t)$  is:

$$p'(t) = -\frac{p'_m r_0}{4R_1} \int_{-\infty}^{\infty} f(t - R_1/c_1 - z/a) \frac{d\varepsilon(z')}{dz'} dz', \quad (3)$$

397 where  $p'_m$  is the peak signal amplitude recorded at distance  $r_0$  close to the source;  
 398  $R_1$  is the total distance along the propagation path;  $f(t)$  is the normalized acous-  
 399 tic pressure waveform at  $r_0$ ;  $a = c_1/(2 \cos \theta_0)$  is a coefficient representing the speed  
 400 of the infrasound in the refractive layer; and  $d\varepsilon(z)/dz$  is the spatial derivative of  
 401  $\varepsilon(z)$ . The dimensionless waveform of the scattered signal is defined as  $I_0(t) = p'(t)R_1/(p'_m r_0)$ .

- 3) The assumption that the initial signal waveform,  $f(t)$ , has an N-wave shape (Lonzaga  
 402 et al., 2015) near the source and a duration  $T_0$  at the reflective layer altitude.

404 After integrating Eq. 3 and solving the resulting equation (more details in Chunchuzov  
 405 and Kulichkov (2020)), the relation between the effective refractive index profile and the  
 406 dimensionless waveform of the scattered signal becomes

$$I_0(t) = -\frac{\varepsilon(a[t - R_1/c_1]) + \varepsilon(a[t - R_1/c_1 - T_0])}{4}. \quad (4)$$

407 Equation 4 can be solved numerically for a set of discrete time samples with respect  
 408 to  $\varepsilon(z)$  using the method of least squares (see Appendix A for details). Next, the effec-  
 409 tive sound speed fluctuations,  $\Delta C_{\text{eff}}(z)$ , can be estimated from the  $\varepsilon(z)$  profile using Eq. 2  
 410 (Appendix B). However, several parameters need to be specified before solving Eq. 4:

- The average sound speed  $c_1$  is obtained by matching the travel time predicted by  
 411 ray-tracing simulations to the observed travel time, and thereby determining the  
 412 altitude range of the reflective layer and averaging the sound speed within it, as  
 413 well as angle  $\theta_0$ .
- An estimate of the peak overpressure close to the source,  $p'_m$ , is obtained using  
 414 the model by Kinney and Graham (1985) based on the blast yield. The typical  
 415 yield of Hukkakero explosions is presumed to be approximately 20 ton of TNT equiv-  
 416 alent (Gibbons et al., 2015). According to the Kinney and Graham (1985) model  
 417 with the initial conditions  $W = 20$  ton TNT,  $P_{\text{ref}} = 1.01325 \cdot 10^5$  Pa, and  $\rho_{\text{ref}} =$   
 418  $1.225 \text{ kg/m}^3$  (Atmosphere, 1976), the peak overpressure at  $r_0 = 1$  km from the  
 419 source becomes  $p'_m = 2320$  Pa.
- As the initially generated shock wave propagates, it experiences attenuation and  
 420 becomes distorted due to non-linear propagation effects, which become more promi-  
 421 nent with increasing height due to decreasing atmospheric density with altitude  
 422  
 423  
 424

(Lonzaga et al., 2015; Blom & Waxler, 2021). One of the distortion features associated with non-linear propagation is period lengthening, which occurs since positive and negative phases of the pressure wave travel at slightly different speed (Hamilton & Blackstock, 2008). This contributes to decreasing the amplitude of the acoustic pulse as its duration increases following the acoustic-pulse conservation law (Kulichkov et al., 2017). To get an estimate of the N-wave duration at the reflective layer altitude, weakly non-linear propagation simulations were performed using InfraGA. Properties of the initially generated shock wave (peak overpressure of 2320 Pa and positive pressure phase of 0.11 s) were calculated based on the Kinney and Graham (1985) model described above. Values of  $T_0$  in the range of 1–2 s were found to correspond to altitudes in the range of 50–80 km. This is the region from where we expect rays to reflect from, following the travel-time based mirroring simulations as described in Sect. 3.3.

## 4 Results

This study analyzes the first (stratospheric) Hukkakero arrivals in the infrasound recordings described in Sect. 3.1 and illustrated in Fig. 3. For the 49 Hukkakero blasts investigated, we processed a 30 second segment of the infrasound best-beam signal traces using the recipe provided in Sect. 3.4. Figure 7 displays the  $\Delta C_{\text{eff}}(z)$  profiles retrieved. There is a day-to-day variability in the reflective layer altitude, with all  $\Delta C_{\text{eff}}(z)$  profiles being located within stratopause–lower mesosphere altitudes of 50 – 75 km with the average depth of  $7.75 \pm 0.38$  km. Previous studies demonstrate that infrasound signal characteristics observed for events with similar strength and source-receiver geometry are highly sensitive to varying middle atmospheric winds and temperatures (Le Pichon et al., 2002; Drob, 2019; Averbuch et al., 2022). Therefore, the difference in the arrival time between events, as displayed in Fig. 3, can be related to the variation in the infrasound probing altitude. This is confirmed by the overall agreement in the arrival time variations for the explosions studied and the associated altitude variation of the retrieved fluctuation profiles, see Fig. 7. It should be noted that the same  $\Delta C_{\text{eff}}(z)$  retrieval procedure can also be applied to later arrivals, which correspond to higher altitudes, as demonstrated in Chunchuzov et al. (2022).

The majority of the effective sound-speed fluctuations retrieved,  $\Delta C_{\text{eff}}(z)$ , have amplitudes of up to 5 m/s. However, for some cases, the amplitudes reach up to 15 m/s. Exceptionally high  $\Delta C_{\text{eff}}(z)$  amplitudes of up to 25 m/s are estimated from the waveform recorded on 27 August 2016 (day 240 shown as the gray profile in Fig. 7). There are two reasons behind it. First, the signal amplitude reaches 2 Pa which is larger than for any other event. Second, rapid changes in the waveform amplitude make it difficult for the fitting procedure to find an appropriate solution (see Appendix B). We consider this event as an outlier and suggest that it should be interpreted as a refracted rather than reflected arrival, and therefore remove it from the analysis.

The root-mean-square error (RMSE) of  $\Delta C_{\text{eff}}(z)$  retrieved varies within 6–18% (see Appendix A). This RMSE is calculated based on the difference between the left- and right- hand sides of Eq. 4 (see Appendix B for details).

Next, we perform a vertical wavenumber spectral analysis of the retrieved  $\Delta C_{\text{eff}}(z)$  profiles by estimating the PSD using Welch’s method (Welch, 1967) with a Hamming window (window length of 750 m or 50 samples and 50% overlap). Figure 8 displays the vertical wavenumber power spectral density of the retrieved effective sound-speed fluctuation profiles, as well as their mean. It can be seen that negative PSD slope is present for all events. The vertical wavenumber,  $k_z$ , that corresponds to the beginning of the negative slope is denoted the dominant wavenumber,  $m_*$ . Based on the analyzed events,  $m_* = 2.15 \cdot 10^{-3} \pm 4.4 \cdot 10^{-4}$  cycles/m (see Appendix A). Fitting the  $k_z^p$  power-law within

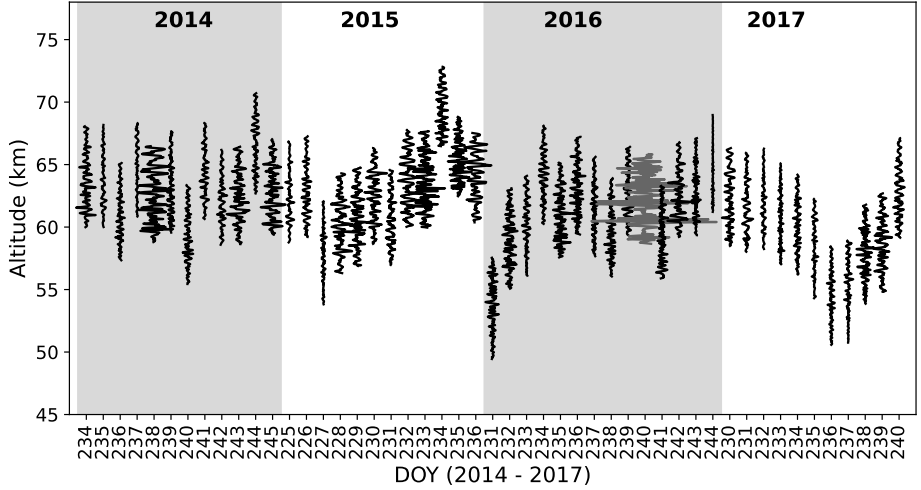


**Figure 7.** Retrieved fluctuations of the effective sound speed  $C_{\text{eff}}(z)$ . The  $C_{\text{eff}}(z)$  profile on 27 August 2016 (day 240) with exceptionally high values (more details in the text) is displayed in gray to avoid overlapping with other profiles.

475  $k_z > m_*$  provides an estimate of  $p = -3.35$  for the mean PSD and  $p = -3.50 \pm 0.39$   
 476 for all profiles (see Appendix A).

477 The power-law exponents obtained in this study are close to the  $k_z^{-3}$  power-law which  
 478 is known to correspond to the “universal” spectrum of horizontal wind fluctuations in-  
 479 duced by gravity waves or gravity wave saturation spectrum (Fritts & Alexander, 2003).  
 480 Various theories were proposed to explain the dynamics behind gravity wave saturation,  
 481 i.e., instability and wave-wave interaction. The saturation spectrum amplitude was shown  
 482 to correspond to  $CN^2k_z^{-3}$  with  $C$  typically varying within 0.1 – 0.4 (Hines, 1991) de-  
 483 pending on the theory and assumptions made. The first attempt to describe universal-  
 484 ity in measured wind spectra (e.g., Endlich et al., 1969; Dewan et al., 1984) was made  
 485 by Dewan and Good (1986) who assumed saturation via convective instabilities at each  
 486 vertical wave number independently and yielded  $C = 1$ . Later, this theory was extended  
 487 by S. A. Smith et al. (1987) to account also for amplitude limiting instabilities arising  
 488 from the whole wave spectrum instead, and value of  $C = 1/6$  was obtained. These tra-  
 489 ditional linear saturation theories were criticized in Hines (1991) and Chunchuzov (2002),  
 490 where it was shown that small-scale anisotropic inhomogeneities with  $k_z^{-3}$  vertical wavenum-  
 491 ber spectrum are shaped due to non-resonant internal wave-wave interactions. Chunchuzov  
 492 et al. (2015) compared vertical wavenumber spectra of effective sound-speed fluctuations  
 493 retrieved from infrasound detections of five volcanic eruptions and one explosion. Based  
 494 on this analysis, a value of  $C = 0.2$  for the upper stratosphere was proposed.

495 The power-laws corresponding to linear (Dewan & Good, 1986) and non-linear (Chunchuzov  
 496 et al., 2015) theoretical models are displayed in Fig. 8 together with error bars indicat-  
 497 ing possible variability in theoretical PSD amplitude ( $C = 0.1 - 0.4$ ). In both theo-  
 498 retical models, the altitude regime is controlled via the Brunt-Väisälä frequency,  $N$ . We  
 499 use  $N = 1.66 \cdot 10^{-2}$  rad/s in our calculations, which is typical for the lower mesosphere  
 500 (Dewan & Good, 1986). Theoretical models show a good agreement with the mean spec-  
 501 trum of the retrieved  $\Delta C_{\text{eff}}(z)$  profiles. This allows us to conclude that the infrasound-  
 502 based vertical wavenumber spectra that are obtained in this study are consistent with  
 503 previously obtained theoretical spectra, taking into account the confidence intervals of  
 504 those measurements (Fritts & Alexander, 2003).

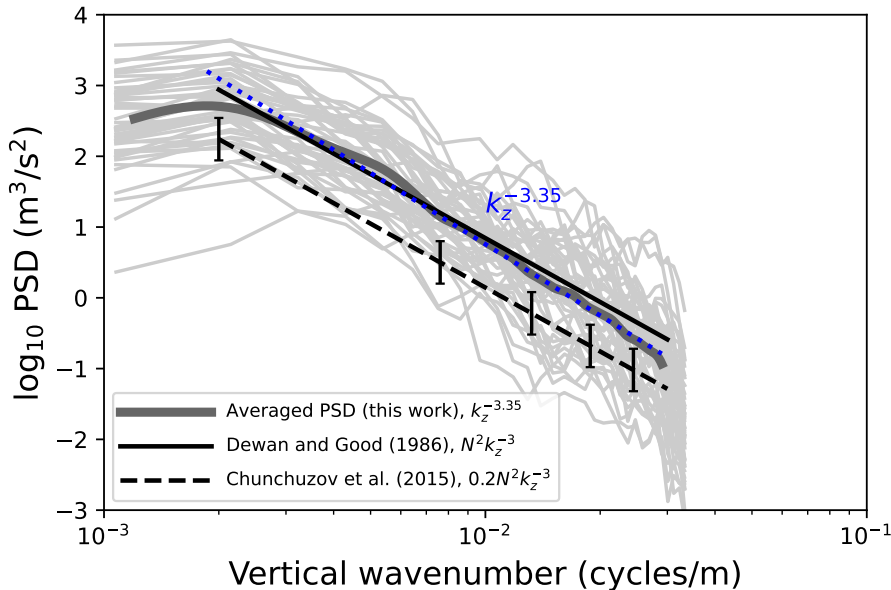


**Figure 8.** Vertical wavenumber power spectral density (PSD) of the retrieved  $\Delta C_{\text{eff}}(z)$  fluctuations (light gray lines) and their mean (dark gray line) versus theoretical models by Dewan and Good (1986) (black solid) and Chunchuzov et al. (2015) (black dashed). Black error bars indicate variability in theoretical PSD amplitude based on other theories mentioned in the text. The blue dotted line indicates the power-law fitting region for the mean PSD.

505 From the spectral analysis, we can estimate the outer and inner vertical scale of  
 506 atmospheric inhomogeneities that infrasound is sensitive to, based on the vertical wavenum-  
 507 ber limits within which the  $k_z^{-3}$  power-law establishes. Denoting the highest vertical wavenum-  
 508 ber as  $m_b$ , we obtain  $L_{\text{inner}} = 1/m_b = 33 - 37$  m and  $L_{\text{outer}} = 1/m_* = 386 - 585$  m.  
 509 Note that the limited altitude range of the  $\Delta C_{\text{eff}}(z)$  profiles retrieved restricts the sen-  
 510 sitivity to motions with smaller vertical wavenumbers (larger vertical scales). This could  
 511 be improved by processing longer segments of infrasound waveforms as was demonstrated  
 512 in e.g., Chunchuzov et al. (2013, 2015).

## 513 5 Discussion

514 The current study applies the effective sound-speed retrieval procedure by Chunchuzov  
 515 et al. (2015) to infrasound recordings in the shadow zone. This is the first time the afore-  
 516 mentioned approach is applied to a large and consistent dataset. Because we are retriev-  
 517 ing  $\Delta C_{\text{eff}}(z)$  profiles along a fixed source-receiver path and because the explosion yields  
 518 are similar for each event, we can consider the variability in the infrasound recordings  
 519 as being related to atmospheric dynamics.

520 The results show that vertical wavenumber PSDs obtained from the  $\Delta C_{\text{eff}}(z)$  pro-  
 521 files are close to the “universal” gravity wave saturation spectrum of  $k_z^{-3}$ . The very end  
 522 of the vertical wavenumber spectra in Fig. 8 corresponds to motions at scales of tens of  
 523 meters. This is on the edge of transition from the gravity wave saturation regime to the  
 524 turbulence regime where the theory predicts a transition from a  $k_z^{-3}$  power-law to  $k_z^{-5/3}$   
 525 (e.g., Gardner et al., 1993). The vertical wavenumber where this transition occurs may  
 526 have different values based on the latitude and altitude of interest, for example, the value

527 of  $2 \cdot 10^{-3}$  cycles/m was proposed in (Gardner et al., 1993) for mid-latitude mesopause  
 528 region. In contrast, Endlich et al. (1969) analyzed vertical wind profiles measured dur-  
 529 ing different seasons and found that their PSDs follow the  $k_z^{-3}$  power-law up to the ver-  
 530 tical wavenumber of  $10^{-2}$  cycles/m. However, the turbulence regime is outside of the scope  
 531 of this study, and we leave this question open for further research.

532 As  $C_{\text{eff}}(z)$  fluctuations are mostly associated with variations in horizontal wind (Sect. 3.4),  
 533 it would be interesting to compare the vertical wavenumber spectra obtained in this study  
 534 to spectra of wind measured near the IS37-Hukkakero region (Fig. 1). For this purpose,  
 535 the spectral characteristics of 11 infrasound-based  $\Delta C_{\text{eff}}(z)$  profile retrievals from 2017  
 536 were compared against independent wind measurements available from the Saura medium-  
 537 frequency (MF) radar near Andøya, Norway ( $69.14^\circ$  N,  $16.02^\circ$  E; Fig. 1). This radar is  
 538 located  $\sim 100$  km west of the IS37 infrasound station and  $\sim 420$  km north-west from  
 539 Hukkakero (Fig. 1), and operates on 3.17 MHz with 58 2kW pulsed transceiver modules.  
 540 Its observation capabilities include wind measurements, estimates of turbulent kinetic  
 541 energy dissipation rates, and electron density, as well as meteor observations. The ob-  
 542 servations typically provide measurements within the  $\sim 50$ – $100$  km altitude range with  
 543 a vertical resolution of 1–1.5 km (Singer et al., 2008). Hence, the system can observe  
 544 vertical variations at wavenumbers below approximately  $k_z = 10^{-3}$  cycles/m.

545 The wind data used for the validation has been derived from Doppler-Beam-Swinging  
 546 experiments measuring the radial velocity for one vertical and four oblique soundings in-  
 547 cluding statistical interferometric Angle of Arrival correction (see Renkowitz et al., 2018).

548 First, we directly compare the Saura radar winds to the SD-WACCM-X model winds.  
 549 As the effective sound speed  $\Delta C_{\text{eff}}(z)$  is taken along the horizontal infrasound propaga-  
 550 tion direction (Eq. 1), we project the Saura radar wind on the same unit vector point-  
 551 ing from Hukkakero towards IS37:  $\mathbf{u} \cdot \hat{n} = u \sin(\phi) + v \cos(\phi)$ , where  $\phi$  is the Hukkakero-  
 552 IS37 azimuth. The same projection was applied to the SD-WACCM-X wind profiles, ex-  
 553 tracted at the grid node located between the Saura radar and IS37 (Fig. 1). This com-  
 554 parison between Saura radar and SD-WACCM-X winds is displayed in Fig. 9a,b. Although  
 555 the radar measurements do not fully cover the altitude region where the infrasound-based  
 556  $\Delta C_{\text{eff}}(z)$  profiles are retrieved (highlighted in Fig. 9a,b), it can still be seen that the Saura  
 557 wind measurement features a pattern similar to the SD-WACCM-X model. There is a  
 558 weak wind pattern ( $< 50$  m/s) that alternates between positive and negative values, mostly  
 559 modulated by tidal waves. Above 70 km, a noticeable discrepancy between measured and  
 560 modeled winds is observed. This may be related to a lower temporal resolution of the  
 561 model compared to the radar, the distance between the sampling locations, or to inac-  
 562 curacies in the parametrization of gravity wave breaking used in the SD-WACCM-X model.  
 563 Moreover, note that above  $\sim 50$  km SD-WACCM-X is not supported by any observa-  
 564 tional dataset and is, therefore, expected to deviate more from the measurements. This  
 565 discrepancy between the radar measured winds and SD-WACCM was shown in (de Wit  
 566 et al., 2014), and is not unique to our measurements.

567 Next, we interpolate the SD-WACCM-X profiles to the radar vertical grid and per-  
 568 form a spectral comparison between the SD-WACCM-X and Saura radar wind profiles  
 569 closest in time to the explosion onset. The obtained vertical wavenumber spectra are dis-  
 570 played in Fig. 9c together with gravity wave saturation theories from Fig. 8. One can  
 571 see a good agreement in PSD amplitudes between the radar, atmospheric model and GW  
 572 saturation theories. However, it's clear that SD-WACCM-X wind spectra have steeper  
 573 slope and seem to underestimate amplitudes at ranges  $10^{-4}$ – $10^{-3}$  cycles/m. A more  
 574 detailed look into SD-WACCM-X and Saura radar horizontal winds over long time pe-  
 575 riods is needed to fully understand the nature of such discrepancy. We leave this ques-  
 576 tion open for further research suggesting that parametrization of subgrid-scale processes  
 577 in SD-WACCM-X can probably be improved.

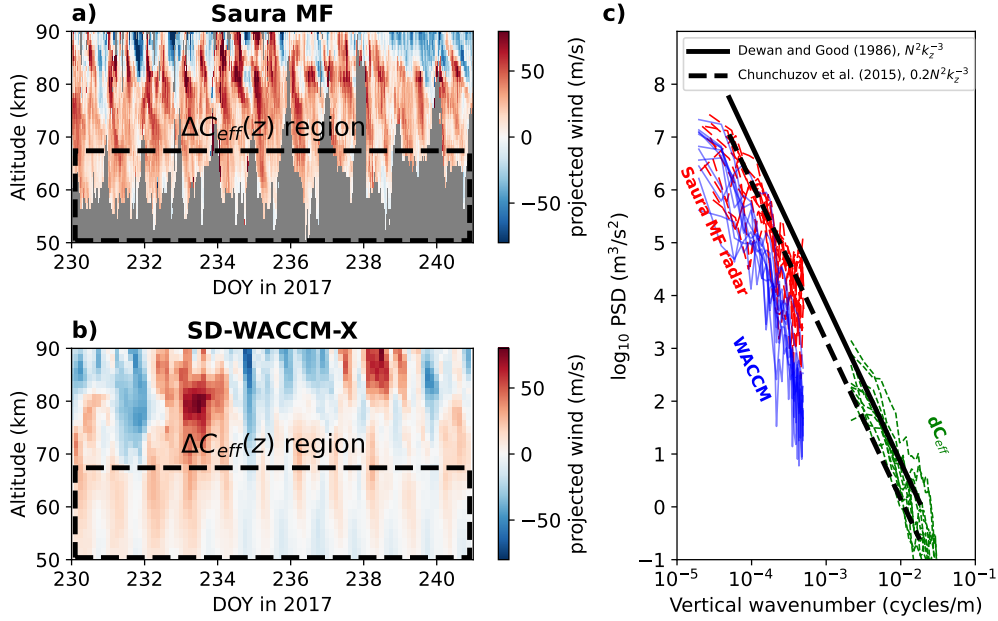


**Figure 9.** a) Projection of wind measured by Saura MF radar and b) predicted by SD-WACCM-X on the vector connecting Hukkakero and IS37. c) Vertical wavenumber spectra of the Saura radar winds (red dashed), SD-WACCM-X winds (blue solid) and retrieved  $\Delta C_{\text{eff}}(z)$  fluctuations (green dotted) for the explosions in 2017, versus theoretical models by Dewan and Good (1986) (black solid) and Chunchuzov et al. (2015) (black dashed).

578 To resolve the high-wavenumber part of the spectrum that the Saura radar and SD-  
 579 WACCM-X are insensitive to due to their vertical resolution, the infrasound-retrieved  
 580  $\Delta C_{\text{eff}}(z)$  profiles retrieved are used. The vertical wavenumber spectra for the 2017  $\Delta C_{\text{eff}}(z)$   
 581 profiles are presented in Fig. 9c. As was shown earlier (Fig. 8), the high-wavenumber part  
 582 of the spectrum follows the  $k_z^{-3}$  power-law and agrees well in amplitude with linear and  
 583 non-linear gravity wave saturation theories. The overall agreement found allows us to  
 584 suggest that Saura radar and infrasound-based  $\Delta C_{\text{eff}}(z)$  profiles represent low- and high-  
 585 wavenumber parts of the same “universal” GW spectrum.

586 Possible avenues for future research can include application of the same effective  
 587 sound-speed retrieval approach to later mesospheric and thermospheric arrivals observed  
 588 at IS37 (Fig. 3). This would provide an opportunity to study thicker atmospheric layers  
 589 and to possibly look at other physical phenomena that could be responsible for infrasound  
 590 scattering (e.g., polar mesospheric summer echoes). Another possible direction  
 591 of research could be comparing the effective sound-speed fluctuations obtained in this  
 592 study to other measurement techniques with high vertical resolution, e.g., lidar. More-  
 593 over, studying the 3D wind field and temperature fluctuations caused by gravity wave  
 594 could be performed by applying the retrieval approach to several infrasound stations around  
 595 the Hukkakero explosion site e.g., ARCES/ARCI (Karasjok, Norway), KRIS (Kiruna,  
 596 Norway) and APA/APAI (Apatity, Russia) (Gibbons et al., 2015).

## 597 6 Summary

598 In this study, infrasound waves from 49 blasts between 2014 and 2017 are used to  
 599 retrieve effective sound speed fluctuations,  $\Delta C_{\text{eff}}(z)$ , in the middle atmosphere. The ap-

600 plied retrieval recipe is based on approaches previously developed by Chunchuzov et al.  
601 (2013, 2015). It is based on a relation between the waveform of the scattered infrasound  
602 signal recorded on the surface in the shadow zone and the  $C_{\text{eff}}(z)$  fluctuation profile in  
603 an inhomogeneous atmospheric layer. The results obtained demonstrate that the infra-  
604 sound scattering occurs in the lower mesosphere between 50 and 75 km altitude. This  
605 atmospheric region is also known to be altitudes where gravity waves start to break (Garcia  
606 & Solomon, 1985). Therefore, information about the  $\Delta C_{\text{eff}}(z)$  retrieved from ground-based  
607 infrasound measurements is of direct interest for studying the GW activity and for po-  
608 tential improvement of GW parameterization schemes used in numerical weather pre-  
609 diction models. The spectral analysis of retrieved effective sound speed fluctuations in  
610 terms of vertical wavenumber spectra revealed that the tail of the mean spectrum fol-  
611 lows a  $k_z^{-3}$  power law. This law corresponds to the “universal” spectrum of horizontal  
612 wind fluctuations induced by gravity waves (Fritts & Alexander, 2003). The spectral char-  
613 acteristics of the 11 infrasound-based  $\Delta C_{\text{eff}}(z)$  profiles retrieved for 2017 were compared  
614 against independent wind measurements by the Saura MF radar. Good agreement in am-  
615 plitudes and slopes of the spectra was demonstrated, indicating that the infrasound and  
616 the radar measurements represent the high- and low-wavenumber sections of the “uni-  
617 versal” gravity-wave spectrum, respectively. Therefore, the current study opens the way  
618 for remote sensing of GW activity by means of ground-based infrasound measurements  
619 and to improve the representation of small-scale wind inhomogeneities in upper atmo-  
620 spheric model products. The latter would be beneficial for the infrasound scientific field  
621 since advanced simulations of infrasound propagation require atmospheric specifications  
622 with high vertical resolution (Hedlin & Drob, 2014; Chunchuzov et al., 2015; Lalande &  
623 Waxler, 2016; Sabatini et al., 2019). Moreover, the prospects of using explosive event se-  
624 quences as *datasets of opportunity* for middle atmospheric remote sensing can pave the  
625 way for an enhanced GW representation in atmospheric models.

626 **Appendix A Retrieved parameters and comparisons**

627 Table A1 provides details about the spectral analysis performed in Sect. 4.

**Table A1.** Explosion origin time, dominant wavenumber and the slope for the corresponding spectrum.

Origin time (yyyy-mm-dd HH:MM:SS, UTC)	DOY	$m_*$ [cycl/m]	exponent in $k_z^p$	RMSE relative to max amplitude
2014-08-22 11:59:59	234	2.15e-3	-3.79	0.06
2014-08-23 10:29:59	235	1.07e-3	-3.43	0.08
2014-08-24 11:59:59	236	2.15e-3	-3.29	0.13
2014-08-25 10:29:59	237	1.07e-3	-3.23	0.10
2014-08-26 10:59:59	238	2.15e-3	-3.04	0.07
2014-08-27 10:59:59	239	2.15e-3	-2.95	0.08
2014-08-28 10:59:59	240	2.15e-3	-3.30	0.08
2014-08-29 10:29:59	241	2.15e-3	-3.83	0.13
2014-08-30 10:29:59	242	2.15e-3	-3.95	0.10
2014-08-31 10:59:59	243	2.15e-3	-3.63	0.08
2014-09-01 09:59:59	244	2.15e-3	-3.67	0.13
2014-09-02 09:29:59	245	2.15e-3	-3.25	0.09
2015-08-13 10:59:59	225	2.15e-3	-3.71	0.08
2015-08-14 10:04:59	226	2.15e-3	-3.54	0.14
2015-08-15 10:59:59	227	2.15e-3	-3.87	0.09
2015-08-16 10:59:59	228	2.15e-3	-3.56	0.09
2015-08-17 11:59:59	229	2.15e-3	-3.02	0.13
2015-08-18 09:59:59	230	2.15e-3	-3.86	0.06
2015-08-19 09:29:59	231	2.15e-3	-2.90	0.08
2015-08-20 09:29:59	232	2.15e-3	-3.57	0.13
2015-08-21 09:29:59	233	2.15e-3	-3.19	0.08
2015-08-22 11:29:59	234	2.15e-3	-2.84	0.11
2015-08-23 11:29:59	235	2.15e-3	-2.65	0.09
2015-08-24 12:00:00	236	2.15e-3	-3.52	0.06
2016-08-18 12:29:59	231	2.15e-3	-3.18	0.10
2016-08-19 11:29:59	232	2.15e-3	-4.00	0.12
2016-08-20 13:29:59	233	2.15e-3	-3.76	0.07
2016-08-21 13:00:00	234	2.15e-3	-3.71	0.12
2016-08-22 11:59:59	235	2.15e-3	-3.60	0.09
2016-08-23 12:59:59	236	1.07e-3	-2.78	0.18
2016-08-24 11:59:59	237	2.15e-3	-3.06	0.12
2016-08-25 11:29:59	238	3.23e-3	-4.11	0.10
2016-08-26 11:29:59	239	2.15e-3	-3.36	0.10
2016-08-27 12:59:59	240	3.23e-3	-4.07	0.06
2016-08-28 10:59:59	241	2.15e-3	-3.13	0.13
2016-08-29 09:59:59	242	2.15e-3	-3.46	0.10
2016-08-30 07:54:59	243	3.22e-3	-3.13	0.07
2016-08-31 08:49:59	244	3.23e-3	-3.80	0.06
2017-08-18 11:59:59	230	2.15e-3	-4.25	0.18
2017-08-19 11:00:00	231	1.08e-3	-3.46	0.16
2017-08-20 12:00:00	232	2.15e-3	-3.70	0.08
2017-08-21 12:59:59	233	3.22e-3	-4.23	0.07
2017-08-22 11:59:59	234	2.15e-3	-3.47	0.10
2017-08-23 11:29:59	235	2.15e-3	-4.11	0.07
2017-08-24 11:29:59	236	2.15e-3	-4.06	0.14
2017-08-25 09:59:59	237	2.15e-3	-3.75	0.10
2017-08-26 10:59:59	238	2.15e-3	-3.59	0.07
2017-08-27 11:29:59	239	2.15e-3	-3.34	0.08
2017-08-28 10:29:59	240	2.15e-3	-3.40	0.11
<b>Mean:</b>		2.15e-3	-3.50	
<b>STD:</b>		4.40e-4	-0.39	

## Appendix B Derivation of the inversion equations

### B1 Derivation of Eq. 2

Consider a stationary atmosphere consisting of an inhomogeneous moving layer within  $z_0 \leq z \leq z_H$  and a homogeneous half-space below and above it. The sound speed  $c(z)$ , wind velocity  $\mathbf{v}(z)$  and density  $\rho(z)$  have continuous first and second order derivatives, and are constant outside the inhomogeneous layer with values of  $c_1$ ,  $\mathbf{v}_1$  and  $\rho_1$ . The layer is filled with stratified sound speed, wind velocity and density fluctuations  $\Delta c(z)$ ,  $\Delta \mathbf{v}(z)$  and  $\Delta \rho(z)$  on top of the background atmosphere. Therefore, sound speed, atmospheric wind and density within the inhomogeneous layer are defined as:  $c_{1+\Delta}(z) = c_1 + \Delta c(z)$ ,  $\mathbf{v}_{1+\Delta}(z) = \mathbf{v}_1 + \Delta \mathbf{v}(z)$ ,  $\rho_{1+\Delta}(z) = \rho_1 + \Delta \rho(z)$ . In terms of the relative fluctuations, it's assumed that  $\Delta c/c_1$ ,  $\Delta v/c_1$  and  $\Delta \rho/\rho_1$  are of the same order of smallness, namely  $M = |\Delta c/c_1| \ll 1$ .

A plane monochromatic acoustic wave  $A \exp(i(\xi_x x + \xi_y y + \mu z - \omega t))$  propagates from the source to the receiver upward through the homogeneous atmosphere and incident on a moving inhomogeneous layer at an angle  $\theta$  measured from the vertical. Here  $A$  is complex wave amplitude,  $\omega$  is wave frequency,  $\boldsymbol{\xi} = (\xi_x, \xi_y)$  is the horizontal propagation vector,  $\mu = (k_0^2 - |\boldsymbol{\xi}|^2)^{1/2}$  is the vertical wavenumber, and  $k_0 = \omega/c_1$  is the wavenumber in the homogeneous atmosphere. The projection of the wind velocity  $\mathbf{v}(z)$  on the source-receiver radius vector  $\boldsymbol{\xi}$  is defined as  $u(z) = \mathbf{v}(z)\boldsymbol{\xi}/|\boldsymbol{\xi}|$ .

We introduce the squared effective refractive index following Chunchuzov et al. (2013) as:

$$N^2(z) = \left( n^2 \beta^2 - \frac{\xi^2}{k_0^2} \right) \left( \frac{\rho_0}{\rho \beta^2} \right)^2, \quad (\text{B1})$$

where  $n = c_1/c$  is a refractive index in a stationary medium,  $\beta = 1 - \boldsymbol{\xi}\mathbf{v}(z)/\omega$ ,  $\rho_0$  is a density dimension coefficient,  $\xi = k_0 \sin \theta (1 + u_1 \sin \theta / c_1)^{-1}$ .

Small relative fluctuations of the effective refractive index in an inhomogeneous layer are defined as:

$$\varepsilon(z) = \ln \frac{N_{1+\Delta}^2}{N_1^2} = \ln \frac{n_{1+\Delta}^2 \beta_{1+\Delta}^2 - \xi^2/k_0^2}{n_1^2 \beta_1^2 - \xi^2/k_0^2} + 2 \ln \frac{\rho_1}{\rho_{1+\Delta}} + 4 \ln \frac{\beta_1}{\beta_{1+\Delta}}, \quad (\text{B2})$$

where

$$n_1 = 1, \quad n_{1+\Delta} = \frac{c_1}{c_1 + \Delta c}, \quad \text{and} \quad \beta_1 = 1 - \xi u_1 / \omega = \left( 1 + \frac{u_1 \sin \theta}{c_1} \right)^{-1}, \quad (\text{B3})$$

and

$$\beta_{1+\Delta} = 1 - \frac{\xi(u_1 + \Delta u(z))}{\omega} = \beta_1 \left( 1 - \frac{\Delta u(z) \sin \theta}{c_1} \right). \quad (\text{B4})$$

Substituting parameters from Eq. B3 into Eq. B2 and assuming the first-order of smallness for the natural logarithm,  $\ln(x/y) \sim (x - y)/y$ , yields

$$\varepsilon(z) = \frac{-2[\Delta c/c_1 + \Delta u(z) \sin \theta / c_1] + \mathcal{O}(M^2)}{\cos^2 \theta} + 4 \frac{\Delta u(z) \sin \theta}{c_1} - 2 \frac{\Delta \rho}{\rho_1}. \quad (\text{B5})$$

As  $\theta$  approaches  $\pi/2$  the last two terms can be neglected and Eq. 2 is obtained.

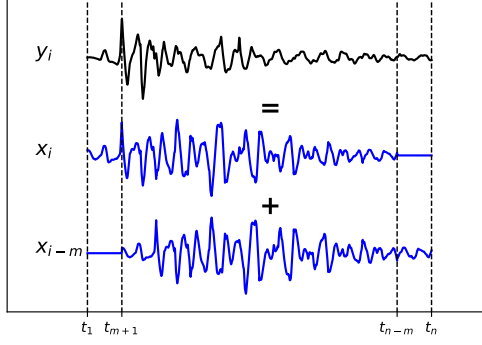


**Figure B1.** A synthetic example of the Eq. 4.

656

## B2 System of equations to solve Eq. 4

657

In this section, we provide the same explanation on how to numerically solve Eq. 4 as presented in (Chunchuzov & Kulichkov, 2020), but complemented with more detail.

658

659

660

661

662

663

664

665

Eq. 4 represents the dimensionless waveform of scattered signal as a sum of two effective refractive index profiles shifted in time by the time interval  $T_0$ . Let us denote values of the scattered signal at discrete times  $t_i$  as  $y_i = I_0(t_i)$  where  $i = 1, 2, \dots, n$  ( $n$  is the number of samples), and effective refractive index values as  $x_i = -\varepsilon(a[t_j - R_1/c_1])/4$  with non-zero values at  $1, 2, \dots, n - m$  and  $x_{i-m} = -\varepsilon(a[t_j - R_1/c_1 - T_0])/4$  with non-zero values at  $m + 1, m + 2, \dots, n$ , where  $m$  is the number of  $t_i$  values within the time interval  $T_0$ . Fig. B1 demonstrates Eq. 4 with the notation introduced.

Thus, the following system of linear algebraic equations with respect to  $x_i$  can be obtained from Eq. 4:

$$\begin{cases} y_i = x_i, & \text{for } 1 \leq i \leq m \\ y_i = x_i + x_{i-m}, & \text{for } m + 1 \leq i \leq n - m \\ y_i = x_{i-m}, & \text{for } n - m + 1 \leq i \leq n. \end{cases} \quad (\text{B6})$$

666

667

668

669

670

The number of unknowns in the system B6,  $n - m$ , is less than number of equations,  $n$ , and the system is therefore overdetermined. In this case, the least squares method can be used to find an approximate solution by minimizing the difference  $|\alpha X - Y|$  where  $X = x_j$ ,  $j = 1, 2, \dots, n - m$ ,  $Y = y_i$ ,  $i = 1, 2, \dots, n$ , and  $\alpha$  is the matrix of coefficients.

After the solution  $X = x_j$  has been found, the profile of the effective refractive index can be retrieved as  $\varepsilon(a[t_j - R_1/c_1]) = -4x_j$ . Next, the effective sound fluctuation profile is obtained from  $\varepsilon(z_j)$  values using Eq. 2 as:

$$\Delta C_{\text{eff}}(z_j) \approx \Delta c(z_j) + \Delta u(z_j) \sin \theta_0 = -\frac{\varepsilon(z_j)c_1 \cos^2 \theta_0}{2} = 2x_j c_1 \cos^2 \theta_0. \quad (\text{B7})$$

671

## Open Research Section

672

673

674

675

676

The 3-hourly SD-WACCM-X model product data are available via [https://www.earthsystemgrid.org/dataset/ucar.cgd.ccm4.SD-WACCM-X.v2.1.atm.hist.3hourly\\_inst.html](https://www.earthsystemgrid.org/dataset/ucar.cgd.ccm4.SD-WACCM-X.v2.1.atm.hist.3hourly_inst.html) (last access June 2022). The InfraGA infrasound propagation code (e.g., Blom & Waxler, 2017, 2021) is provided under open access by Los Alamos National Laboratory at <https://github.com/LANL-Seismoacoustics/infraGA> (last access June 2022).

677 The IS37 infrasound station is part of the International Monitoring System (IMS) of the  
 678 Preparatory Commission for the Comprehensive Nuclear-Test-Ban Treaty Organization  
 679 (CTBTO). Data access can be granted to third parties and researchers through the vir-  
 680 tual Data Exploitation Centre (vDEC) of the International Data Center: [https://www](https://www.ctbto.org/specials/vdec/)  
 681 [.ctbto.org/specials/vdec/](https://www.ctbto.org/specials/vdec/). The dataset of Saura wind measurements used in this  
 682 study is available via [https://www.radar-service.eu/radar/en/dataset/mzuBmhtrDxSGIBNd](https://www.radar-service.eu/radar/en/dataset/mzuBmhtrDxSGIBNd?token=leArd0pgjcsMPpeNSFy0)  
 683 [?token=leArd0pgjcsMPpeNSFy0](https://www.radar-service.eu/radar/en/dataset/mzuBmhtrDxSGIBNd?token=leArd0pgjcsMPpeNSFy0). More data can be obtained by contacting Toralf Renkwitz.

## 684 Acknowledgments

685 This research was supported by the Research Council of Norway FRIPRO/FRINATEK  
 686 basic research program, project contract 274377: *Middle Atmosphere Dynamics: Exploit-*  
 687 *ing Infrasound Using a Multidisciplinary Approach at High Latitudes* (MADEIRA). This  
 688 work was partially supported by the Research Council of Norway under contract 223252/F50  
 689 and RSF grant No. 21-17-00021. This study was facilitated by previous research performed  
 690 within the framework of the ARISE and ARISE2 projects (Blanc et al., 2018, 2019), funded  
 691 by the European Commission FP7 and Horizon 2020 programmes (Grant No. 284387 and  
 692 653980). The authors would also like to thank Yvan Orsolini for useful discussions and  
 693 suggestions.

## 694 References

- 695 Amezcua, J., Näsholm, S. P., Blixt, E. M., & Charlton-Perez, A. J. (2020). As-  
 696 simulation of atmospheric infrasound data to constrain tropospheric and  
 697 stratospheric winds. *Quarterly Journal of the Royal Meteorological Society*,  
 698 *146*(731), 2634–2653. doi: <https://doi.org/10.1002/qj.3809>
- 699 Assink, J., Le Pichon, A., Blanc, E., Kallel, M., & Khemiri, L. (2014). Evaluation  
 700 of wind and temperature profiles from ECMWF analysis on two hemispheres  
 701 using volcanic infrasound. *Journal of Geophysical Research: Atmospheres*,  
 702 *119*(14), 8659–8683. doi: <https://doi.org/10.1002/2014JD021632>
- 703 Assink, J., Smets, P., Marcillo, O., Weemstra, C., Lalande, J.-M., Waxler, R., &  
 704 Evers, L. (2019). Advances in infrasonic remote sensing methods. In *In-*  
 705 *frasound monitoring for atmospheric studies* (pp. 605–632). Springer. doi:  
 706 [https://doi.org/10.1007/978-3-319-75140-5\\_18](https://doi.org/10.1007/978-3-319-75140-5_18)
- 707 Assink, J., Waxler, R., & Drob, D. (2012). On the sensitivity of infrasonic trav-  
 708 eltimes in the equatorial region to the atmospheric tides. *Journal of Geo-*  
 709 *physical Research: Atmospheres*, *117*(D1). doi: [https://doi.org/10.1029/](https://doi.org/10.1029/2011JD016107)  
 710 [2011JD016107](https://doi.org/10.1029/2011JD016107)
- 711 Assink, J., Waxler, R., Frazier, W., & Lonzaga, J. (2013). The estimation of upper  
 712 atmospheric wind model updates from infrasound data. *Journal of Geophysical*  
 713 *Research: Atmospheres*, *118*(19), 10,707-10,724. doi: [https://doi.org/10.1002/](https://doi.org/10.1002/jgrd.50833)  
 714 [jgrd.50833](https://doi.org/10.1002/jgrd.50833)
- 715 Atmosphere, U. S. (1976). *Us standard atmosphere*. National Oceanic and Atmo-  
 716 spheric Administration.
- 717 Averbuch, G., Ronac-Giannone, M., Arrowsmith, S., & Anderson, J. (2022). Evi-  
 718 dence for short temporal atmospheric variations observed by infrasonic signals:  
 719 1. the troposphere. *Earth and Space Science*, *9*(3), e2021EA002036. doi:  
 720 <https://doi.org/10.1029/2021EA002036>
- 721 Bauer, P., Thorpe, A., & Brunet, G. (2015). The quiet revolution of numerical  
 722 weather prediction. *Nature*, *525*(7567), 47–55. doi: [https://doi.org/10.1038/](https://doi.org/10.1038/nature14956)  
 723 [nature14956](https://doi.org/10.1038/nature14956)
- 724 Becker, E., Vadas, S. L., Bossert, K., Harvey, V. L., Zülicke, C., & Hoffmann, L.  
 725 (2022). A high-resolution whole-atmosphere model with resolved gravity  
 726 waves and specified large-scale dynamics in the troposphere and stratosphere.  
 727 *Journal of Geophysical Research: Atmospheres*, *127*(2), e2021JD035018. doi:

- 10.1029/2021JD035018
- 728 Bengtsson, L., Andrae, U., Aspelien, T., Batrak, Y., Calvo, J., de Rooy, W., ... oth-  
 729 ers (2017). The HARMONIE-AROME model configuration in the ALADIN-  
 730 HIRLAM NWP system. *Monthly Weather Review*, *145*(5), 1919–1935. doi:  
 731 <https://doi.org/10.1175/MWR-D-16-0417.1>
- 732 Bertin, M., Millet, C., & Bouche, D. (2014). A low-order reduced model for the  
 733 long range propagation of infrasounds in the atmosphere. *The Journal of the*  
 734 *Acoustical Society of America*, *136*(1), 37–52. doi: [https://doi.org/10.1121/1](https://doi.org/10.1121/1.4883388)  
 735 [.4883388](https://doi.org/10.1121/1.4883388)
- 736 Blanc, E., Ceranna, L., Hauchecorne, A., Charlton-Perez, A., Marchetti, E., Evers,  
 737 L., ... Chum, J. (2018). Toward an improved representation of middle atmo-  
 738 spheric dynamics thanks to the ARISE project. *Surveys in Geophysics*, *39*(2),  
 739 171–225. doi: [10.1007/s10712-017-9444-0](https://doi.org/10.1007/s10712-017-9444-0)
- 740 Blanc, E., Pol, K., Le Pichon, A., Hauchecorne, A., Keckhut, P., Baumgarten,  
 741 G., ... Smets, P. (2019). Middle atmosphere variability and model uncer-  
 742 tainties as investigated in the framework of the ARISE project. In *Infra-*  
 743 *sound monitoring for atmospheric studies* (pp. 845–887). Springer. doi:  
 744 [https://doi.org/10.1007/978-3-319-75140-5\\_28](https://doi.org/10.1007/978-3-319-75140-5_28)
- 745 Blixt, E. M., Näsholm, S. P., Gibbons, S. J., Evers, L. G., Charlton-Perez, A. J., Or-  
 746 solini, Y. J., & Kværna, T. (2019). Estimating tropospheric and stratospheric  
 747 winds using infrasound from explosions. *The Journal of the Acoustical Society*  
 748 *of America*, *146*(2), 973–982. doi: <https://doi.org/10.1121/1.5120183>
- 749 Blom, P., & Waxler, R. (2017). Modeling and observations of an elevated, moving  
 750 infrasonic source: Eigenray methods. *The Journal of the Acoustical Society of*  
 751 *America*, *141*(4), 2681–2692. doi: <https://doi.org/10.1121/1.4980096>
- 752 Blom, P., & Waxler, R. (2021). Characteristics of thermospheric infrasound pre-  
 753 dicted using ray tracing and weakly non-linear waveform analyses. *The Journal*  
 754 *of the Acoustical Society of America*, *149*(5), 3174–3188. doi: [https://doi.org/](https://doi.org/10.1121/10.0004949)  
 755 [10.1121/10.0004949](https://doi.org/10.1121/10.0004949)
- 756 Bossert, K., Fritts, D. C., Pautet, P.-D., Williams, B. P., Taylor, M. J., Kaifler, B.,  
 757 ... MacKinnon, A. D. (2015). Momentum flux estimates accompanying mul-  
 758 tiscala gravity waves over Mount Cook, New Zealand, on 13 July 2014 during  
 759 the DEEPWAVE campaign. *Journal of Geophysical Research: Atmospheres*,  
 760 *120*(18), 9323–9337. doi: <https://doi.org/10.1002/2015JD023197>
- 761 Brekhovskikh, L. (1960). Propagation of acoustic and infrared waves in natural  
 762 waveguides over long distances. *Soviet Physics Uspekhi*, *3*(1), 159. doi: [10](https://doi.org/10.1070/PU1960v003n01ABEH003263)  
 763 [.1070/PU1960v003n01ABEH003263](https://doi.org/10.1070/PU1960v003n01ABEH003263)
- 764 Brissaud, Q., Näsholm, S. P., Turquet, A., & Le Pichon, A. (2023, January). Pre-  
 765 dicting infrasound transmission loss using deep learning. *Geophysical Journal*  
 766 *International*, *232*(1), 274–286. doi: [10.1093/gji/ggac307](https://doi.org/10.1093/gji/ggac307)
- 767 Chunchuzov, I. (2002). On the high-wavenumber form of the eulerian internal  
 768 wave spectrum in the atmosphere. *Journal of the atmospheric sciences*,  
 769 *59*(10), 1753–1774. doi: [https://doi.org/10.1175/1520-0469\(2002\)059<1753:](https://doi.org/10.1175/1520-0469(2002)059<1753:OTHWFO>2.0.CO;2)  
 770 [OTHWFO>2.0.CO;2](https://doi.org/10.1175/1520-0469(2002)059<1753:OTHWFO>2.0.CO;2)
- 771 Chunchuzov, I., & Kulichkov, S. (2020). *Infrasound propagation in an anisotropic*  
 772 *fluctuating atmosphere*. Cambridge Scholars Publishing.
- 773 Chunchuzov, I., Kulichkov, S., & Firstov, P. (2013). On acoustic N-wave reflections  
 774 from atmospheric layered inhomogeneities. *Izvestiya, Atmospheric and Oceanic*  
 775 *Physics*, *49*(3), 258–270. doi: <https://doi.org/10.1134/S0001433813020060>
- 776 Chunchuzov, I., Kulichkov, S., Perepelkin, V., Popov, O., Firstov, P., Assink, J.,  
 777 & Marchetti, E. (2015). Study of the wind velocity-layered structure in the  
 778 stratosphere, mesosphere, and lower thermosphere by using infrasound probing  
 779 of the atmosphere. *Journal of Geophysical Research: Atmospheres*, *120*(17),  
 780 8828–8840. doi: <https://doi.org/10.1002/2015JD023276>
- 781 Chunchuzov, I., Kulichkov, S., Popov, O., & Perepelkin, V. (2022). Infrasound

- 783 propagation through the atmosphere with mesoscale wind velocity and tem-  
 784 perature fluctuations. *Waves in Random and Complex Media*, 1–16. doi:  
 785 10.1080/17455030.2022.2056259
- 786 Chunchuzov, I., Kulichkov, S., Popov, O., Waxler, R., & Assink, J. (2011). Scatter-  
 787 ing of infrasound by anisotropic inhomogeneities of the atmosphere. *Izv. At-*  
 788 *mos. Oceanic Phys*, 47(5), 540–547.
- 789 Cugnet, D., de la Camara, A., Lott, F., Millet, C., & Ribstein, B. (2019). Non-  
 790 orographic gravity waves: Representation in climate models and effects on  
 791 infrasound. In A. Le Pichon, E. Blanc, & A. Hauchecorne (Eds.), *Infrasound*  
 792 *monitoring for atmospheric studies: Challenges in middle atmosphere dynam-*  
 793 *ics and societal benefits* (pp. 827–844). Cham, Switzerland: Springer. doi:  
 794 10.1007/978-3-319-75140-5\_27
- 795 De Carlo, M., Arduin, F., & Le Pichon, A. (2020, January). Atmospheric infra-  
 796 sound generation by ocean waves in finite depth: unified theory and applica-  
 797 tion to radiation patterns. *Geophysical Journal International*, 221(1), 569–585.  
 798 doi: 10.1093/gji/ggaa015
- 799 Dewan, E., & Good, R. (1986). Saturation and the “universal” spectrum for verti-  
 800 cal profiles of horizontal scalar winds in the atmosphere. *Journal of Geophysi-*  
 801 *cal Research: Atmospheres*, 91(D2), 2742–2748. doi: [https://doi.org/10.1029/  
 802 JD091iD02p02742](https://doi.org/10.1029/JD091iD02p02742)
- 803 Dewan, E., Grossbard, N., Quesada, A., & Good, R. (1984). Spectral analysis of  
 804 10m resolution scalar velocity profiles in the stratosphere. *Geophysical research*  
 805 *letters*, 11(1), 80–83. doi: <https://doi.org/10.1029/GL011i001p00080>
- 806 de Wit, R. J., Hibbins, R. E., Espy, P. J., Orsolini, Y. J., Limpasuvan, V., & Kin-  
 807 nison, D. E. (2014). Observations of gravity wave forcing of the mesopause  
 808 region during the January 2013 major sudden stratospheric warming. *Geo-*  
 809 *physical Research Letters*, 41(13), 4745–4752. doi: [https://doi.org/10.1002/  
 810 2014GL060501](https://doi.org/10.1002/2014GL060501)
- 811 Diamond, M. (1963). Sound channels in the atmosphere. *Journal of Geophysical Re-*  
 812 *search*, 68(11), 3459–3464. doi: <https://doi.org/10.1029/JZ068i011p03459>
- 813 Drob, D. (2019). Meteorology, climatology, and upper atmospheric composition for  
 814 infrasound propagation modeling. In *Infrasound monitoring for atmospheric*  
 815 *studies* (pp. 485–508). Springer. doi: [https://doi.org/10.1007/978-3-319-75140-  
 816 -5\\_14](https://doi.org/10.1007/978-3-319-75140-5_14)
- 817 Drob, D., Broutman, D., Hedlin, M., Winslow, N., & Gibson, R. (2013). A method  
 818 for specifying atmospheric gravity wavefields for long-range infrasound propa-  
 819 gation calculations. *Journal of Geophysical Research: Atmospheres*, 118(10),  
 820 3933–3943. doi: <https://doi.org/10.1029/2012JD018077>
- 821 Endlich, R. M., Singleton, R. C., & Kaufman, J. W. (1969). Spectral analysis of  
 822 detailed vertical wind speed profiles. *Journal of Atmospheric Sciences*, 26(5),  
 823 1030–1041. doi: [https://doi.org/10.1175/1520-0469\(1969\)026<1030:SAODVW>  
 824 .0.CO;2](https://doi.org/10.1175/1520-0469(1969)026<1030:SAODVW>2.0.CO;2)
- 825 Evers, L. G. (2008). *The inaudible symphony: On the detection and source identi-*  
 826 *fication of atmospheric infrasound* (PhD Thesis). Delft University of Technol-  
 827 ogy, The Netherlands.
- 828 Fee, D., Waxler, R., Assink, J., Gitterman, Y., Given, J., Coyne, J., ... others  
 829 (2013). Overview of the 2009 and 2011 Sayarim infrasound calibration exper-  
 830 iments. *Journal of Geophysical Research: Atmospheres*, 118(12), 6122–6143.  
 831 doi: <https://doi.org/10.1002/jgrd.50398>
- 832 Fritts, D. C., & Alexander, M. J. (2003). Gravity wave dynamics and effects in the  
 833 middle atmosphere. *Reviews of geophysics*, 41(1). doi: [https://doi.org/10.  
 834 .1029/2001RG000106](https://doi.org/10.1029/2001RG000106)
- 835 Garcia, R. R., & Boville, B. A. (1994). “Downward control” of the mean  
 836 meridional circulation and temperature distribution of the polar winter  
 837 stratosphere. *Journal of Atmospheric Sciences*, 51(15), 2238–2245. doi:

- 838 [https://doi.org/10.1175/1520-0469\(1994\)051\(2238:COTMMC\)2.0.CO;2](https://doi.org/10.1175/1520-0469(1994)051(2238:COTMMC)2.0.CO;2)
- 839 Garcia, R. R., & Solomon, S. (1985). The effect of breaking gravity waves on the  
840 dynamics and chemical composition of the mesosphere and lower thermo-  
841 sphere. *Journal of Geophysical Research: Atmospheres*, *90*(D2), 3850–3868.  
842 doi: <https://doi.org/10.1029/JD090iD02p03850>
- 843 Gardner, C. S., Hostetler, C. A., & Franke, S. J. (1993). Gravity wave models for  
844 the horizontal wave number spectra of atmospheric velocity and density fluc-  
845 tuations. *Journal of Geophysical Research: Atmospheres*, *98*(D1), 1035–1049.  
846 doi: <https://doi.org/10.1029/92JD02051>
- 847 Gelaro, R., McCarty, W., Suárez, M. J., Todling, R., Molod, A., Takacs, L., ...  
848 Zhao, B. (2017). The modern-era retrospective analysis for research and ap-  
849 plications, version 2 (MERRA-2). *Journal of climate*, *30*(14), 5419–5454. doi:  
850 <https://doi.org/10.1175/JCLI-D-16-0758.1>
- 851 Gibbons, S., Asming, V., Eliasson, L., Fedorov, A., Fyen, J., Kero, J., ... Vино-  
852 gradov, Y. (2015). The European Arctic: A laboratory for seismoacoustic stud-  
853 ies. *Seismological Research Letters*, *86*(3), 917–928. doi: 10.1785/0220140230
- 854 Gibbons, S., Kværna, T., & Näsholm, S. P. (2019). Characterization of the infra-  
855 sonic wavefield from repeating seismo-acoustic events. In *Infrasound monitor-*  
856 *ing for atmospheric studies* (pp. 387–407). Springer. doi: [https://doi.org/10.1007/978-3-319-75140-5\\_10](https://doi.org/10.1007/978-3-319-75140-5_10)
- 857  
858 Gibbons, S. J., Kværna, T., Tiira, T., & Kozlovskaya, E. (2020). A benchmark case  
859 study for seismic event relative location. *Geophysical Journal International*.  
860 doi: 10.1093/gji/ggaa362
- 861 Green, D. N., Waxler, R., Lalande, J.-M., Velea, D., & Talmadge, C. (2018).  
862 Regional infrasound generated by the Humming Roadrunner ground truth  
863 experiment. *Geophysical Journal International*, *214*(3), 1847–1864. doi:  
864 <https://doi.org/10.1093/gji/ggy232>
- 865 Hamilton, M., & Blackstock, D. (2008). *Nonlinear acoustics*. Acoustical Society of  
866 America.
- 867 Hedlin, M. A., & Drob, D. P. (2014). Statistical characterization of atmospheric  
868 gravity waves by seismoacoustic observations. *Journal of Geophysical Research:*  
869 *Atmospheres*, *119*(9), 5345–5363. doi: <https://doi.org/10.1002/2013JD021304>
- 870 Hines, C. O. (1991). The saturation of gravity waves in the middle atmosphere. Part  
871 II: Development of doppler-spread theory. *Journal of Atmospheric Sciences*,  
872 *48*(11), 1361–1379. doi: [https://doi.org/10.1175/1520-0469\(1991\)048\(1361:  
873 TSOGWI\)2.0.CO;2](https://doi.org/10.1175/1520-0469(1991)048(1361:TSOGWI)2.0.CO;2)
- 874 Kinney, G., & Graham, K. (1985). Explosive shocks in air, 2 nd. *New York:*  
875 *Springer Science*, *10*, 978–3.
- 876 Kulichkov, S. (2010). On the prospects for acoustic sounding of the fine structure of  
877 the middle atmosphere. In *Infrasound monitoring for atmospheric studies* (pp.  
878 511–540). Springer. doi: [https://doi.org/10.1007/978-1-4020-9508-5\\_16](https://doi.org/10.1007/978-1-4020-9508-5_16)
- 879 Kulichkov, S., Popov, O., Mishenin, A., Chunchuzov, I., Chkhetiani, O., & Tsybul-  
880 skaya, N. (2017). Using the acoustic-pulse conservation law in estimating  
881 the energy of surface acoustic sources by remote sounding. *Izvestiya, Atmo-*  
882 *spheric and Oceanic Physics*, *53*(6), 603–612. doi: [https://doi.org/10.1134/  
883 S0001433817060068](https://doi.org/10.1134/S0001433817060068)
- 884 Kumari, K., Wu, H., Long, A., Lu, X., & Oberheide, J. (2021). Mechanism  
885 studies of Madden-Julian oscillation coupling into the mesosphere/lower  
886 thermosphere tides using SABER, MERRA-2, and SD-WACCMX. *Jour-*  
887 *nal of Geophysical Research: Atmospheres*, *126*(13), e2021JD034595. doi:  
888 <https://doi.org/10.1029/2021JD034595>
- 889 Lalande, J.-M., & Waxler, R. (2016). The interaction between infrasonic waves  
890 and gravity wave perturbations: Application to observations using uttr rocket  
891 motor fuel elimination events. *Journal of Geophysical Research: Atmospheres*,  
892 *121*(10), 5585–5600. doi: <https://doi.org/10.1002/2015JD024527>

- 893 Le Pichon, A., Assink, J. D., Heinrich, P., Blanc, E., Charlton-Perez, A., Lee, C. F.,  
 894 ... Claud, C. (2015). Comparison of co-located independent ground-based  
 895 middle atmospheric wind and temperature measurements with numerical  
 896 weather prediction models. *Journal of Geophysical Research: Atmospheres*,  
 897 *120*(16), 8318–8331. doi: <https://doi.org/10.1002/2015JD023273>
- 898 Le Pichon, A., Blanc, E., & Drob, D. (2005). Probing high-altitude winds using  
 899 infrasound. *Journal of Geophysical Research: Atmospheres*, *110*(D20). doi:  
 900 <https://doi.org/10.1029/2005JD006020>
- 901 Le Pichon, A., Garcés, M., Blanc, E., Barthélémy, M., & Drob, D. P. (2002). Acous-  
 902 tic propagation and atmosphere characteristics derived from infrasonic waves  
 903 generated by the Concorde. *The Journal of the Acoustical Society of America*,  
 904 *111*(1), 629–641. doi: <https://doi.org/10.1121/1.1404434>
- 905 Liu, H.-L., Bardeen, C. G., Foster, B. T., Lauritzen, P., Liu, J., Lu, G., ... others  
 906 (2018). Development and validation of the Whole Atmosphere Community  
 907 Climate Model with thermosphere and ionosphere extension (WACCM-X  
 908 2.0). *Journal of Advances in Modeling Earth Systems*, *10*(2), 381–402. doi:  
 909 <https://doi.org/10.1002/2017MS001232>
- 910 Liu, H.-L., McInerney, J., Santos, S., Lauritzen, P., Taylor, M., & Pedatella, N.  
 911 (2014). Gravity waves simulated by high-resolution whole atmosphere com-  
 912 munity climate model. *Geophysical Research Letters*, *41*(24), 9106–9112. doi:  
 913 <https://doi.org/10.1002/2014GL062468>
- 914 Liu, J., Liu, H., Wang, W., Burns, A. G., Wu, Q., Gan, Q., ... Schreiner, W. S.  
 915 (2018). First results from the ionospheric extension of WACCM-X during the  
 916 deep solar minimum year of 2008. *Journal of Geophysical Research: Space*  
 917 *Physics*, *123*(2), 1534–1553. doi: <https://doi.org/10.1002/2017JA025010>
- 918 Lonzaga, J. B. (2015). A theoretical relation between the celerity and trace velocity  
 919 of infrasonic phases. *The Journal of the Acoustical Society of America*, *138*(3),  
 920 EL242–EL247. doi: <https://doi.org/10.1121/1.4929628>
- 921 Lonzaga, J. B., Waxler, R. M., Assink, J. D., & Talmadge, C. L. (2015). Modelling  
 922 waveforms of infrasound arrivals from impulsive sources using weakly non-  
 923 linear ray theory. *Geophysical Journal International*, *200*(3), 1347–1361. doi:  
 924 <https://doi.org/10.1093/gji/ggu479>
- 925 Marty, J. (2019). The IMS infrasound network: current status and technological  
 926 developments. In *Infrasound monitoring for atmospheric studies* (pp. 3–62).  
 927 Springer. doi: [https://doi.org/10.1007/978-3-319-75140-5\\_1](https://doi.org/10.1007/978-3-319-75140-5_1)
- 928 McFarlane, N. (1987). The effect of orographically excited gravity wave drag on  
 929 the general circulation of the lower stratosphere and troposphere. *Journal of*  
 930 *Atmospheric Sciences*, *44*(14), 1775–1800. doi: [https://doi.org/10.1175/1520-0469\(1987\)044\(1775:TEOOEG\)2.0.CO;2](https://doi.org/10.1175/1520-0469(1987)044(1775:TEOOEG)2.0.CO;2)
- 931  
 932 Melton, B. S., & Bailey, L. F. (1957). Multiple signal correlators. *Geophysics*, *22*(3),  
 933 565–588. doi: <https://doi.org/10.1190/1.1438390>
- 934 Miller, A., Fritts, D., Chapman, D., Jones, G., Limon, M., Araujo, D., ... others  
 935 (2015). Stratospheric imaging of polar mesospheric clouds: A new window  
 936 on small-scale atmospheric dynamics. *Geophysical Research Letters*, *42*(14),  
 937 6058–6065. doi: <https://doi.org/10.1002/2015GL064758>
- 938 Nippres, A., Green, D. N., Marcillo, O. E., & Arrowsmith, S. J. (2014). Generating  
 939 regional infrasound celerity-range models using ground-truth information and  
 940 the implications for event location. *Geophysical Journal International*, *197*(2),  
 941 1154–1165. doi: <https://doi.org/10.1093/gji/ggu049>
- 942 Orsolini, Y. J., Limpasuvan, V., Pérot, K., Espy, P., Hibbins, R., Lossow, S.,  
 943 ... Murtagh, D. (2017). Modelling the descent of nitric oxide during  
 944 the elevated stratopause event of January 2013. *Journal of Atmospheric*  
 945 *and Solar-Terrestrial Physics*, *155*, 50–61. doi: [https://doi.org/10.1016/](https://doi.org/10.1016/j.jastp.2017.01.006)  
 946 [j.jastp.2017.01.006](https://doi.org/10.1016/j.jastp.2017.01.006)
- 947 Pancheva, D., Mukhtarov, P., Hall, C., Meek, C., Tsutsumi, M., Pedatella, N., &

- 948 Nozawa, S. (2020). Climatology of the main (24-h and 12-h) tides observed by  
 949 meteor radars at svalbard and tromsø: Comparison with the models CMAM-  
 950 DAS and WACCM-X. *Journal of Atmospheric and Solar-Terrestrial Physics*,  
 951 *207*, 105339. doi: <https://doi.org/10.1016/j.jastp.2020.105339>
- 952 Pilger, C., Ceranna, L., Ross, J. O., Vergoz, J., Le Pichon, A., Brachet, N., ...  
 953 Mialle, P. (2018). The European Infrasound Bulletin. *Pure and Applied*  
 954 *Geophysics*, *175*(10), 3619–3638. doi: [10.1007/s00024-018-1900-3](https://doi.org/10.1007/s00024-018-1900-3)
- 955 Podglajen, A., Le Pichon, A., Garcia, R. F., G erier, S., Millet, C., Bedka, K., ...  
 956 Hertzog, A. (2022). Stratospheric balloon observations of infrasound waves  
 957 from the January 15 2022 Hunga eruption, Tonga. *Geophysical Research Let-*  
 958 *ters*, e2022GL100833. doi: [10.1029/2022GL100833](https://doi.org/10.1029/2022GL100833)
- 959 Rapp, M., & L ubken, F.-J. (2004). Polar mesosphere summer echoes (PMSE): Re-  
 960 view of observations and current understanding. *Atmospheric chemistry and*  
 961 *physics*, *4*(11/12), 2601–2633. doi: <https://doi.org/10.5194/acp-4-2601-2004>
- 962 Renkowitz, T., Tsutsumi, M., Laskar, F. I., Chau, J. L., & Latteck, R. (2018). On the  
 963 role of anisotropic MF/HF scattering in mesospheric wind estimation. *Earth,*  
 964 *Planets and Space*, *70*(1), 1–16. doi: [https://doi.org/10.1186/s40623-018-0927-  
 965 \*0\*](https://doi.org/10.1186/s40623-018-0927-0)
- 966 Sabatini, R., Snively, J. B., Baily, C., Hickey, M. P., & Garrison, J. L. (2019). Nu-  
 967 merical modeling of the propagation of infrasonic acoustic waves through the  
 968 turbulent field generated by the breaking of mountain gravity waves. *Geo-*  
 969 *physical Research Letters*, *46*(10), 5526–5534. doi: [https://doi.org/10.1029/](https://doi.org/10.1029/2019GL082456)  
 970 [2019GL082456](https://doi.org/10.1029/2019GL082456)
- 971 Sassi, F., Liu, H.-L., Ma, J., & Garcia, R. R. (2013). The lower thermosphere during  
 972 the northern hemisphere winter of 2009: A modeling study using high-altitude  
 973 data assimilation products in WACCM-X. *Journal of Geophysical Research:*  
 974 *Atmospheres*, *118*(16), 8954–8968. doi: <https://doi.org/10.1002/jgrd.50632>
- 975 Sch afer, B., Baumgarten, G., & Fiedler, J. (2020). Small-scale structures in noc-  
 976 tilucent clouds observed by lidar. *Journal of Atmospheric and Solar-Terrestrial*  
 977 *Physics*, *208*, 105384. doi: <https://doi.org/10.1016/j.jastp.2020.105384>
- 978 Selvaraj, D., Patra, A., Chandra, H., Sinha, H., & Das, U. (2014). Scattering cross  
 979 section of mesospheric echoes and turbulence parameters from gadanki radar  
 980 observations. *Journal of Atmospheric and Solar-Terrestrial Physics*, *119*,  
 981 162–172. doi: <https://doi.org/10.1016/j.jastp.2014.08.004>
- 982 Shaw, T. A., & Shepherd, T. G. (2008). Raising the roof. *Nature geoscience*, *1*(1),  
 983 12–13. doi: <https://doi.org/10.1038/ngeo.2007.53>
- 984 Singer, W., Latteck, R., & Holdsworth, D. (2008). A new narrow beam doppler  
 985 radar at 3 MHz for studies of the high-latitude middle atmosphere. *Advances*  
 986 *in Space Research*, *41*(9), 1488–1494. doi: [https://doi.org/10.1016/j.asr.2007.  
 987 \*10.006\*](https://doi.org/10.1016/j.asr.2007.10.006)
- 988 Siskind, D. E., Harvey, V. L., Sassi, F., McCormack, J. P., Randall, C. E., Hervig,  
 989 M. E., & Bailey, S. M. (2021). Two- and three-dimensional structures of the  
 990 descent of mesospheric trace constituents after the 2013 sudden stratospheric  
 991 warming elevated stratopause event. *Atmospheric Chemistry and Physics*,  
 992 *21*(18), 14059–14077. doi: [10.5194/acp-21-14059-2021](https://doi.org/10.5194/acp-21-14059-2021)
- 993 Smets, P. S. M., & Evers, L. G. (2014). The life cycle of a sudden stratospheric  
 994 warming from infrasonic ambient noise observations. *Journal of Geophys-*  
 995 *ical Research: Atmospheres*, *119*(21), 12–084. doi: [https://doi.org/10.1002/](https://doi.org/10.1002/2014JD021905)  
 996 [2014JD021905](https://doi.org/10.1002/2014JD021905)
- 997 Smith, A. K. (2012). Global dynamics of the MLT. *Surveys in Geophysics*, *33*(6),  
 998 1177–1230. doi: <https://doi.org/10.1007/s10712-012-9196-9>
- 999 Smith, S. A., Fritts, D. C., & Vanzandt, T. E. (1987). Evidence for a saturated spec-  
 1000 trum of atmospheric gravity waves. *Journal of Atmospheric Sciences*, *44*(10),  
 1001 1404–1410. doi: [https://doi.org/10.1175/1520-0469\(1987\)044<1404:EFASSO>2.0](https://doi.org/10.1175/1520-0469(1987)044<1404:EFASSO>2.0.CO;2)  
 1002 [.CO;2](https://doi.org/10.1175/1520-0469(1987)044<1404:EFASSO>2.0.CO;2)

- 1003 Stocker, T. F., Qin, D., Plattner, G.-K., Tignor, M. M., Allen, S. K., Boschung, J.,  
 1004 ... Midgley, P. M. (2014). Climate Change 2013: The physical science basis.  
 1005 working group I contribution to the fifth assessment report of IPCC the inter-  
 1006 governmental panel on climate change. In (p. 741–866). Cambridge University  
 1007 Press. doi: 10.1017/CBO9781107415324.020
- 1008 Strelnikov, B., Eberhart, M., Friedrich, M., Hedin, J., Khaplanov, M., Baumgarten,  
 1009 G., ... Pautet, P.-D. (2019). Simultaneous in situ measurements of small-  
 1010 scale structures in neutral, plasma, and atomic oxygen densities during the  
 1011 WADIS sounding rocket project. *Atmospheric Chemistry and Physics*, 19(17),  
 1012 11443–11460. doi: 10.5194/acp-19-11443-2019
- 1013 Tsuda, T. (2014). Characteristics of atmospheric gravity waves observed using the  
 1014 MU (Middle and Upper atmosphere) radar and GPS (Global Positioning Sys-  
 1015 tem) radio occultation. *Proceedings of the Japan Academy, Series B*, 90(1),  
 1016 12–27. doi: <https://doi.org/10.2183/pjab.90.12>
- 1017 van Caspel, W. E., Espy, P. J., Ortland, D. A., & Hibbins, R. E. (2022). The mid-  
 1018 to high-latitude migrating semidiurnal tide: Results from a mechanistic tide  
 1019 model and superdarn observations. *Journal of Geophysical Research: Atmo-*  
 1020 *spheres*, 127(1), e2021JD036007. doi: <https://doi.org/10.1029/2021JD036007>
- 1021 Vera Rodriguez, I., Näsholm, S. P., & Le Pichon, A. (2020). Atmospheric wind and  
 1022 temperature profiles inversion using infrasound: An ensemble model context.  
 1023 *The Journal of the Acoustical Society of America*, 148(5), 2923–2934. doi:  
 1024 <https://doi.org/10.1121/10.0002482>
- 1025 Vorobeva, E., De Carlo, M., Le Pichon, A., Espy, P. J., & Näsholm, S. P. (2021).  
 1026 Benchmarking microbarom radiation and propagation model against infra-  
 1027 sound recordings: a vespagram-based approach. *Annales Geophysicae*, 39(3),  
 1028 515–531. doi: <https://doi.org/10.5194/angeo-39-515-2021>
- 1029 Waugh, D. W., & Polvani, L. M. (2010). Stratospheric polar vortices. In *The strato-*  
 1030 *sphere: Dynamics, transport, and chemistry* (p. 43–57). American Geophysical  
 1031 Union (AGU). doi: <https://doi.org/10.1002/9781118666630.ch3>
- 1032 Waugh, D. W., Sobel, A. H., & Polvani, L. M. (2017). What is the polar vortex and  
 1033 how does it influence weather? *Bulletin of the American Meteorological Soci-*  
 1034 *ety*, 98(1), 37–44. doi: <https://doi.org/10.1175/BAMS-D-15-00212.1>
- 1035 Waxler, R., & Assink, J. (2019). Propagation modeling through realistic atmo-  
 1036 sphere and benchmarking. In *Infrasound monitoring for atmospheric studies*  
 1037 (pp. 509–549). Springer. doi: [https://doi.org/10.1007/978-3-319-75140-5\\_15](https://doi.org/10.1007/978-3-319-75140-5_15)
- 1038 Welch, P. (1967). The use of fast fourier transform for the estimation of power spec-  
 1039 tra: a method based on time averaging over short, modified periodograms.  
 1040 *IEEE Transactions on audio and electroacoustics*, 15(2), 70–73. doi:  
 1041 [10.1109/TAU.1967.1161901](https://doi.org/10.1109/TAU.1967.1161901)
- 1042 Wicker, W., Polichtchouk, I., & Domeisen, D. I. V. (2023). Increased vertical  
 1043 resolution in the stratosphere reveals role of gravity waves after sudden  
 1044 stratospheric warmings. *Weather and Climate Dynamics*, 4(1), 81–93. doi:  
 1045 [10.5194/wcd-4-81-2023](https://doi.org/10.5194/wcd-4-81-2023)
- 1046 Zhang, J., Limpasuvan, V., Orsolini, Y. J., Espy, P. J., & Hibbins, R. E. (2021).  
 1047 Climatological westward-propagating semidiurnal tides and their composite re-  
 1048 sponse to sudden stratospheric warmings in SuperDARN and SD-WACCM-X.  
 1049 *Journal of Geophysical Research: Atmospheres*, 126(3), e2020JD032895. doi:  
 1050 <https://doi.org/10.1029/2020JD032895>

# Probing gravity waves in the middle atmosphere using infrasound from explosions

Ekaterina Vorobeva<sup>1,2</sup>, Jelle Assink<sup>3</sup>, Patrick Joseph Espy<sup>1</sup>, Toralf Renkowitz<sup>4</sup>,  
Igor Chunchuzov<sup>5</sup>, Sven Peter Näsholm<sup>2,6</sup>

<sup>1</sup>Department of Physics, Norwegian University of Science and Technology, Trondheim, Norway

<sup>2</sup>NORSAR, Kjeller, Norway

<sup>3</sup>R&D Seismology and Acoustics, Royal Netherlands Meteorological Institute (KNMI), De Bilt, The

Netherlands

<sup>4</sup>Leibniz Institute of Atmospheric Physics, University of Rostock, Kühlungsborn, Germany

<sup>5</sup>Obukhov Institute of Atmospheric Physics, Moscow, Russia

<sup>6</sup>Department of Informatics, University of Oslo, Oslo, Norway

## Key Points:

- Ground-based infrasound recordings of explosions are used to retrieve effective sound speed fluctuations in the mesosphere
- Vertical wave number spectra of the retrieved fluctuations agree with the “universal” gravity wave saturation spectrum
- Infrasound from 49 explosions and radar data show that remote sensing of the middle atmosphere is possible via ground-based infrasound data

---

Corresponding author: Ekaterina Vorobeva, [ekaterina.vorobeva@ntnu.no](mailto:ekaterina.vorobeva@ntnu.no)

**Abstract**

This study uses low-frequency, inaudible acoustic waves (infrasound) to probe wind and temperature fluctuations associated with breaking gravity waves in the middle atmosphere. Building on an approach introduced by Chunchuzov et al., infrasound recordings are used to retrieve effective sound-speed fluctuations in an inhomogeneous atmospheric layer that causes infrasound backscattering. The infrasound was generated by controlled blasts at Hukkakero, Finland and recorded at the IS37 infrasound station, Norway in the late summers 2014 – 2017. Our findings indicate that the analyzed infrasound scattering occurs at mesospheric altitudes of 50 – 75 km, a region where gravity waves interact under non-linearity, forming thin layers of strong wind shear. The retrieved fluctuations were analyzed in terms of vertical wave number spectra, resulting in approximate  $k_z^{-3}$  power law that corresponds to the “universal” saturated spectrum of atmospheric gravity waves. The  $k_z^{-3}$  power law wavenumber range corresponds to vertical atmospheric scales of 33–625 m. The fluctuation spectra were compared to theoretical gravity wave saturation theories as well as to independent wind measurements by the Saura medium-frequency radar near Andøya Space Center around 100 km west of IS37, yielding a good agreement in terms of vertical wavenumber spectrum amplitudes and slopes. This suggests that the radar and infrasound-based effective sound-speed profiles represent low- and high-wavenumber regimes of the same “universal” gravity wave spectrum. The results illustrate that infrasound allows for probing fine-scale dynamics not well captured by other techniques, suggesting that infrasound can provide a complementary technique to probe atmospheric gravity waves.

**Plain Language Summary**

This study analyzes inaudible acoustic waves (infrasound) detected in Norway following explosions during disposal of military equipment in Finland. We show that infrasound reflects off small-scale structures in the middle atmosphere (within 50-75 km altitude) and we use signals recorded to retrieve so-called effective sound-speed profiles, a proxy of small-scale variations in temperature and horizontal wind. Spectral analysis of the retrieved altitude profiles reveals a power law associated with gravity waves. Such waves are important in the transfer of energy between atmospheric layers and are generated, for example, by upward air flow over mountain ranges. The vertical scales to which infrasound is sensitive to, are estimated to range from 33 to 625 m. Comparisons between spectra obtained using radar and infrasound show good agreement in terms of amplitudes and slopes. This suggests that the radar and infrasound-based effective sound-speed profiles represent different regimes of the same “universal” gravity wave spectrum. This study uses a large, consistent infrasound dataset and independent radar data to show that remote sensing of fine-scale wind and temperature variations in a region of the middle atmosphere for which very few observations are available, is possible by means of ground-based infrasound measurements.

**1 Introduction**

This study investigates the use of acoustic waves to probe fine-scale wind and temperature structures of the middle atmosphere (i.e. stratosphere and lower mesosphere). Atmospheric infrasound, i.e. low-frequency sound waves in the inaudible frequency range (< 20 Hz) can be generated by both natural (e.g., volcanoes, earthquakes, thunder) and artificial (e.g., rocket launches, sonic booms, blasts) sources. Once generated, infrasound waves can propagate in the atmosphere over long distances as the energy is ducted by waveguides formed by vertical gradients in temperature and wind (Brekhovskikh, 1960; Diamond, 1963). In addition to the source characteristics, infrasound waves also provide information about the medium through which they propagate, and can therefore serve

68 as a tool for atmospheric remote sensing (e.g., Le Pichon et al., 2005; Assink et al., 2019;  
69 Smets & Evers, 2014; Chunchuzov et al., 2022).

70 Probing the middle atmosphere by means of ground- and space-based remote sens-  
71 ing techniques contributes to a better representation of this region in atmospheric mod-  
72 els. The latter allows for improved weather forecasts due to the dynamical coupling be-  
73 tween different atmospheric layers (Shaw & Shepherd, 2008). The resolution of the at-  
74 mospheric model products, and therefore the scales of atmospheric processes resolved,  
75 strongly depends on available computational capabilities and the scientific problem. For  
76 example, high-resolution limited-area models routinely in use at national meteorologi-  
77 cal services (e.g., Bengtsson et al., 2017) have high horizontal resolution of several kilo-  
78 meters, however, the model top is typically in the lower stratosphere ( $\sim 10$  hPa, or 30  
79 km). In contrast, global numerical weather prediction models (NWP) and general cir-  
80 culation models (GCMs) with model tops raised into the mesosphere and above (Stocker  
81 et al., 2014) have lower resolution and are unable to resolve atmospheric processes at scales  
82 smaller than 10 kilometers in operational NWP (Bauer et al., 2015) and tens of kilome-  
83 ters in GCMs (H.-L. Liu et al., 2014; Becker et al., 2022). While not fully resolvable by  
84 models, these subgrid-scale processes can be observed by various observational techniques,  
85 including radar, lidar and rocket measurements (Rapp & Lübken, 2004; Le Pichon et al.,  
86 2015; Schäfer et al., 2020; Strelnikov et al., 2019).

87 One such subgrid-scale phenomenon is atmospheric gravity waves (GWs). Gener-  
88 ated in the lower atmosphere, GWs propagate into the middle atmosphere with increas-  
89 ing amplitude due to the decrease in air density with altitude, until they ultimately be-  
90 come unstable and break. When breaking, GWs generate small-scale eddies or turbu-  
91 lence which in turn interact with other atmospheric waves (Fritts & Alexander, 2003).  
92 The transfer of energy and momentum between different atmospheric layers is an im-  
93 portant function of atmospheric waves. For example, the middle atmospheric meridional  
94 circulation is primarily GW-driven (Fritts & Alexander, 2003) and breaking mesospheric  
95 GWs play an important role in the wintertime polar stratospheric downward motion (Garcia  
96 & Boville, 1994; Wicker et al., 2023). Momentum deposited by GWs (or GW drag) can  
97 modify atmospheric circulation patterns at lower altitudes, therefore affecting the weather  
98 and its prediction (McFarlane, 1987). This highlights the need for GW probing and for  
99 improvement of GW representation in NWP and GCMs. Efforts are also being made to  
100 develop GW-resolving GCMs stretching up to the edge of the thermosphere (e.g. H.-L. Liu  
101 et al., 2014; Becker et al., 2022).

102 GWs interact with other atmospheric waves in various ways, including wave-wave  
103 interaction and wave-breaking (Fritts & Alexander, 2003), and cause the presence of lo-  
104 calized, three-dimensional small-scale fluctuations in temperature and wind fields. These  
105 have been observed in the middle atmosphere by in-situ, ground- and space-based in-  
106 struments (e.g., Fritts & Alexander, 2003; Tsuda, 2014; Selvaraj et al., 2014; Bossert et  
107 al., 2015; Miller et al., 2015; Podglajen et al., 2022). The vertical scales of these fluctu-  
108 ations are significantly smaller than the horizontal scales, and have characteristic ver-  
109 tical length scales ranging from tens of meters to tens of kilometers (Gardner et al., 1993).  
110 The presence of such small-scale atmospheric fluctuations is known to affect propaga-  
111 tion and scattering of infrasound waves (Chunchuzov & Kulichkov, 2020). Moreover, it  
112 has been demonstrated by Bertin et al. (2014) and Lalande and Waxler (2016) that in-  
113 frasound waveguides are very sensitive to GW induced small-scale fluctuations in wind  
114 and temperature (see also Brissaud et al. (2023)). This implies the importance of account-  
115 ing for fine-scale atmospheric structures when modelling infrasound propagation (Drob  
116 et al., 2013; Hedlin & Drob, 2014; Chunchuzov et al., 2022). On the other hand, this also  
117 suggests that infrasound observations can be used to probe small-scale atmospheric fluctu-  
118 ations, thereby addressing the need for an enhanced observations of GWs (Cugnet et  
119 al., 2019).

The purpose of the current study is to quantify GW activity using a dataset of infrasound recordings from distant ground-based explosions. These signals have been recorded at a ground-based microbarometer array in Norway, every day during the period of mid-August to mid-September for the years 2014-2017. We apply a method that allows for the retrieval of so-called effective sound speed fluctuations in an inhomogeneous layer in the middle atmosphere. The method was developed over several years by Chunchuzov (2002); Chunchuzov et al. (2013, 2015, 2022); Chunchuzov and Kulichkov (2020). Based on the retrieved effective sound speed fluctuations for each event, we calculate the corresponding vertical wavenumber spectrum, and further interpret this in terms of power spectral density (PSD) slope and amplitude. The retrieved GW spectra are further compared to independent wind radar observations as well as to both linear and non-linear theoretical GW saturation models (Dewan & Good, 1986; S. A. Smith et al., 1987; Chunchuzov et al., 2015).

We exploit an infrasound dataset of signals generated by ground-based blasts in Hukkakero, Finland. These signals are detected at 321 km distance from the source, at microbarometer array IS37 in Northern Norway. This dataset has several attractive features making it suitable for atmospheric probing studies. First, the explosive events take place during August and September which is during the atmospheric transition from summer to winter, when the zonal component of the stratospheric winds reverses from westward to eastward (Waugh & Polvani, 2010; Waugh et al., 2017). Second, the known locations of the source and receiver together with the transient nature of the blasts make it possible to clearly identify arrivals from both stratospheric and from mesospheric – lower thermospheric (MLT) altitudes. Finally, yet importantly, the recurring nature of explosive events allows us to study day-to-day variability of the middle atmosphere dynamics.

The paper is organized as follows. A background on infrasound sensitivity to atmospheric structure, infrasound signal processing terminology, and previous studies exploiting Hukkakero explosion-related data is provided in Sect. 2. Section 3 describes the infrasound dataset, signal pre-processing, the SD-WACCM-X atmospheric model used, and the ray-tracing simulations conducted. Its subsection 3.4 elaborates the effective sound speed retrieval methodology. The obtained results are shown in Sect. 4, also further discussed in Sect. 5 including vertical wavenumber spectrum comparison to independent radar measurements and theoretical models.

## 2 Background

### 2.1 Sensitivity of infrasound to atmospheric structure

Infrasound propagation is sensitive to spatial variations in temperature and wind (e.g., Waxler & Assink, 2019). In the direction of propagation, the wind and temperature related propagation effects can approximately be modelled using the concept of effective sound speed,  $C_{\text{eff}}(z)$ , defined as:

$$C_{\text{eff}}(z) = \sqrt{\gamma RT} + \mathbf{u} \cdot \hat{n}, \quad (1)$$

where,  $\gamma$ ,  $R$ ,  $T$ ,  $\mathbf{u}$  and  $\hat{n}$  correspond to the adiabatic index, the gas constant, the absolute temperature, the horizontal wind speed vector and the direction of propagation, respectively. In the infrasound-related context, it is often appropriate to approximate  $\sqrt{\gamma R} \approx 20 \text{ m s}^{-1} \text{ K}^{-1/2}$ . For cases where ground-to-ground propagation is of interest, it is convenient to introduce the effective sound speed ratio, which is obtained by normalizing  $C_{\text{eff}}(z)$  by its value on the ground and which is analogous to the more familiar refractive index. From classical ray theory, acoustic signals that originate from the ground are expected to traverse in waveguides between the ground and the altitudes for which the  $C_{\text{eff}}$  ratio exceeds unity.

164 The celerity is defined as the source-receiver great-circle distance divided by the  
 165 infrasound travel time (i.e., the difference between the arrival time and origin time). The  
 166 celerity can hence be considered as the average group speed of a guided acoustic wave.  
 167 When the origin time and location are known, celerity-based models can be used to pro-  
 168 vide information about the infrasound waveguide through which an acoustic wave prop-  
 169 agated. Infrasonic paths with a substantial vertical component have a group speed that  
 170 is significantly lower than the speed of sound. Conversely, infrasound guided by tropo-  
 171 spheric waveguides (that propagates in the troposphere) has a celerity near the local sound  
 172 speed. Typical celerities for different waveguides are 310–330 m/s for tropospheric ar-  
 173 rivals, 280–320 m/s for stratospheric arrivals, and 180–310 m/s for mesospheric and  
 174 thermospheric arrivals (e.g., Nippress et al., 2014; Lonzaga, 2015).

## 175 2.2 Infrasound array processing

176 An infrasound array is a group of microbarometers distributed in space but installed  
 177 close enough so that the received sensor signals are sufficiently coherent to estimate the  
 178 wavefront parameters of the dominant plane wave arriving at the array. This is done us-  
 179 ing array signal processing techniques that delay and sum sensor traces according to a  
 180 model for the inter-element delays. This spatial filtering allows for reducing incoherent  
 181 noise and for separating acoustic signals from different directions of arrival. Identifica-  
 182 tion of the signals of interest is typically based on the observed back-azimuth, apparent  
 183 velocity, and average inter-sensor coherence. The back-azimuth represents the direction  
 184 from which the plane wave arrives at the array and is measured in degrees clockwise from  
 185 the North. The apparent velocity is the velocity the plane wave appears to travel at hor-  
 186 izontally along the array. This parameter is estimated based on the time delays between  
 187 sensors (as well as back-azimuth) and contains information about the angle of incidence  
 188  $\theta$  of the plane-wave,  $v_{\text{app}} = c / \sin \theta$  where  $c$  is the local sound speed. There is no unique  
 189 relationship between apparent velocity and altitude from which signal arrives, however  
 190 higher values of apparent velocity would normally indicate arrival from higher altitudes.  
 191 The combination of back-azimuth and travel time allows for signal identification and in-  
 192 frasound source location, while  $v_{\text{app}}$  helps to identify the incidence angle of the ray-path  
 193 at the ground.

## 194 2.3 The Hukkakero blasts in infrasound studies

195 The site of Hukkakero, Finland (67.94° N, 25.84° E; Fig. 1), has been of particu-  
 196 lar interest for infrasound related studies over the past years. At Hukkakero, blasts re-  
 197 lated to the disposal of military explosives occur yearly since 1988 in August-September,  
 198 typically once a day with a yield of around 20 tons of TNT equivalent (Gibbons et al.,  
 199 2015). In addition to generating an atmospheric pressure wave, these explosions produce  
 200 clear seismic signals which allow for the accurate estimation of origin time and location  
 201 by means of seismic localization techniques (Gibbons et al., 2020). Blixt et al. (2019)  
 202 showed that the ARCES seismic array in northern Norway records, besides the seismic  
 203 waves also the ground-coupled airwaves associated with Hukkakero explosions. These  
 204 explosions are also well-represented in event bulletins like the comprehensive European  
 205 Infrasound Bulletin (Pilger et al., 2018, Fig. 10), as well as in the Comprehensive Nuclear-  
 206 Test-Ban Treaty (CTBT) bulletin products.

207 Infrasound signals that originated from Hukkakero explosions have been exploited  
 208 in several atmospheric probing studies. Blixt et al. (2019) analyzed 30 years of Hukkakero  
 209 explosions detected at the ARCES/ARCI seismo-acoustic array (Norway) in terms of back-  
 210 azimuth deviation due to cross-wind (the component of wind perpendicular to the di-  
 211 rection of propagation) influence along the propagation path. The resulting cross-wind  
 212 estimates obtained showed a good agreement with the European Centre for Medium-Range  
 213 Weather Forecasts (ECMWF) Reanalysis (ERA)-Interim model. Amezcua et al. (2020)  
 214 presented a way to implement an off-line assimilation of infrasound data into atmospheric

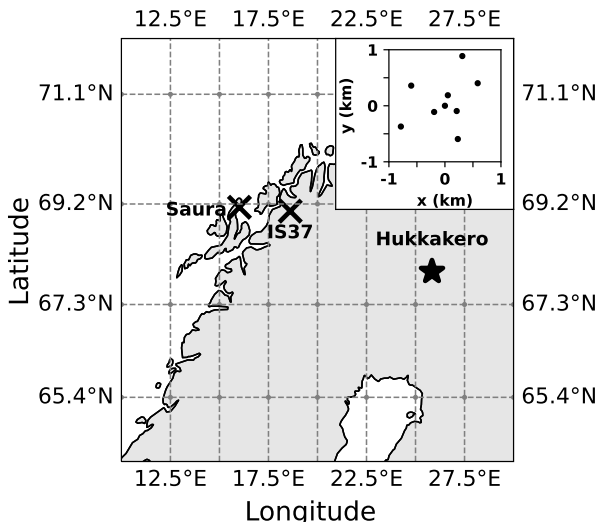


**Figure 1.** Location of all sources of data used in this study: Hukkakero explosion site, IS37 infrasound array, and Saura medium-frequency radar. The SD-WACCM-X atmospheric model grid is displayed on the map as gray dashed lines. The IS37 array layout is shown in the inset.

215 models using Ensemble Kalman filters. The study extends the approach by Blixt et al.  
 216 (2019), demonstrating that assimilation of back-azimuth deviation allows for corrections  
 217 to atmospheric winds at tropospheric and stratospheric altitudes. Based on the same dataset,  
 218 Vera Rodriguez et al. (2020) developed an extended inversion methodology that uses in-  
 219 frasound observations to update atmospheric wind and temperature profiles on the ba-  
 220 sis of the ERA5 re-analysis ensembles.

221 Still, Hukkakero related infrasound signals have not previously been used to probe  
 222 small-scale atmospheric inhomogeneities.

### 223 3 Materials and Methods

#### 224 3.1 Infrasound dataset and signal pre-processing

225 This study exploits Hukkakero explosions and the associated signals recorded at  
 226 infrasound array IS37 that is located at  $\sim 320$  km distance in Bardufoss, Norway (69.07°  
 227 N, 18.61° E; Fig. 1). This 10-element array is part of the International Monitoring Sys-  
 228 tem (IMS) for the verification of the CTBT (Marty, 2019). The region is also host to  
 229 a cluster of additional seismo-acoustic monitoring stations (Gibbons et al., 2015). Dur-  
 230 ing the years 2014 – 2017, 57 explosions took place at Hukkakero, however 8 of them  
 231 (the three last explosions in 2014 and the five last explosions in 2016) were significantly  
 232 weaker (Gibbons et al., 2015) and are therefore not considered in the current study. Ori-  
 233 gin times of the analyzed 49 explosions are tabulated in Appendix A.

234 For each explosion, the back-azimuth and apparent velocity of the dominant wave-  
 235 front were estimated using a conventional time-domain array processing technique (Melton  
 236 & Bailey, 1957). The detection of coherent infrasound over the array is based on the eval-  
 237 uation of the so-called Fisher ratio. The Fisher ratio corresponds to a probability of de-  
 238 tection of a coherent signal with a specific signal-to-noise ratio (SNR). The associated  
 239 inter-element time-delays are used to form the so-called best-beam, for which the indi-  
 240 vidual array recordings are time-aligned before summation. Details on the particular im-

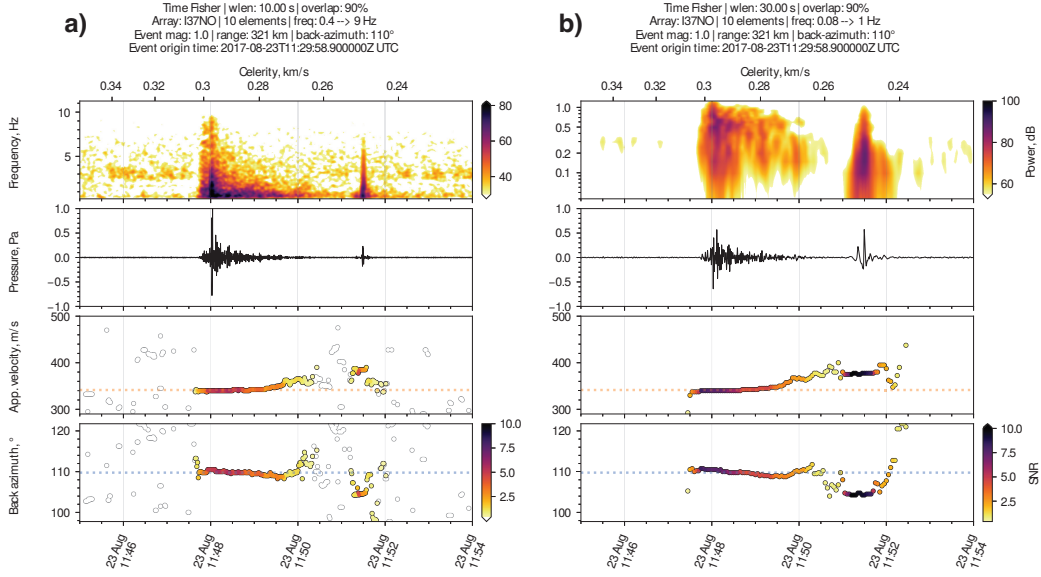


**Figure 2.** Array processing results for a Hukkakero explosion on 23 August 2017, processed between a) 0.4 – 9 Hz and b) 0.08 – 1.0 Hz. Top panel: spectrogram displayed in decibel. Second panel: the best-beam trace with an orange dashed line indicating the sound speed on the ground ( $\approx 340$  m/s). Third panel: apparent velocity. Bottom panel: the back-azimuth, where the blue dashed line corresponds to the great-circle back-azimuth ( $110^\circ$ ) towards Hukkakero.

241 plementation can be found in Evers (2008). The beam waveforms were processed in two  
 242 partly overlapping frequency bands to highlight the key trace features, 0.4–9 Hz and  
 243 0.08 – 1.0 Hz. Figure 2 shows array analysis results for one explosion filtered in both  
 244 frequency bands. Note, the contribution of ocean ambient noise (“microbaroms”) around  
 245 0.2 Hz (Vorobeva et al., 2021; De Carlo et al., 2020) and wind noise at low frequencies  
 246 is negligible compared to the explosion contributions.

247 Fig. 3 shows a compilation of IS37 infrasound signals from the 49 explosions ex-  
 248 ploited in the current study. The first arrivals are detected between 17.5–19 minutes  
 249 (celerity of 281–314 m/s) after the explosion (Fig. 3a) and feature energy in a broad  
 250 frequency band (Fig. 2a). Typically, the waveform consists of a main arrival with a sig-  
 251 nificantly larger amplitude, followed by a coda (“tail”) with progressively increasing ap-  
 252 parent velocity with values within the 340–360 m/s. These ranges of celerities and ap-  
 253 parent velocities are typical for stratospheric arrivals (Nippress et al., 2014; Lonzaga, 2015)  
 254 which generally refract or reflect near the stratopause. Similarly extended wave trains  
 255 have been observed in far-field infrasound recordings following large detonations (Fee et  
 256 al., 2013; Lalande & Waxler, 2016; Green et al., 2018), and it was assumed that these  
 257 wave trains originate from interactions with atmospheric perturbations caused by GWs.

258 After this first wave train, a later arrival can in many cases be observed between  
 259 approximately 20–23 min after the explosion (a celerity range of 232–267 m/s). Figs. 2b  
 260 and 3b show the signals in a pass-band between 0.08 – 1.0 Hz. This arrival is charac-  
 261 terized by a low-frequency U-shaped waveform, has higher apparent velocity values (i.e.,  
 262  $> 360$  m/s) and larger back-azimuth deviations compared to the first arrival. All of these  
 263 characteristics are typical of arrivals returning from the lower thermosphere (Le Pichon  
 264 et al., 2005; Assink et al., 2012, 2013; Green et al., 2018; Blom & Waxler, 2021).

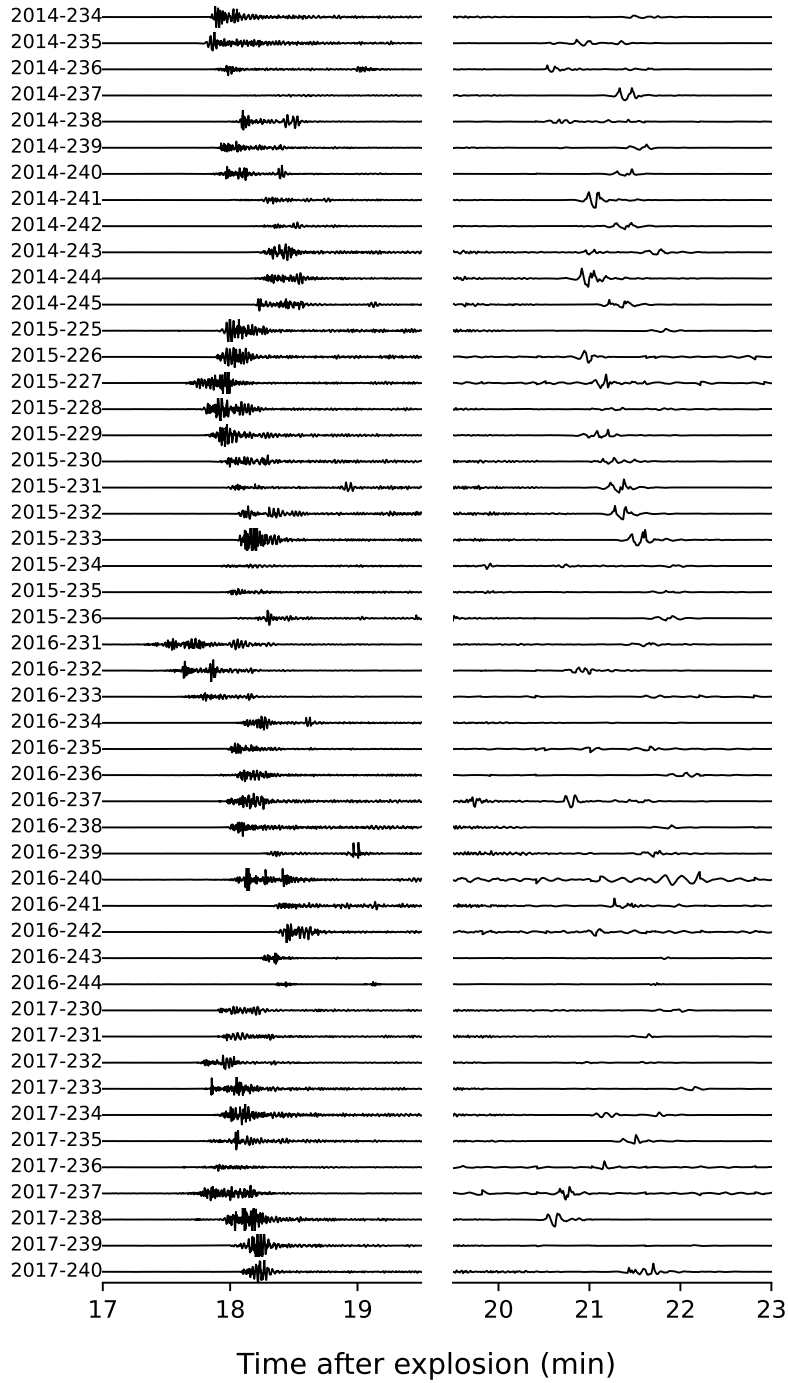


**Figure 3.** Infrasonic signals from 49 Hukkakero explosions that occurred in the time period 2014-2017. The signals have been recorded at infrasound array IS37 between (left) 17 – 19.5 minutes and (right) 19.5 – 23 minutes. The data are band-pass filtered between (left) 0.4 – 9 Hz and (right) 0.08 – 1 Hz. The y-axis of each trace has  $\pm 1$  Pa limit. The left-hand side labels display the year and the day-of-year when events took place.

265 A closer look at Figure 3 further reveals that several of the events feature an ar-  
 266 rival between the stratospheric and thermospheric arrivals, see also Gibbons et al. (2019,  
 267 Fig. 10.7). Although the current study only exploits the stratospheric arrivals for atmo-  
 268 spheric probing, it is worth noting the potential for further analysis and probing based  
 269 on later arrivals in the wavetrains, for example as demonstrated in Chunchuzov et al.  
 270 (2011).

### 271 3.2 The SD-WACCM-X atmospheric model

272 In this study, the Whole Atmosphere Community Climate Model with thermosphere  
 273 and ionosphere extension (WACCM-X; H.-L. Liu et al., 2018) is used as a model atmo-  
 274 sphere. The particular version is the *specified dynamics*, SD-WACCM-X, version v2.1  
 275 (Sassi et al., 2013), for which the temperature and winds are nudged by the Modern-Era  
 276 Retrospective analysis for Research and Applications, Version 2 (MERRA-2; Gelaro et  
 277 al., 2017) from the ground up to  $\sim 50$  km. Above that altitude, WACCM-X is free-running.  
 278 While WACCM-X extends up to about 500–700 km altitude (145 levels), we only con-  
 279 sider the altitude region relevant for infrasound propagation, which is up to 140 km al-  
 280 titude. The model has grid cells of  $1.9^\circ \times 2.5^\circ$  in latitude-longitude and a 3-h tempo-  
 281 ral resolution (see the Data availability Section). For a detailed description of chemical  
 282 and physical processes and parameterizations included in the model, see the studies by  
 283 H.-L. Liu et al. (2018); J. Liu et al. (2018).

284 The WACCM-X model has been validated against observations and empirical mod-  
 285 els and has shown a good agreement in thermospheric composition, density and tidal am-  
 286 plitudes (H.-L. Liu et al., 2018). The SD-WACCM-X model has been found to be rep-  
 287 resentative of the Earth’s atmosphere in studies of different atmospheric phenomena: e.g.,  
 288 elevated-stratopause events (Siskind et al., 2021; Orsolini et al., 2017), dynamics (Kumari  
 289 et al., 2021), atmospheric tides (Pancheva et al., 2020; Zhang et al., 2021; van Caspel  
 290 et al., 2022). In contrast to other models routinely used for infrasound propagation, SD-  
 291 WACCM-X provides a single consistent atmospheric model covering the altitude region  
 292 relevant for long-range infrasound propagation, with a suitable spatio-temporal resolu-  
 293 tion. In particular, WACCM should provide a more physical description of the MLT re-  
 294 gion when compared to atmospheric specifications that are typically used for thermo-  
 295 spheric arrival modeling, such as the HWM/MSIS climatological models (Drob, 2019).

296 Due to the proximity of the source to the receiver, the atmosphere can be approx-  
 297 imated as a 1-D layered medium without time dependence. To avoid interpolation in space  
 298 and time, we extract pressure, temperature, zonal and meridional winds from the grid  
 299 node closest to the explosion site (Fig. 1) and the time step closest to the explosion ori-  
 300 gin time. The atmospheric conditions for all 49 Hukkakero events are presented in Fig. 4.  
 301 Zonal and meridional winds in the stratosphere (20–50 km) are weak and have abso-  
 302 lute values of up to 18 m/s. Their variation from explosion to explosion is negligible with  
 303 standard deviation of 1–5 m/s. This can be explained by the summer-to-winter tran-  
 304 sition in the stratospheric polar vortex where zonal wind is reversing from the westward  
 305 summer circulation to the eastward winter circulation (Vaugh & Polvani, 2010; Vaugh  
 306 et al., 2017). In contrast, atmospheric winds in the mesosphere - lower thermosphere (50–  
 307 120 km) reach values of up to 100 m/s and vary strongly between explosions (standard  
 308 deviation of up to 33 m/s) (A. K. Smith, 2012).

309 Figure 4 also shows  $C_{\text{eff}}(z)$  ratio profiles (see Sect. 3.1) that have been computed  
 310 using the SD-WACCM-X model (see Sect. 2). It can be seen that around 50 km altitude  
 311 the ratio is close but does not exceed unity for most profiles, except for the events on  
 312 13 and 14 Aug 2015 (days 225 and 226). This indicates that the presence of a strong strato-  
 313 spheric waveguide for the Hukkakero-IS37 configuration in late summer is rather rare and  
 314 therefore (strong) stratospheric returns would not be expected at IS37. In contrast, the  
 315 effective sound speed ratio exceeds unity around lower thermosphere in all cases. This

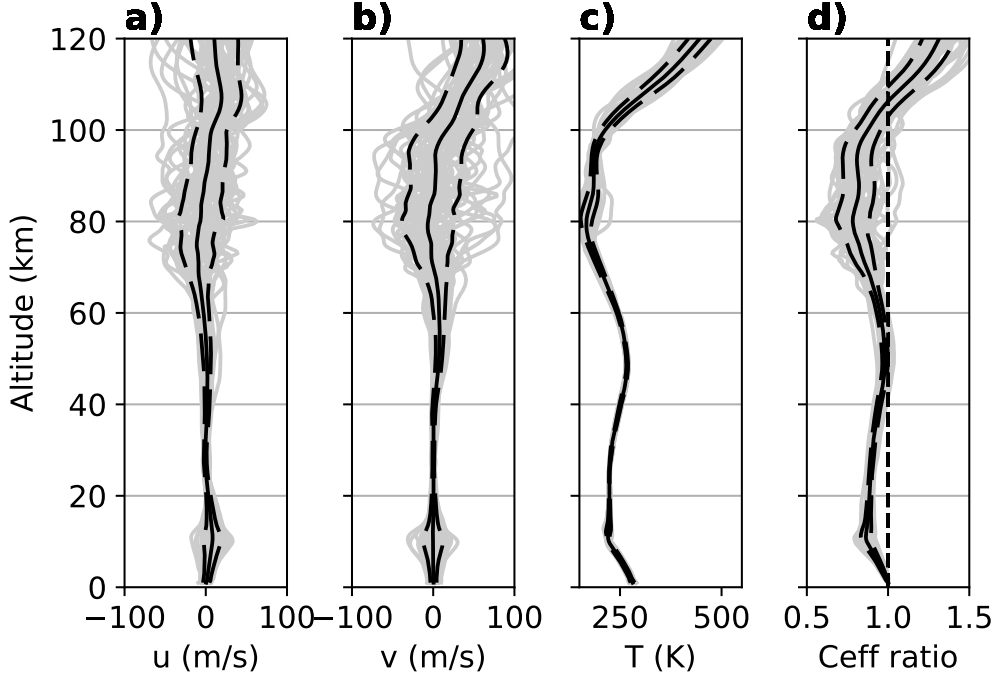


**Figure 4.** SD-WACCM-X atmospheric specifications for the 49 analyzed Hukkakero explosions, extracted at the grid point closest to the site around the time of the explosion. a) zonal wind, b) meridional wind, c) temperature, d) effective sound speed ratio.

316 can be attributed to the strong temperature gradient, which guarantees the presence of  
 317 a thermospheric waveguide.

318 The effects of small-scale atmospheric fluctuations on stratospheric arrivals is particu-  
 319 larly enhanced during periods of the year when the  $C_{\text{eff}}$  ratio near the stratopause  
 320 is close to unity (Assink et al., 2014). Under these conditions, the small perturbations  
 321 (e.g., gravity waves induced wind and temperature perturbations) can cause conditions  
 322 favorable for i) refraction or ii) reflection. The propagation effects (refraction or reflec-  
 323 tion) strongly depend on the vertical scale of the atmospheric fluctuations in compar-  
 324 ison to the infrasonic wavelength. For relatively large vertical scales, refraction of infra-  
 325 sonic waves can be simulated with ray theory, showing variations in travel time and back-  
 326 azimuth (Kulichkov, 2010). In contrast, infrasound scattering (or partial reflection) on  
 327 vertical scales comparable to the infrasonic wavelength is a full-wave effect that cannot  
 328 be simulated using ray theory. However, several studies (Chunchuzov & Kulichkov, 2020;  
 329 Green et al., 2018; Blixt et al., 2019) have reported observations of partial reflections from  
 330 stratospheric altitudes in the region where no stratospheric rays are predicted (i.e., the  
 331 shadow zone).

### 332 3.3 Ray-tracing using the SD-WACCM-X model

333 For each of the analyzed Hukkakero events, we simulated infrasound propagation  
 334 through its SD-WACCM-X atmospheric profile using the InfraGA ray tracer in 2-D Carte-  
 335 sian mode (see the Data availability Section for links and references). Rays were launched  
 336 from the location of Hukkakero in the direction of IS37 with inclination angles ranging  
 337 from 0 to 60 degrees measured from the horizontal.

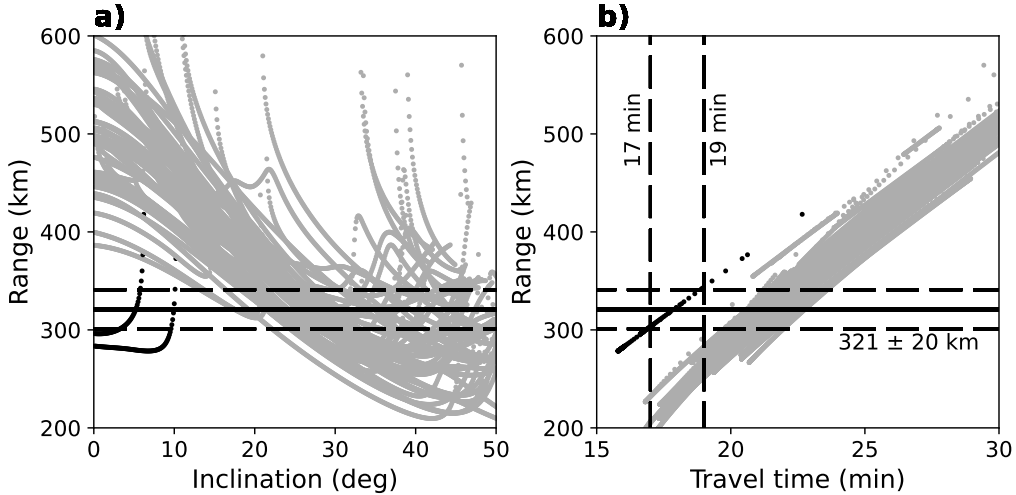


**Figure 5.** The first ground intercept information predicted by InfraGA for all explosive events. a) Eigenray departure inclination versus the distance from the source, b) travel time versus distance from the source. The eigenray turning height is color coded ( $< 60$  km - black dots,  $\geq 60$  km - gray dots). The Hukkakero-IS37 great-circle distance and the tolerance distance interval considered for ground intercept are indicated as a solid black line and dashed black lines, respectively. Observed travel time of the first arrival at IS37 is between 17 and 19 min (dashed black lines).

338 Fig. 5a shows ray departure inclination angle against distance from Hukkakero for  
 339 refracted paths predicted by ray theory. Almost all of the predictions correspond to ther-  
 340 mospheric refracted paths with turning heights in the lower thermosphere, near  $\sim 100$   
 341 km (gray dots). As was mentioned before, these thermospheric arrivals are often observed  
 342 at IS37 station Fig. 3. Fig. 5b shows the corresponding travel time (in min) for these rays.  
 343 Stratospheric arrivals with arrival times between 17-19 min that correspond to our ob-  
 344 servations (Fig. 3) are only predicted for two events that occurred on 13 and 14 August  
 345 2015 (days 225 and 226). It follows from analysis of the SD-WACCM-X profiles (Fig. 4),  
 346 that for these two days the  $C_{\text{eff}}(z)$  ratio exceeds unity in the stratosphere.

347 From the ray-tracing simulations, it can be concluded that i) IS37 is located in a  
 348 stratospheric shadow zone (i.e. there is no refraction-supported stratospheric duct) for  
 349 the vast majority of cases and ii) refracted infrasound reaches the station via thermo-  
 350 spheric ducts. Therefore, it is presumed that the stratospheric signals arrive at IS37 sta-  
 351 tion after being partially reflected in the middle atmosphere (Kulichkov, 2010; Chunchu-  
 352 zov et al., 2011).

353 Fig. 6 illustrates the raypaths of a stratospheric and a thermospheric arrival at IS37  
 354 for the analyzed Hukkakero events. The  $C_{\text{eff}}(z)$ -ratio profile shown in the figure is com-  
 355 puted based on the SD-WACCM-X model for 22 August 2017 at 12:00 UTC. The only  
 356 arrival predicted by ray tracing is a thermospheric refracted ray that propagates up to  
 357 113 km and is predicted to arrive at IS37 after  $\sim 22$  minutes, which matches the ob-  
 358 servations (see Fig. 3).

359 The reflected rays are not predicted by the classical ray theory but are instead con-  
 360 structed using a mirroring procedure akin to the approach in, e.g., Blixt et al. (2019).  
 361 We trace all rays until they reach the midpoint between Hukkakero and IS37 and then

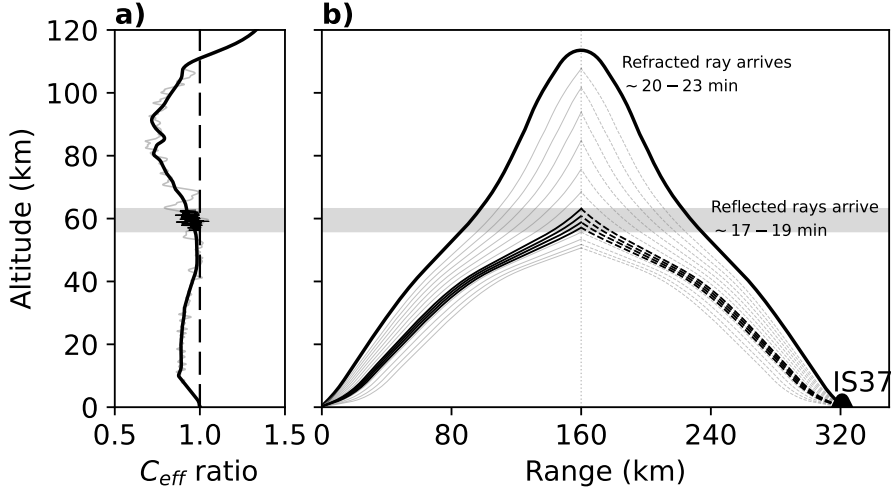


**Figure 6.** A schematic representation of infrasound raypaths from Hukkakero to IS37 relevant to this study. a) Effective sound speed ratio in direction of IS37 with a conceptual gravity wave perturbations (gray) and inhomogeneous layer of  $C_{\text{eff}}(z)$  fluctuations (black). b) Thermospheric ducting simulated by ray theory and explaining later arrivals (20-23 min) with U-shape (thick black line). Earlier arrivals (17-19 min) that are not predicted by ray theory can be explained by infrasound being scattered by small-scale  $C_{\text{eff}}(z)$  fluctuations in an atmospheric layer (dashed black lines).

362 mirror them to continue the path back to the surface. Due to acoustic reciprocity, this  
 363 is a valid approach in a range-independent medium. It is hypothesized that these rays  
 364 have scattered from an atmospheric layer with small-scale fluctuations in wind and  
 365 temperature. The travel time is then estimated as twice the propagation time to the mid-  
 366 point. The altitude range of the reflective layer is defined from the two rays that match  
 367 best the observed beginning and ending of the processed infrasound signal. In case of  
 368 a large discrepancy between the predicted and observed travel time for the lower bound-  
 369 ary, we calculate the lower layer altitude as  $z_j = z_{\text{top}} - C_{\text{eff}}(t_{\text{end}} - t_{\text{obs},j})$ , assuming a  
 370 constant effective sound speed in the layer. Here  $z_{\text{top}}$  is the upper boundary of the re-  
 371 flective layer obtained from ray tracing calculations,  $t_{\text{obs},j}$  is a set of discrete times de-  
 372 scribing the observed travel time of the arrival,  $t_{\text{end}}$  is the end of the analyzed signal win-  
 373 dow.

### 374 3.4 Effective sound speed retrieval

375 We applied the approach of Chunchuzov et al. (2015) to retrieve fine-scale effec-  
 376 tive sound-speed variations in the middle atmosphere. This method was designed to be  
 377 applied to stratospheric and thermospheric arrivals in the shadow zone, assuming that  
 378 infrasound was scattered from inhomogeneous atmospheric layers with fine-scale  $C_{\text{eff}}(z)$   
 379 fluctuations. It was demonstrated in (Chunchuzov et al., 2013) that temperature vari-  
 380 ations contribute relatively little to the effective sound-speed fluctuations ( $\sim 20\%$ ) com-  
 381 pared to wind variations ( $\sim 80\%$ ). Therefore, we associate  $C_{\text{eff}}(z)$  fluctuations with vari-  
 382 ations in horizontal wind.

383 This section presents the salient details behind the algorithm for the retrieval pro-  
 384 cedure, and provides a description of the main underlying assumptions. For a more de-

385 tailed derivation of the equations and discussion of the method, we refer to (Chunchuzov  
 386 et al., 2015; Chunchuzov & Kulichkov, 2020; Chunchuzov et al., 2022). For convenience,  
 387 most nomenclature and designations used in the current study are the same as in these  
 388 original studies.

389 The fine-scale effective sound-speed inversion approach is based on:

- 1) The assumption that infrasound is scattered or partially reflected at the midpoint between the source and receiver in a moving atmospheric layer with vertical fluctuations in the effective refractive index,

$$\varepsilon(z) = -2(\Delta c + \Delta u \sin \theta_0)/(c_1 \cos^2 \theta_0), \quad (2)$$

390 where  $\Delta c$  are the sound speed fluctuations;  $\Delta u$  is the projection of wind fluctu-  
 391 ations on the source-receiver radius vector;  $c_1$  is the average sound speed in the  
 392 layer; and  $\theta_0$  is the angle of incidence on the layer at altitude  $z$ . The effective re-  
 393 fractive index,  $\varepsilon(z)$ , is assumed to be non-zero only inside the moving layer. A de-  
 394 tailed derivation of Eq. 2 is provided in Appendix B.

- 2) The relationship between the vertical profile of the effective refractive index fluctu-  
 395 ations,  $\varepsilon(z)$ , and the scattered signal waveform,  $p'(t)$  is:

$$p'(t) = -\frac{p'_m r_0}{4R_1} \int_{-\infty}^{\infty} f(t - R_1/c_1 - z/a) \frac{d\varepsilon(z')}{dz'} dz', \quad (3)$$

397 where  $p'_m$  is the peak signal amplitude recorded at distance  $r_0$  close to the source;  
 398  $R_1$  is the total distance along the propagation path;  $f(t)$  is the normalized acous-  
 399 tic pressure waveform at  $r_0$ ;  $a = c_1/(2 \cos \theta_0)$  is a coefficient representing the speed  
 400 of the infrasound in the refractive layer; and  $d\varepsilon(z)/dz$  is the spatial derivative of  
 401  $\varepsilon(z)$ . The dimensionless waveform of the scattered signal is defined as  $I_0(t) = p'(t)R_1/(p'_m r_0)$ .

- 3) The assumption that the initial signal waveform,  $f(t)$ , has an N-wave shape (Lonzaga  
 402 et al., 2015) near the source and a duration  $T_0$  at the reflective layer altitude.

404 After integrating Eq. 3 and solving the resulting equation (more details in Chunchuzov  
 405 and Kulichkov (2020)), the relation between the effective refractive index profile and the  
 406 dimensionless waveform of the scattered signal becomes

$$I_0(t) = -\frac{\varepsilon(a[t - R_1/c_1]) + \varepsilon(a[t - R_1/c_1 - T_0])}{4}. \quad (4)$$

407 Equation 4 can be solved numerically for a set of discrete time samples with respect  
 408 to  $\varepsilon(z)$  using the method of least squares (see Appendix A for details). Next, the effec-  
 409 tive sound speed fluctuations,  $\Delta C_{\text{eff}}(z)$ , can be estimated from the  $\varepsilon(z)$  profile using Eq. 2  
 410 (Appendix B). However, several parameters need to be specified before solving Eq. 4:

- 411 • The average sound speed  $c_1$  is obtained by matching the travel time predicted by  
 412 ray-tracing simulations to the observed travel time, and thereby determining the  
 413 altitude range of the reflective layer and averaging the sound speed within it, as  
 414 well as angle  $\theta_0$ .
- 415 • An estimate of the peak overpressure close to the source,  $p'_m$ , is obtained using  
 416 the model by Kinney and Graham (1985) based on the blast yield. The typical  
 417 yield of Hukkakero explosions is presumed to be approximately 20 ton of TNT equiv-  
 418 alent (Gibbons et al., 2015). According to the Kinney and Graham (1985) model  
 419 with the initial conditions  $W = 20$  ton TNT,  $P_{\text{ref}} = 1.01325 \cdot 10^5$  Pa, and  $\rho_{\text{ref}} =$   
 420  $1.225 \text{ kg/m}^3$  (Atmosphere, 1976), the peak overpressure at  $r_0 = 1$  km from the  
 421 source becomes  $p'_m = 2320$  Pa.
- 422 • As the initially generated shock wave propagates, it experiences attenuation and  
 423 becomes distorted due to non-linear propagation effects, which become more promi-  
 424 nent with increasing height due to decreasing atmospheric density with altitude

(Lonzaga et al., 2015; Blom & Waxler, 2021). One of the distortion features associated with non-linear propagation is period lengthening, which occurs since positive and negative phases of the pressure wave travel at slightly different speed (Hamilton & Blackstock, 2008). This contributes to decreasing the amplitude of the acoustic pulse as its duration increases following the acoustic-pulse conservation law (Kulichkov et al., 2017). To get an estimate of the N-wave duration at the reflective layer altitude, weakly non-linear propagation simulations were performed using InfraGA. Properties of the initially generated shock wave (peak overpressure of 2320 Pa and positive pressure phase of 0.11 s) were calculated based on the Kinney and Graham (1985) model described above. Values of  $T_0$  in the range of 1–2 s were found to correspond to altitudes in the range of 50–80 km. This is the region from where we expect rays to reflect from, following the travel-time based mirroring simulations as described in Sect. 3.3.

## 4 Results

This study analyzes the first (stratospheric) Hukkakero arrivals in the infrasound recordings described in Sect. 3.1 and illustrated in Fig. 3. For the 49 Hukkakero blasts investigated, we processed a 30 second segment of the infrasound best-beam signal traces using the recipe provided in Sect. 3.4. Figure 7 displays the  $\Delta C_{\text{eff}}(z)$  profiles retrieved. There is a day-to-day variability in the reflective layer altitude, with all  $\Delta C_{\text{eff}}(z)$  profiles being located within stratopause–lower mesosphere altitudes of 50 – 75 km with the average depth of  $7.75 \pm 0.38$  km. Previous studies demonstrate that infrasound signal characteristics observed for events with similar strength and source-receiver geometry are highly sensitive to varying middle atmospheric winds and temperatures (Le Pichon et al., 2002; Drob, 2019; Averbuch et al., 2022). Therefore, the difference in the arrival time between events, as displayed in Fig. 3, can be related to the variation in the infrasound probing altitude. This is confirmed by the overall agreement in the arrival time variations for the explosions studied and the associated altitude variation of the retrieved fluctuation profiles, see Fig. 7. It should be noted that the same  $\Delta C_{\text{eff}}(z)$  retrieval procedure can also be applied to later arrivals, which correspond to higher altitudes, as demonstrated in Chunchuzov et al. (2022).

The majority of the effective sound-speed fluctuations retrieved,  $\Delta C_{\text{eff}}(z)$ , have amplitudes of up to 5 m/s. However, for some cases, the amplitudes reach up to 15 m/s. Exceptionally high  $\Delta C_{\text{eff}}(z)$  amplitudes of up to 25 m/s are estimated from the waveform recorded on 27 August 2016 (day 240 shown as the gray profile in Fig. 7). There are two reasons behind it. First, the signal amplitude reaches 2 Pa which is larger than for any other event. Second, rapid changes in the waveform amplitude make it difficult for the fitting procedure to find an appropriate solution (see Appendix B). We consider this event as an outlier and suggest that it should be interpreted as a refracted rather than reflected arrival, and therefore remove it from the analysis.

The root-mean-square error (RMSE) of  $\Delta C_{\text{eff}}(z)$  retrieved varies within 6–18% (see Appendix A). This RMSE is calculated based on the difference between the left- and right- hand sides of Eq. 4 (see Appendix B for details).

Next, we perform a vertical wavenumber spectral analysis of the retrieved  $\Delta C_{\text{eff}}(z)$  profiles by estimating the PSD using Welch’s method (Welch, 1967) with a Hamming window (window length of 750 m or 50 samples and 50% overlap). Figure 8 displays the vertical wavenumber power spectral density of the retrieved effective sound-speed fluctuation profiles, as well as their mean. It can be seen that negative PSD slope is present for all events. The vertical wavenumber,  $k_z$ , that corresponds to the beginning of the negative slope is denoted the dominant wavenumber,  $m_*$ . Based on the analyzed events,  $m_* = 2.15 \cdot 10^{-3} \pm 4.4 \cdot 10^{-4}$  cycles/m (see Appendix A). Fitting the  $k_z^p$  power-law within

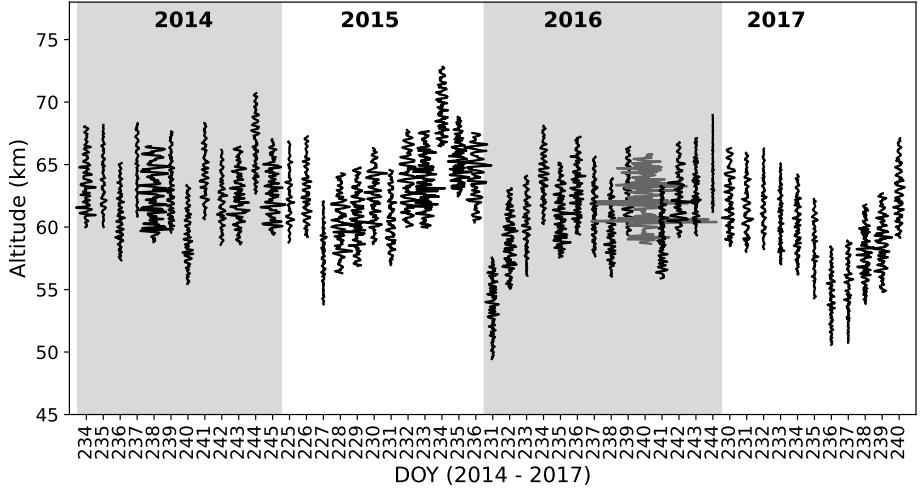


**Figure 7.** Retrieved fluctuations of the effective sound speed  $C_{\text{eff}}(z)$ . The  $C_{\text{eff}}(z)$  profile on 27 August 2016 (day 240) with exceptionally high values (more details in the text) is displayed in gray to avoid overlapping with other profiles.

475  $k_z > m_*$  provides an estimate of  $p = -3.35$  for the mean PSD and  $p = -3.50 \pm 0.39$   
 476 for all profiles (see Appendix A).

477 The power-law exponents obtained in this study are close to the  $k_z^{-3}$  power-law which  
 478 is known to correspond to the “universal” spectrum of horizontal wind fluctuations in-  
 479 duced by gravity waves or gravity wave saturation spectrum (Fritts & Alexander, 2003).  
 480 Various theories were proposed to explain the dynamics behind gravity wave saturation,  
 481 i.e., instability and wave-wave interaction. The saturation spectrum amplitude was shown  
 482 to correspond to  $CN^2k_z^{-3}$  with  $C$  typically varying within 0.1 – 0.4 (Hines, 1991) de-  
 483 pending on the theory and assumptions made. The first attempt to describe universal-  
 484 ity in measured wind spectra (e.g., Endlich et al., 1969; Dewan et al., 1984) was made  
 485 by Dewan and Good (1986) who assumed saturation via convective instabilities at each  
 486 vertical wave number independently and yielded  $C = 1$ . Later, this theory was extended  
 487 by S. A. Smith et al. (1987) to account also for amplitude limiting instabilities arising  
 488 from the whole wave spectrum instead, and value of  $C = 1/6$  was obtained. These tra-  
 489 ditional linear saturation theories were criticized in Hines (1991) and Chunchuzov (2002),  
 490 where it was shown that small-scale anisotropic inhomogeneities with  $k_z^{-3}$  vertical wavenum-  
 491 ber spectrum are shaped due to non-resonant internal wave-wave interactions. Chunchuzov  
 492 et al. (2015) compared vertical wavenumber spectra of effective sound-speed fluctuations  
 493 retrieved from infrasound detections of five volcanic eruptions and one explosion. Based  
 494 on this analysis, a value of  $C = 0.2$  for the upper stratosphere was proposed.

495 The power-laws corresponding to linear (Dewan & Good, 1986) and non-linear (Chunchuzov  
 496 et al., 2015) theoretical models are displayed in Fig. 8 together with error bars indicat-  
 497 ing possible variability in theoretical PSD amplitude ( $C = 0.1 - 0.4$ ). In both theo-  
 498 retical models, the altitude regime is controlled via the Brunt-Väisälä frequency,  $N$ . We  
 499 use  $N = 1.66 \cdot 10^{-2}$  rad/s in our calculations, which is typical for the lower mesosphere  
 500 (Dewan & Good, 1986). Theoretical models show a good agreement with the mean spec-  
 501 trum of the retrieved  $\Delta C_{\text{eff}}(z)$  profiles. This allows us to conclude that the infrasound-  
 502 based vertical wavenumber spectra that are obtained in this study are consistent with  
 503 previously obtained theoretical spectra, taking into account the confidence intervals of  
 504 those measurements (Fritts & Alexander, 2003).

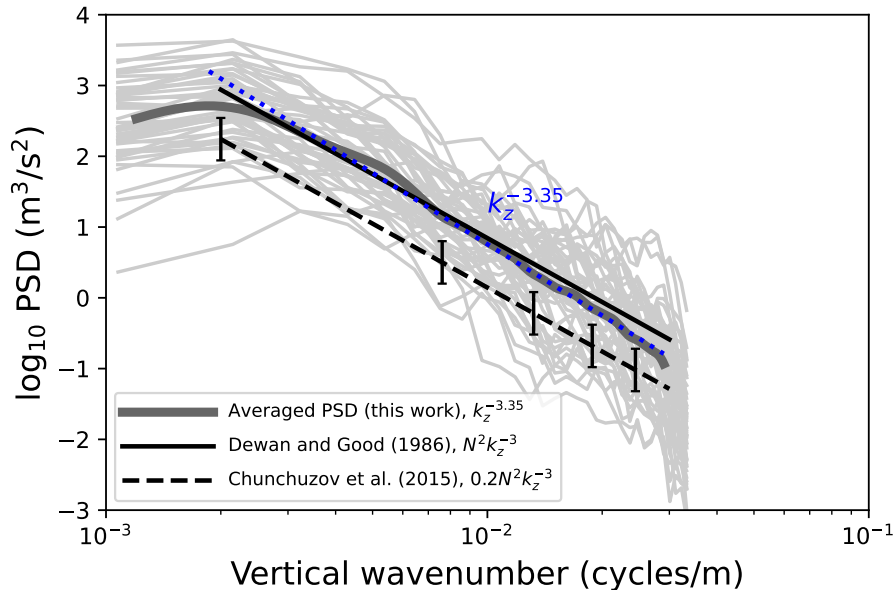


**Figure 8.** Vertical wavenumber power spectral density (PSD) of the retrieved  $\Delta C_{\text{eff}}(z)$  fluctuations (light gray lines) and their mean (dark gray line) versus theoretical models by Dewan and Good (1986) (black solid) and Chunchuzov et al. (2015) (black dashed). Black error bars indicate variability in theoretical PSD amplitude based on other theories mentioned in the text. The blue dotted line indicates the power-law fitting region for the mean PSD.

505 From the spectral analysis, we can estimate the outer and inner vertical scale of  
 506 atmospheric inhomogeneities that infrasound is sensitive to, based on the vertical wavenum-  
 507 ber limits within which the  $k_z^{-3}$  power-law establishes. Denoting the highest vertical wavenum-  
 508 ber as  $m_b$ , we obtain  $L_{\text{inner}} = 1/m_b = 33 - 37$  m and  $L_{\text{outer}} = 1/m_* = 386 - 585$  m.  
 509 Note that the limited altitude range of the  $\Delta C_{\text{eff}}(z)$  profiles retrieved restricts the sensi-  
 510 tivity to motions with smaller vertical wavenumbers (larger vertical scales). This could  
 511 be improved by processing longer segments of infrasound waveforms as was demonstrated  
 512 in e.g., Chunchuzov et al. (2013, 2015).

## 513 5 Discussion

514 The current study applies the effective sound-speed retrieval procedure by Chunchuzov  
 515 et al. (2015) to infrasound recordings in the shadow zone. This is the first time the afore-  
 516 mentioned approach is applied to a large and consistent dataset. Because we are retriev-  
 517 ing  $\Delta C_{\text{eff}}(z)$  profiles along a fixed source-receiver path and because the explosion yields  
 518 are similar for each event, we can consider the variability in the infrasound recordings  
 519 as being related to atmospheric dynamics.

520 The results show that vertical wavenumber PSDs obtained from the  $\Delta C_{\text{eff}}(z)$  pro-  
 521 files are close to the “universal” gravity wave saturation spectrum of  $k_z^{-3}$ . The very end  
 522 of the vertical wavenumber spectra in Fig. 8 corresponds to motions at scales of tens of  
 523 meters. This is on the edge of transition from the gravity wave saturation regime to the  
 524 turbulence regime where the theory predicts a transition from a  $k_z^{-3}$  power-law to  $k_z^{-5/3}$   
 525 (e.g., Gardner et al., 1993). The vertical wavenumber where this transition occurs may  
 526 have different values based on the latitude and altitude of interest, for example, the value

527 of  $2 \cdot 10^{-3}$  cycles/m was proposed in (Gardner et al., 1993) for mid-latitude mesopause  
 528 region. In contrast, Endlich et al. (1969) analyzed vertical wind profiles measured dur-  
 529 ing different seasons and found that their PSDs follow the  $k_z^{-3}$  power-law up to the ver-  
 530 tical wavenumber of  $10^{-2}$  cycles/m. However, the turbulence regime is outside of the scope  
 531 of this study, and we leave this question open for further research.

532 As  $C_{\text{eff}}(z)$  fluctuations are mostly associated with variations in horizontal wind (Sect. 3.4),  
 533 it would be interesting to compare the vertical wavenumber spectra obtained in this study  
 534 to spectra of wind measured near the IS37-Hukkakero region (Fig. 1). For this purpose,  
 535 the spectral characteristics of 11 infrasound-based  $\Delta C_{\text{eff}}(z)$  profile retrievals from 2017  
 536 were compared against independent wind measurements available from the Saura medium-  
 537 frequency (MF) radar near Andøya, Norway ( $69.14^\circ$  N,  $16.02^\circ$  E; Fig. 1). This radar is  
 538 located  $\sim 100$  km west of the IS37 infrasound station and  $\sim 420$  km north-west from  
 539 Hukkakero (Fig. 1), and operates on 3.17 MHz with 58 2kW pulsed transceiver modules.  
 540 Its observation capabilities include wind measurements, estimates of turbulent kinetic  
 541 energy dissipation rates, and electron density, as well as meteor observations. The ob-  
 542 servations typically provide measurements within the  $\sim 50$ – $100$  km altitude range with  
 543 a vertical resolution of 1–1.5 km (Singer et al., 2008). Hence, the system can observe  
 544 vertical variations at wavenumbers below approximately  $k_z = 10^{-3}$  cycles/m.

545 The wind data used for the validation has been derived from Doppler-Beam-Swinging  
 546 experiments measuring the radial velocity for one vertical and four oblique soundings in-  
 547 cluding statistical interferometric Angle of Arrival correction (see Renkwitz et al., 2018).

548 First, we directly compare the Saura radar winds to the SD-WACCM-X model winds.  
 549 As the effective sound speed  $\Delta C_{\text{eff}}(z)$  is taken along the horizontal infrasound propaga-  
 550 tion direction (Eq. 1), we project the Saura radar wind on the same unit vector point-  
 551 ing from Hukkakero towards IS37:  $\mathbf{u} \cdot \hat{n} = u \sin(\phi) + v \cos(\phi)$ , where  $\phi$  is the Hukkakero-  
 552 IS37 azimuth. The same projection was applied to the SD-WACCM-X wind profiles, ex-  
 553 tracted at the grid node located between the Saura radar and IS37 (Fig. 1). This com-  
 554 parison between Saura radar and SD-WACCM-X winds is displayed in Fig. 9a,b. Although  
 555 the radar measurements do not fully cover the altitude region where the infrasound-based  
 556  $\Delta C_{\text{eff}}(z)$  profiles are retrieved (highlighted in Fig. 9a,b), it can still be seen that the Saura  
 557 wind measurement features a pattern similar to the SD-WACCM-X model. There is a  
 558 weak wind pattern ( $< 50$  m/s) that alternates between positive and negative values, mostly  
 559 modulated by tidal waves. Above 70 km, a noticeable discrepancy between measured and  
 560 modeled winds is observed. This may be related to a lower temporal resolution of the  
 561 model compared to the radar, the distance between the sampling locations, or to inac-  
 562 curacies in the parametrization of gravity wave breaking used in the SD-WACCM-X model.  
 563 Moreover, note that above  $\sim 50$  km SD-WACCM-X is not supported by any observa-  
 564 tional dataset and is, therefore, expected to deviate more from the measurements. This  
 565 discrepancy between the radar measured winds and SD-WACCM was shown in (de Wit  
 566 et al., 2014), and is not unique to our measurements.

567 Next, we interpolate the SD-WACCM-X profiles to the radar vertical grid and per-  
 568 form a spectral comparison between the SD-WACCM-X and Saura radar wind profiles  
 569 closest in time to the explosion onset. The obtained vertical wavenumber spectra are dis-  
 570 played in Fig. 9c together with gravity wave saturation theories from Fig. 8. One can  
 571 see a good agreement in PSD amplitudes between the radar, atmospheric model and GW  
 572 saturation theories. However, it's clear that SD-WACCM-X wind spectra have steeper  
 573 slope and seem to underestimate amplitudes at ranges  $10^{-4}$ – $10^{-3}$  cycles/m. A more  
 574 detailed look into SD-WACCM-X and Saura radar horizontal winds over long time pe-  
 575 riods is needed to fully understand the nature of such discrepancy. We leave this ques-  
 576 tion open for further research suggesting that parametrization of subgrid-scale processes  
 577 in SD-WACCM-X can probably be improved.

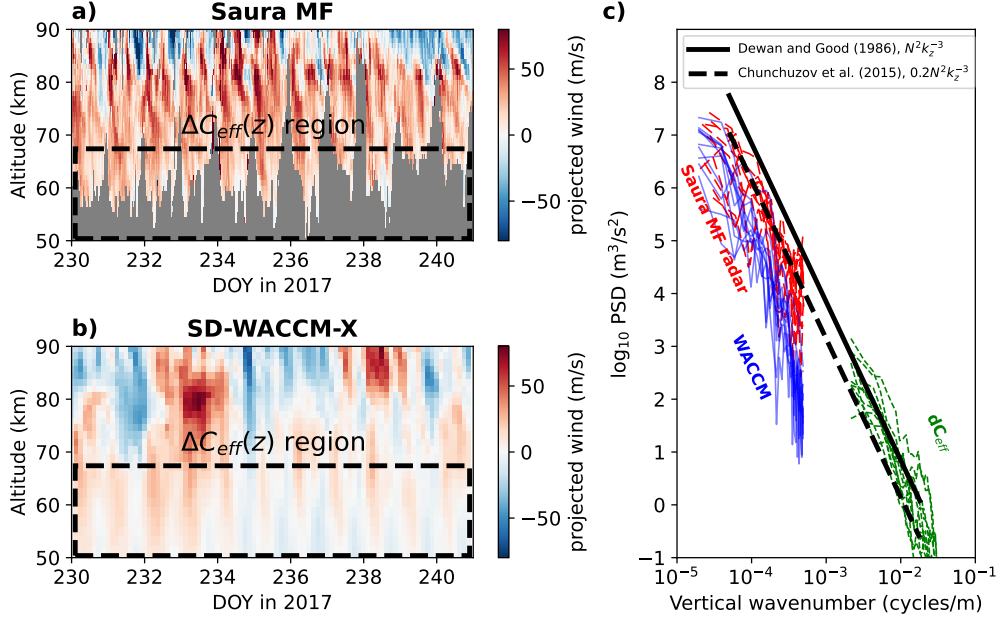


**Figure 9.** a) Projection of wind measured by Saura MF radar and b) predicted by SD-WACCM-X on the vector connecting Hukkakero and IS37. c) Vertical wavenumber spectra of the Saura radar winds (red dashed), SD-WACCM-X winds (blue solid) and retrieved  $\Delta C_{\text{eff}}(z)$  fluctuations (green dotted) for the explosions in 2017, versus theoretical models by Dewan and Good (1986) (black solid) and Chunchuzov et al. (2015) (black dashed).

578 To resolve the high-wavenumber part of the spectrum that the Saura radar and SD-  
 579 WACCM-X are insensitive to due to their vertical resolution, the infrasound-retrieved  
 580  $\Delta C_{\text{eff}}(z)$  profiles retrieved are used. The vertical wavenumber spectra for the 2017  $\Delta C_{\text{eff}}(z)$   
 581 profiles are presented in Fig. 9c. As was shown earlier (Fig. 8), the high-wavenumber part  
 582 of the spectrum follows the  $k_z^{-3}$  power-law and agrees well in amplitude with linear and  
 583 non-linear gravity wave saturation theories. The overall agreement found allows us to  
 584 suggest that Saura radar and infrasound-based  $\Delta C_{\text{eff}}(z)$  profiles represent low- and high-  
 585 wavenumber parts of the same “universal” GW spectrum.

586 Possible avenues for future research can include application of the same effective  
 587 sound-speed retrieval approach to later mesospheric and thermospheric arrivals observed  
 588 at IS37 (Fig. 3). This would provide an opportunity to study thicker atmospheric layers  
 589 and to possibly look at other physical phenomena that could be responsible for infrasound  
 590 scattering (e.g., polar mesospheric summer echoes). Another possible direction  
 591 of research could be comparing the effective sound-speed fluctuations obtained in this  
 592 study to other measurement techniques with high vertical resolution, e.g., lidar. More-  
 593 over, studying the 3D wind field and temperature fluctuations caused by gravity wave  
 594 could be performed by applying the retrieval approach to several infrasound stations around  
 595 the Hukkakero explosion site e.g., ARCES/ARCI (Karasjok, Norway), KRIS (Kiruna,  
 596 Norway) and APA/APAI (Apatity, Russia) (Gibbons et al., 2015).

## 597 6 Summary

598 In this study, infrasound waves from 49 blasts between 2014 and 2017 are used to  
 599 retrieve effective sound speed fluctuations,  $\Delta C_{\text{eff}}(z)$ , in the middle atmosphere. The ap-

600 plied retrieval recipe is based on approaches previously developed by Chunchuzov et al.  
601 (2013, 2015). It is based on a relation between the waveform of the scattered infrasound  
602 signal recorded on the surface in the shadow zone and the  $C_{\text{eff}}(z)$  fluctuation profile in  
603 an inhomogeneous atmospheric layer. The results obtained demonstrate that the infra-  
604 sound scattering occurs in the lower mesosphere between 50 and 75 km altitude. This  
605 atmospheric region is also known to be altitudes where gravity waves start to break (Garcia  
606 & Solomon, 1985). Therefore, information about the  $\Delta C_{\text{eff}}(z)$  retrieved from ground-based  
607 infrasound measurements is of direct interest for studying the GW activity and for po-  
608 tential improvement of GW parameterization schemes used in numerical weather pre-  
609 diction models. The spectral analysis of retrieved effective sound speed fluctuations in  
610 terms of vertical wavenumber spectra revealed that the tail of the mean spectrum fol-  
611 lows a  $k_z^{-3}$  power law. This law corresponds to the “universal” spectrum of horizontal  
612 wind fluctuations induced by gravity waves (Fritts & Alexander, 2003). The spectral char-  
613 acteristics of the 11 infrasound-based  $\Delta C_{\text{eff}}(z)$  profiles retrieved for 2017 were compared  
614 against independent wind measurements by the Saura MF radar. Good agreement in am-  
615 plitudes and slopes of the spectra was demonstrated, indicating that the infrasound and  
616 the radar measurements represent the high- and low-wavenumber sections of the “uni-  
617 versal” gravity-wave spectrum, respectively. Therefore, the current study opens the way  
618 for remote sensing of GW activity by means of ground-based infrasound measurements  
619 and to improve the representation of small-scale wind inhomogeneities in upper atmo-  
620 spheric model products. The latter would be beneficial for the infrasound scientific field  
621 since advanced simulations of infrasound propagation require atmospheric specifications  
622 with high vertical resolution (Hedlin & Drob, 2014; Chunchuzov et al., 2015; Lalande &  
623 Waxler, 2016; Sabatini et al., 2019). Moreover, the prospects of using explosive event se-  
624 quences as *datasets of opportunity* for middle atmospheric remote sensing can pave the  
625 way for an enhanced GW representation in atmospheric models.

626 **Appendix A Retrieved parameters and comparisons**

627 Table A1 provides details about the spectral analysis performed in Sect. 4.

**Table A1.** Explosion origin time, dominant wavenumber and the slope for the corresponding spectrum.

Origin time (yyyy-mm-dd HH:MM:SS, UTC)	DOY	$m_*$ [cycl/m]	exponent in $k_z^p$	RMSE relative to max amplitude
2014-08-22 11:59:59	234	2.15e-3	-3.79	0.06
2014-08-23 10:29:59	235	1.07e-3	-3.43	0.08
2014-08-24 11:59:59	236	2.15e-3	-3.29	0.13
2014-08-25 10:29:59	237	1.07e-3	-3.23	0.10
2014-08-26 10:59:59	238	2.15e-3	-3.04	0.07
2014-08-27 10:59:59	239	2.15e-3	-2.95	0.08
2014-08-28 10:59:59	240	2.15e-3	-3.30	0.08
2014-08-29 10:29:59	241	2.15e-3	-3.83	0.13
2014-08-30 10:29:59	242	2.15e-3	-3.95	0.10
2014-08-31 10:59:59	243	2.15e-3	-3.63	0.08
2014-09-01 09:59:59	244	2.15e-3	-3.67	0.13
2014-09-02 09:29:59	245	2.15e-3	-3.25	0.09
2015-08-13 10:59:59	225	2.15e-3	-3.71	0.08
2015-08-14 10:04:59	226	2.15e-3	-3.54	0.14
2015-08-15 10:59:59	227	2.15e-3	-3.87	0.09
2015-08-16 10:59:59	228	2.15e-3	-3.56	0.09
2015-08-17 11:59:59	229	2.15e-3	-3.02	0.13
2015-08-18 09:59:59	230	2.15e-3	-3.86	0.06
2015-08-19 09:29:59	231	2.15e-3	-2.90	0.08
2015-08-20 09:29:59	232	2.15e-3	-3.57	0.13
2015-08-21 09:29:59	233	2.15e-3	-3.19	0.08
2015-08-22 11:29:59	234	2.15e-3	-2.84	0.11
2015-08-23 11:29:59	235	2.15e-3	-2.65	0.09
2015-08-24 12:00:00	236	2.15e-3	-3.52	0.06
2016-08-18 12:29:59	231	2.15e-3	-3.18	0.10
2016-08-19 11:29:59	232	2.15e-3	-4.00	0.12
2016-08-20 13:29:59	233	2.15e-3	-3.76	0.07
2016-08-21 13:00:00	234	2.15e-3	-3.71	0.12
2016-08-22 11:59:59	235	2.15e-3	-3.60	0.09
2016-08-23 12:59:59	236	1.07e-3	-2.78	0.18
2016-08-24 11:59:59	237	2.15e-3	-3.06	0.12
2016-08-25 11:29:59	238	3.23e-3	-4.11	0.10
2016-08-26 11:29:59	239	2.15e-3	-3.36	0.10
2016-08-27 12:59:59	240	3.23e-3	-4.07	0.06
2016-08-28 10:59:59	241	2.15e-3	-3.13	0.13
2016-08-29 09:59:59	242	2.15e-3	-3.46	0.10
2016-08-30 07:54:59	243	3.22e-3	-3.13	0.07
2016-08-31 08:49:59	244	3.23e-3	-3.80	0.06
2017-08-18 11:59:59	230	2.15e-3	-4.25	0.18
2017-08-19 11:00:00	231	1.08e-3	-3.46	0.16
2017-08-20 12:00:00	232	2.15e-3	-3.70	0.08
2017-08-21 12:59:59	233	3.22e-3	-4.23	0.07
2017-08-22 11:59:59	234	2.15e-3	-3.47	0.10
2017-08-23 11:29:59	235	2.15e-3	-4.11	0.07
2017-08-24 11:29:59	236	2.15e-3	-4.06	0.14
2017-08-25 09:59:59	237	2.15e-3	-3.75	0.10
2017-08-26 10:59:59	238	2.15e-3	-3.59	0.07
2017-08-27 11:29:59	239	2.15e-3	-3.34	0.08
2017-08-28 10:29:59	240	2.15e-3	-3.40	0.11
<b>Mean:</b>		2.15e-3	-3.50	
<b>STD:</b>		4.40e-4	-0.39	

## Appendix B Derivation of the inversion equations

### B1 Derivation of Eq. 2

Consider a stationary atmosphere consisting of an inhomogeneous moving layer within  $z_0 \leq z \leq z_H$  and a homogeneous half-space below and above it. The sound speed  $c(z)$ , wind velocity  $\mathbf{v}(z)$  and density  $\rho(z)$  have continuous first and second order derivatives, and are constant outside the inhomogeneous layer with values of  $c_1$ ,  $\mathbf{v}_1$  and  $\rho_1$ . The layer is filled with stratified sound speed, wind velocity and density fluctuations  $\Delta c(z)$ ,  $\Delta \mathbf{v}(z)$  and  $\Delta \rho(z)$  on top of the background atmosphere. Therefore, sound speed, atmospheric wind and density within the inhomogeneous layer are defined as:  $c_{1+\Delta}(z) = c_1 + \Delta c(z)$ ,  $\mathbf{v}_{1+\Delta}(z) = \mathbf{v}_1 + \Delta \mathbf{v}(z)$ ,  $\rho_{1+\Delta}(z) = \rho_1 + \Delta \rho(z)$ . In terms of the relative fluctuations, it's assumed that  $\Delta c/c_1$ ,  $\Delta v/c_1$  and  $\Delta \rho/\rho_1$  are of the same order of smallness, namely  $M = |\Delta c/c_1| \ll 1$ .

A plane monochromatic acoustic wave  $A \exp(i(\xi_x x + \xi_y y + \mu z - \omega t))$  propagates from the source to the receiver upward through the homogeneous atmosphere and incident on a moving inhomogeneous layer at an angle  $\theta$  measured from the vertical. Here  $A$  is complex wave amplitude,  $\omega$  is wave frequency,  $\boldsymbol{\xi} = (\xi_x, \xi_y)$  is the horizontal propagation vector,  $\mu = (k_0^2 - |\boldsymbol{\xi}|^2)^{1/2}$  is the vertical wavenumber, and  $k_0 = \omega/c_1$  is the wavenumber in the homogeneous atmosphere. The projection of the wind velocity  $\mathbf{v}(z)$  on the source-receiver radius vector  $\boldsymbol{\xi}$  is defined as  $u(z) = \mathbf{v}(z)\boldsymbol{\xi}/|\boldsymbol{\xi}|$ .

We introduce the squared effective refractive index following Chunchuzov et al. (2013) as:

$$N^2(z) = \left( n^2 \beta^2 - \frac{\xi^2}{k_0^2} \right) \left( \frac{\rho_0}{\rho \beta^2} \right)^2, \quad (\text{B1})$$

where  $n = c_1/c$  is a refractive index in a stationary medium,  $\beta = 1 - \boldsymbol{\xi}\mathbf{v}(z)/\omega$ ,  $\rho_0$  is a density dimension coefficient,  $\xi = k_0 \sin \theta (1 + u_1 \sin \theta / c_1)^{-1}$ .

Small relative fluctuations of the effective refractive index in an inhomogeneous layer are defined as:

$$\varepsilon(z) = \ln \frac{N_{1+\Delta}^2}{N_1^2} = \ln \frac{n_{1+\Delta}^2 \beta_{1+\Delta}^2 - \xi^2/k_0^2}{n_1^2 \beta_1^2 - \xi^2/k_0^2} + 2 \ln \frac{\rho_1}{\rho_{1+\Delta}} + 4 \ln \frac{\beta_1}{\beta_{1+\Delta}}, \quad (\text{B2})$$

where

$$n_1 = 1, \quad n_{1+\Delta} = \frac{c_1}{c_1 + \Delta c}, \quad \text{and} \quad \beta_1 = 1 - \xi u_1 / \omega = \left( 1 + \frac{u_1 \sin \theta}{c_1} \right)^{-1}, \quad (\text{B3})$$

and

$$\beta_{1+\Delta} = 1 - \frac{\xi(u_1 + \Delta u(z))}{\omega} = \beta_1 \left( 1 - \frac{\Delta u(z) \sin \theta}{c_1} \right). \quad (\text{B4})$$

Substituting parameters from Eq. B3 into Eq. B2 and assuming the first-order of smallness for the natural logarithm,  $\ln(x/y) \sim (x - y)/y$ , yields

$$\varepsilon(z) = \frac{-2[\Delta c/c_1 + \Delta u(z) \sin \theta / c_1] + \mathcal{O}(M^2)}{\cos^2 \theta} + 4 \frac{\Delta u(z) \sin \theta}{c_1} - 2 \frac{\Delta \rho}{\rho_1}. \quad (\text{B5})$$

As  $\theta$  approaches  $\pi/2$  the last two terms can be neglected and Eq. 2 is obtained.

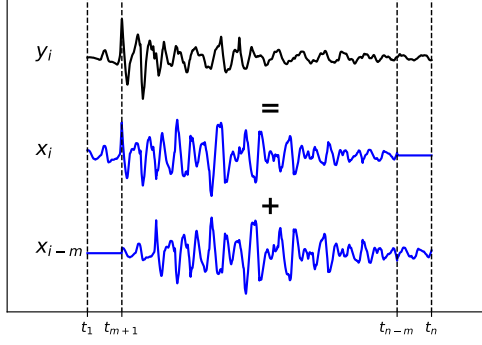


**Figure B1.** A synthetic example of the Eq. 4.

656

## B2 System of equations to solve Eq. 4

657

658

In this section, we provide the same explanation on how to numerically solve Eq. 4 as presented in (Chunchuzov & Kulichkov, 2020), but complemented with more detail.

659

660

661

662

663

664

665

Eq. 4 represents the dimensionless waveform of scattered signal as a sum of two effective refractive index profiles shifted in time by the time interval  $T_0$ . Let us denote values of the scattered signal at discrete times  $t_i$  as  $y_i = I_0(t_i)$  where  $i = 1, 2, \dots, n$  ( $n$  is the number of samples), and effective refractive index values as  $x_i = -\varepsilon(a[t_j - R_1/c_1])/4$  with non-zero values at  $1, 2, \dots, n - m$  and  $x_{i-m} = -\varepsilon(a[t_j - R_1/c_1 - T_0])/4$  with non-zero values at  $m + 1, m + 2, \dots, n$ , where  $m$  is the number of  $t_i$  values within the time interval  $T_0$ . Fig. B1 demonstrates Eq. 4 with the notation introduced.

Thus, the following system of linear algebraic equations with respect to  $x_i$  can be obtained from Eq. 4:

$$\begin{cases} y_i = x_i, & \text{for } 1 \leq i \leq m \\ y_i = x_i + x_{i-m}, & \text{for } m + 1 \leq i \leq n - m \\ y_i = x_{i-m}, & \text{for } n - m + 1 \leq i \leq n. \end{cases} \quad (\text{B6})$$

666

667

668

669

670

The number of unknowns in the system B6,  $n - m$ , is less than number of equations,  $n$ , and the system is therefore overdetermined. In this case, the least squares method can be used to find an approximate solution by minimizing the difference  $|\alpha X - Y|$  where  $X = x_j$ ,  $j = 1, 2, \dots, n - m$ ,  $Y = y_i$ ,  $i = 1, 2, \dots, n$ , and  $\alpha$  is the matrix of coefficients.

After the solution  $X = x_j$  has been found, the profile of the effective refractive index can be retrieved as  $\varepsilon(a[t_j - R_1/c_1]) = -4x_j$ . Next, the effective sound fluctuation profile is obtained from  $\varepsilon(z_j)$  values using Eq. 2 as:

$$\Delta C_{\text{eff}}(z_j) \approx \Delta c(z_j) + \Delta u(z_j) \sin \theta_0 = -\frac{\varepsilon(z_j)c_1 \cos^2 \theta_0}{2} = 2x_j c_1 \cos^2 \theta_0. \quad (\text{B7})$$

671

## Open Research Section

672

673

674

675

676

The 3-hourly SD-WACCM-X model product data are available via [https://www.earthsystemgrid.org/dataset/ucar.cgd.ccm4.SD-WACCM-X.v2.1.atm.hist.3hourly\\_inst.html](https://www.earthsystemgrid.org/dataset/ucar.cgd.ccm4.SD-WACCM-X.v2.1.atm.hist.3hourly_inst.html) (last access June 2022). The InfraGA infrasound propagation code (e.g., Blom & Waxler, 2017, 2021) is provided under open access by Los Alamos National Laboratory at <https://github.com/LANL-Seismoacoustics/infraGA> (last access June 2022).

677 The IS37 infrasound station is part of the International Monitoring System (IMS) of the  
 678 Preparatory Commission for the Comprehensive Nuclear-Test-Ban Treaty Organization  
 679 (CTBTO). Data access can be granted to third parties and researchers through the vir-  
 680 tual Data Exploitation Centre (vDEC) of the International Data Center: [https://www](https://www.ctbto.org/specials/vdec/)  
 681 [.ctbto.org/specials/vdec/](https://www.ctbto.org/specials/vdec/). The dataset of Saura wind measurements used in this  
 682 study is available via [https://www.radar-service.eu/radar/en/dataset/mzuBmhtrDxSGIBNd](https://www.radar-service.eu/radar/en/dataset/mzuBmhtrDxSGIBNd?token=leArd0pgjcsMPpeNSFy0)  
 683 [?token=leArd0pgjcsMPpeNSFy0](https://www.radar-service.eu/radar/en/dataset/mzuBmhtrDxSGIBNd?token=leArd0pgjcsMPpeNSFy0). More data can be obtained by contacting Toralf Renkwitz.

## 684 Acknowledgments

685 This research was supported by the Research Council of Norway FRIPRO/FRINATEK  
 686 basic research program, project contract 274377: *Middle Atmosphere Dynamics: Exploit-*  
 687 *ing Infrasound Using a Multidisciplinary Approach at High Latitudes* (MADEIRA). This  
 688 work was partially supported by the Research Council of Norway under contract 223252/F50  
 689 and RSF grant No. 21-17-00021. This study was facilitated by previous research performed  
 690 within the framework of the ARISE and ARISE2 projects (Blanc et al., 2018, 2019), funded  
 691 by the European Commission FP7 and Horizon 2020 programmes (Grant No. 284387 and  
 692 653980). The authors would also like to thank Yvan Orsolini for useful discussions and  
 693 suggestions.

## 694 References

- 695 Amezcua, J., Näsholm, S. P., Blixt, E. M., & Charlton-Perez, A. J. (2020). As-  
 696 simulation of atmospheric infrasound data to constrain tropospheric and  
 697 stratospheric winds. *Quarterly Journal of the Royal Meteorological Society*,  
 698 *146*(731), 2634–2653. doi: <https://doi.org/10.1002/qj.3809>
- 699 Assink, J., Le Pichon, A., Blanc, E., Kallel, M., & Khemiri, L. (2014). Evaluation  
 700 of wind and temperature profiles from ECMWF analysis on two hemispheres  
 701 using volcanic infrasound. *Journal of Geophysical Research: Atmospheres*,  
 702 *119*(14), 8659–8683. doi: <https://doi.org/10.1002/2014JD021632>
- 703 Assink, J., Smets, P., Marcillo, O., Weemstra, C., Lalande, J.-M., Waxler, R., &  
 704 Evers, L. (2019). Advances in infrasonic remote sensing methods. In *In-*  
 705 *frasound monitoring for atmospheric studies* (pp. 605–632). Springer. doi:  
 706 [https://doi.org/10.1007/978-3-319-75140-5\\_18](https://doi.org/10.1007/978-3-319-75140-5_18)
- 707 Assink, J., Waxler, R., & Drob, D. (2012). On the sensitivity of infrasonic trav-  
 708 eltimes in the equatorial region to the atmospheric tides. *Journal of Geo-*  
 709 *physical Research: Atmospheres*, *117*(D1). doi: [https://doi.org/10.1029/](https://doi.org/10.1029/2011JD016107)  
 710 [2011JD016107](https://doi.org/10.1029/2011JD016107)
- 711 Assink, J., Waxler, R., Frazier, W., & Lonzaga, J. (2013). The estimation of upper  
 712 atmospheric wind model updates from infrasound data. *Journal of Geophysical*  
 713 *Research: Atmospheres*, *118*(19), 10,707-10,724. doi: [https://doi.org/10.1002/](https://doi.org/10.1002/jgrd.50833)  
 714 [jgrd.50833](https://doi.org/10.1002/jgrd.50833)
- 715 Atmosphere, U. S. (1976). *Us standard atmosphere*. National Oceanic and Atmo-  
 716 spheric Administration.
- 717 Averbuch, G., Ronac-Giannone, M., Arrowsmith, S., & Anderson, J. (2022). Evi-  
 718 dence for short temporal atmospheric variations observed by infrasonic signals:  
 719 1. the troposphere. *Earth and Space Science*, *9*(3), e2021EA002036. doi:  
 720 <https://doi.org/10.1029/2021EA002036>
- 721 Bauer, P., Thorpe, A., & Brunet, G. (2015). The quiet revolution of numerical  
 722 weather prediction. *Nature*, *525*(7567), 47–55. doi: [https://doi.org/10.1038/](https://doi.org/10.1038/nature14956)  
 723 [nature14956](https://doi.org/10.1038/nature14956)
- 724 Becker, E., Vadas, S. L., Bossert, K., Harvey, V. L., Zülicke, C., & Hoffmann, L.  
 725 (2022). A high-resolution whole-atmosphere model with resolved gravity  
 726 waves and specified large-scale dynamics in the troposphere and stratosphere.  
 727 *Journal of Geophysical Research: Atmospheres*, *127*(2), e2021JD035018. doi:

- 10.1029/2021JD035018
- 728  
729 Bengtsson, L., Andrae, U., Aspelien, T., Batrak, Y., Calvo, J., de Rooy, W., ... oth-  
730 ers (2017). The HARMONIE-AROME model configuration in the ALADIN-  
731 HIRLAM NWP system. *Monthly Weather Review*, *145*(5), 1919–1935. doi:  
732 <https://doi.org/10.1175/MWR-D-16-0417.1>
- 733 Bertin, M., Millet, C., & Bouche, D. (2014). A low-order reduced model for the  
734 long range propagation of infrasounds in the atmosphere. *The Journal of the*  
735 *Acoustical Society of America*, *136*(1), 37–52. doi: [https://doi.org/10.1121/1](https://doi.org/10.1121/1.4883388)  
736 [.4883388](https://doi.org/10.1121/1.4883388)
- 737 Blanc, E., Ceranna, L., Hauchecorne, A., Charlton-Perez, A., Marchetti, E., Evers,  
738 L., ... Chum, J. (2018). Toward an improved representation of middle atmo-  
739 spheric dynamics thanks to the ARISE project. *Surveys in Geophysics*, *39*(2),  
740 171–225. doi: 10.1007/s10712-017-9444-0
- 741 Blanc, E., Pol, K., Le Pichon, A., Hauchecorne, A., Keckhut, P., Baumgarten,  
742 G., ... Smets, P. (2019). Middle atmosphere variability and model uncer-  
743 tainties as investigated in the framework of the ARISE project. In *Infra-*  
744 *sound monitoring for atmospheric studies* (pp. 845–887). Springer. doi:  
745 [https://doi.org/10.1007/978-3-319-75140-5\\_28](https://doi.org/10.1007/978-3-319-75140-5_28)
- 746 Blixt, E. M., Näsholm, S. P., Gibbons, S. J., Evers, L. G., Charlton-Perez, A. J., Or-  
747 solini, Y. J., & Kværna, T. (2019). Estimating tropospheric and stratospheric  
748 winds using infrasound from explosions. *The Journal of the Acoustical Society*  
749 *of America*, *146*(2), 973–982. doi: <https://doi.org/10.1121/1.5120183>
- 750 Blom, P., & Waxler, R. (2017). Modeling and observations of an elevated, moving  
751 infrasonic source: Eigenray methods. *The Journal of the Acoustical Society of*  
752 *America*, *141*(4), 2681–2692. doi: <https://doi.org/10.1121/1.4980096>
- 753 Blom, P., & Waxler, R. (2021). Characteristics of thermospheric infrasound pre-  
754 dicted using ray tracing and weakly non-linear waveform analyses. *The Journal*  
755 *of the Acoustical Society of America*, *149*(5), 3174–3188. doi: [https://doi.org/](https://doi.org/10.1121/10.0004949)  
756 [10.1121/10.0004949](https://doi.org/10.1121/10.0004949)
- 757 Bossert, K., Fritts, D. C., Pautet, P.-D., Williams, B. P., Taylor, M. J., Kaifler, B.,  
758 ... MacKinnon, A. D. (2015). Momentum flux estimates accompanying mul-  
759 tiscala gravity waves over Mount Cook, New Zealand, on 13 July 2014 during  
760 the DEEPWAVE campaign. *Journal of Geophysical Research: Atmospheres*,  
761 *120*(18), 9323–9337. doi: <https://doi.org/10.1002/2015JD023197>
- 762 Brekhovskikh, L. (1960). Propagation of acoustic and infrared waves in natural  
763 waveguides over long distances. *Soviet Physics Uspekhi*, *3*(1), 159. doi: 10  
764 [.1070/PU1960v003n01ABEH003263](https://doi.org/10.1070/PU1960v003n01ABEH003263)
- 765 Brissaud, Q., Näsholm, S. P., Turquet, A., & Le Pichon, A. (2023, January). Pre-  
766 dicting infrasound transmission loss using deep learning. *Geophysical Journal*  
767 *International*, *232*(1), 274–286. doi: 10.1093/gji/ggac307
- 768 Chunchuzov, I. (2002). On the high-wavenumber form of the eulerian internal  
769 wave spectrum in the atmosphere. *Journal of the atmospheric sciences*,  
770 *59*(10), 1753–1774. doi: [https://doi.org/10.1175/1520-0469\(2002\)059<1753:](https://doi.org/10.1175/1520-0469(2002)059<1753:OTHWFO>2.0.CO;2)  
771 [OTHWFO>2.0.CO;2](https://doi.org/10.1175/1520-0469(2002)059<1753:OTHWFO>2.0.CO;2)
- 772 Chunchuzov, I., & Kulichkov, S. (2020). *Infrasound propagation in an anisotropic*  
773 *fluctuating atmosphere*. Cambridge Scholars Publishing.
- 774 Chunchuzov, I., Kulichkov, S., & Firstov, P. (2013). On acoustic N-wave reflections  
775 from atmospheric layered inhomogeneities. *Izvestiya, Atmospheric and Oceanic*  
776 *Physics*, *49*(3), 258–270. doi: <https://doi.org/10.1134/S0001433813020060>
- 777 Chunchuzov, I., Kulichkov, S., Perepelkin, V., Popov, O., Firstov, P., Assink, J.,  
778 & Marchetti, E. (2015). Study of the wind velocity-layered structure in the  
779 stratosphere, mesosphere, and lower thermosphere by using infrasound probing  
780 of the atmosphere. *Journal of Geophysical Research: Atmospheres*, *120*(17),  
781 8828–8840. doi: <https://doi.org/10.1002/2015JD023276>
- 782 Chunchuzov, I., Kulichkov, S., Popov, O., & Perepelkin, V. (2022). Infrasound

- 783 propagation through the atmosphere with mesoscale wind velocity and tem-  
 784 perature fluctuations. *Waves in Random and Complex Media*, 1–16. doi:  
 785 10.1080/17455030.2022.2056259
- 786 Chunchuzov, I., Kulichkov, S., Popov, O., Waxler, R., & Assink, J. (2011). Scatter-  
 787 ing of infrasound by anisotropic inhomogeneities of the atmosphere. *Izv. At-*  
 788 *mos. Oceanic Phys*, 47(5), 540–547.
- 789 Cugnet, D., de la Camara, A., Lott, F., Millet, C., & Ribstein, B. (2019). Non-  
 790 orographic gravity waves: Representation in climate models and effects on  
 791 infrasound. In A. Le Pichon, E. Blanc, & A. Hauchecorne (Eds.), *Infrasound*  
 792 *monitoring for atmospheric studies: Challenges in middle atmosphere dynam-*  
 793 *ics and societal benefits* (pp. 827–844). Cham, Switzerland: Springer. doi:  
 794 10.1007/978-3-319-75140-5\_27
- 795 De Carlo, M., Arduin, F., & Le Pichon, A. (2020, January). Atmospheric infra-  
 796 sound generation by ocean waves in finite depth: unified theory and applica-  
 797 tion to radiation patterns. *Geophysical Journal International*, 221(1), 569–585.  
 798 doi: 10.1093/gji/ggaa015
- 799 Dewan, E., & Good, R. (1986). Saturation and the “universal” spectrum for verti-  
 800 cal profiles of horizontal scalar winds in the atmosphere. *Journal of Geophysi-*  
 801 *cal Research: Atmospheres*, 91(D2), 2742–2748. doi: [https://doi.org/10.1029/  
 802 JD091iD02p02742](https://doi.org/10.1029/JD091iD02p02742)
- 803 Dewan, E., Grossbard, N., Quesada, A., & Good, R. (1984). Spectral analysis of  
 804 10m resolution scalar velocity profiles in the stratosphere. *Geophysical research*  
 805 *letters*, 11(1), 80–83. doi: <https://doi.org/10.1029/GL011i001p00080>
- 806 de Wit, R. J., Hibbins, R. E., Espy, P. J., Orsolini, Y. J., Limpasuvan, V., & Kin-  
 807 nison, D. E. (2014). Observations of gravity wave forcing of the mesopause  
 808 region during the January 2013 major sudden stratospheric warming. *Geo-*  
 809 *physical Research Letters*, 41(13), 4745–4752. doi: [https://doi.org/10.1002/  
 810 2014GL060501](https://doi.org/10.1002/2014GL060501)
- 811 Diamond, M. (1963). Sound channels in the atmosphere. *Journal of Geophysical Re-*  
 812 *search*, 68(11), 3459–3464. doi: <https://doi.org/10.1029/JZ068i011p03459>
- 813 Drob, D. (2019). Meteorology, climatology, and upper atmospheric composition for  
 814 infrasound propagation modeling. In *Infrasound monitoring for atmospheric*  
 815 *studies* (pp. 485–508). Springer. doi: [https://doi.org/10.1007/978-3-319-75140-  
 816 -5\\_14](https://doi.org/10.1007/978-3-319-75140-5_14)
- 817 Drob, D., Broutman, D., Hedlin, M., Winslow, N., & Gibson, R. (2013). A method  
 818 for specifying atmospheric gravity wavefields for long-range infrasound propa-  
 819 gation calculations. *Journal of Geophysical Research: Atmospheres*, 118(10),  
 820 3933–3943. doi: <https://doi.org/10.1029/2012JD018077>
- 821 Endlich, R. M., Singleton, R. C., & Kaufman, J. W. (1969). Spectral analysis of  
 822 detailed vertical wind speed profiles. *Journal of Atmospheric Sciences*, 26(5),  
 823 1030–1041. doi: [https://doi.org/10.1175/1520-0469\(1969\)026<1030:SAODVW>  
 824 .0.CO;2](https://doi.org/10.1175/1520-0469(1969)026<1030:SAODVW>2.0.CO;2)
- 825 Evers, L. G. (2008). *The inaudible symphony: On the detection and source identi-*  
 826 *fication of atmospheric infrasound* (PhD Thesis). Delft University of Technol-  
 827 ogy, The Netherlands.
- 828 Fee, D., Waxler, R., Assink, J., Gitterman, Y., Given, J., Coyne, J., ... others  
 829 (2013). Overview of the 2009 and 2011 Sayarim infrasound calibration exper-  
 830 iments. *Journal of Geophysical Research: Atmospheres*, 118(12), 6122–6143.  
 831 doi: <https://doi.org/10.1002/jgrd.50398>
- 832 Fritts, D. C., & Alexander, M. J. (2003). Gravity wave dynamics and effects in the  
 833 middle atmosphere. *Reviews of geophysics*, 41(1). doi: [https://doi.org/10.  
 834 .1029/2001RG000106](https://doi.org/10.1029/2001RG000106)
- 835 Garcia, R. R., & Boville, B. A. (1994). “Downward control” of the mean  
 836 meridional circulation and temperature distribution of the polar winter  
 837 stratosphere. *Journal of Atmospheric Sciences*, 51(15), 2238–2245. doi:

- 838 [https://doi.org/10.1175/1520-0469\(1994\)051\(2238:COTMMC\)2.0.CO;2](https://doi.org/10.1175/1520-0469(1994)051(2238:COTMMC)2.0.CO;2)
- 839 Garcia, R. R., & Solomon, S. (1985). The effect of breaking gravity waves on the  
840 dynamics and chemical composition of the mesosphere and lower thermo-  
841 sphere. *Journal of Geophysical Research: Atmospheres*, *90*(D2), 3850–3868.  
842 doi: <https://doi.org/10.1029/JD090iD02p03850>
- 843 Gardner, C. S., Hostetler, C. A., & Franke, S. J. (1993). Gravity wave models for  
844 the horizontal wave number spectra of atmospheric velocity and density fluc-  
845 tuations. *Journal of Geophysical Research: Atmospheres*, *98*(D1), 1035–1049.  
846 doi: <https://doi.org/10.1029/92JD02051>
- 847 Gelaro, R., McCarty, W., Suárez, M. J., Todling, R., Molod, A., Takacs, L., ...  
848 Zhao, B. (2017). The modern-era retrospective analysis for research and ap-  
849 plications, version 2 (MERRA-2). *Journal of climate*, *30*(14), 5419–5454. doi:  
850 <https://doi.org/10.1175/JCLI-D-16-0758.1>
- 851 Gibbons, S., Asming, V., Eliasson, L., Fedorov, A., Fyen, J., Kero, J., ... Vино-  
852 gradov, Y. (2015). The European Arctic: A laboratory for seismoacoustic stud-  
853 ies. *Seismological Research Letters*, *86*(3), 917–928. doi: 10.1785/0220140230
- 854 Gibbons, S., Kværna, T., & Näsholm, S. P. (2019). Characterization of the infra-  
855 sonic wavefield from repeating seismo-acoustic events. In *Infrasound monitor-*  
856 *ing for atmospheric studies* (pp. 387–407). Springer. doi: [https://doi.org/10.1007/978-3-319-75140-5\\_10](https://doi.org/10.1007/978-3-319-75140-5_10)
- 857  
858 Gibbons, S. J., Kværna, T., Tiira, T., & Kozlovskaya, E. (2020). A benchmark case  
859 study for seismic event relative location. *Geophysical Journal International*.  
860 doi: 10.1093/gji/ggaa362
- 861 Green, D. N., Waxler, R., Lalande, J.-M., Velea, D., & Talmadge, C. (2018).  
862 Regional infrasound generated by the Humming Roadrunner ground truth  
863 experiment. *Geophysical Journal International*, *214*(3), 1847–1864. doi:  
864 <https://doi.org/10.1093/gji/ggy232>
- 865 Hamilton, M., & Blackstock, D. (2008). *Nonlinear acoustics*. Acoustical Society of  
866 America.
- 867 Hedlin, M. A., & Drob, D. P. (2014). Statistical characterization of atmospheric  
868 gravity waves by seismoacoustic observations. *Journal of Geophysical Research:*  
869 *Atmospheres*, *119*(9), 5345–5363. doi: <https://doi.org/10.1002/2013JD021304>
- 870 Hines, C. O. (1991). The saturation of gravity waves in the middle atmosphere. Part  
871 II: Development of doppler-spread theory. *Journal of Atmospheric Sciences*,  
872 *48*(11), 1361–1379. doi: [https://doi.org/10.1175/1520-0469\(1991\)048\(1361:  
873 TSOGWI\)2.0.CO;2](https://doi.org/10.1175/1520-0469(1991)048(1361:TSOGWI)2.0.CO;2)
- 874 Kinney, G., & Graham, K. (1985). Explosive shocks in air, 2 nd. *New York:*  
875 *Springer Science*, *10*, 978–3.
- 876 Kulichkov, S. (2010). On the prospects for acoustic sounding of the fine structure of  
877 the middle atmosphere. In *Infrasound monitoring for atmospheric studies* (pp.  
878 511–540). Springer. doi: [https://doi.org/10.1007/978-1-4020-9508-5\\_16](https://doi.org/10.1007/978-1-4020-9508-5_16)
- 879 Kulichkov, S., Popov, O., Mishenin, A., Chunchuzov, I., Chkhetiani, O., & Tsybul-  
880 skaya, N. (2017). Using the acoustic-pulse conservation law in estimating  
881 the energy of surface acoustic sources by remote sounding. *Izvestiya, Atmo-*  
882 *spheric and Oceanic Physics*, *53*(6), 603–612. doi: [https://doi.org/10.1134/  
883 S0001433817060068](https://doi.org/10.1134/S0001433817060068)
- 884 Kumari, K., Wu, H., Long, A., Lu, X., & Oberheide, J. (2021). Mechanism  
885 studies of Madden-Julian oscillation coupling into the mesosphere/lower  
886 thermosphere tides using SABER, MERRA-2, and SD-WACCMX. *Jour-*  
887 *nal of Geophysical Research: Atmospheres*, *126*(13), e2021JD034595. doi:  
888 <https://doi.org/10.1029/2021JD034595>
- 889 Lalande, J.-M., & Waxler, R. (2016). The interaction between infrasonic waves  
890 and gravity wave perturbations: Application to observations using uttr rocket  
891 motor fuel elimination events. *Journal of Geophysical Research: Atmospheres*,  
892 *121*(10), 5585–5600. doi: <https://doi.org/10.1002/2015JD024527>

- 893 Le Pichon, A., Assink, J. D., Heinrich, P., Blanc, E., Charlton-Perez, A., Lee, C. F.,  
 894 ... Claud, C. (2015). Comparison of co-located independent ground-based  
 895 middle atmospheric wind and temperature measurements with numerical  
 896 weather prediction models. *Journal of Geophysical Research: Atmospheres*,  
 897 *120*(16), 8318–8331. doi: <https://doi.org/10.1002/2015JD023273>
- 898 Le Pichon, A., Blanc, E., & Drob, D. (2005). Probing high-altitude winds using  
 899 infrasound. *Journal of Geophysical Research: Atmospheres*, *110*(D20). doi:  
 900 <https://doi.org/10.1029/2005JD006020>
- 901 Le Pichon, A., Garcés, M., Blanc, E., Barthélémy, M., & Drob, D. P. (2002). Acous-  
 902 tic propagation and atmosphere characteristics derived from infrasonic waves  
 903 generated by the Concorde. *The Journal of the Acoustical Society of America*,  
 904 *111*(1), 629–641. doi: <https://doi.org/10.1121/1.1404434>
- 905 Liu, H.-L., Bardeen, C. G., Foster, B. T., Lauritzen, P., Liu, J., Lu, G., ... others  
 906 (2018). Development and validation of the Whole Atmosphere Community  
 907 Climate Model with thermosphere and ionosphere extension (WACCM-X  
 908 2.0). *Journal of Advances in Modeling Earth Systems*, *10*(2), 381–402. doi:  
 909 <https://doi.org/10.1002/2017MS001232>
- 910 Liu, H.-L., McInerney, J., Santos, S., Lauritzen, P., Taylor, M., & Pedatella, N.  
 911 (2014). Gravity waves simulated by high-resolution whole atmosphere com-  
 912 munity climate model. *Geophysical Research Letters*, *41*(24), 9106–9112. doi:  
 913 <https://doi.org/10.1002/2014GL062468>
- 914 Liu, J., Liu, H., Wang, W., Burns, A. G., Wu, Q., Gan, Q., ... Schreiner, W. S.  
 915 (2018). First results from the ionospheric extension of WACCM-X during the  
 916 deep solar minimum year of 2008. *Journal of Geophysical Research: Space*  
 917 *Physics*, *123*(2), 1534–1553. doi: <https://doi.org/10.1002/2017JA025010>
- 918 Lonzaga, J. B. (2015). A theoretical relation between the celerity and trace velocity  
 919 of infrasonic phases. *The Journal of the Acoustical Society of America*, *138*(3),  
 920 EL242–EL247. doi: <https://doi.org/10.1121/1.4929628>
- 921 Lonzaga, J. B., Waxler, R. M., Assink, J. D., & Talmadge, C. L. (2015). Modelling  
 922 waveforms of infrasound arrivals from impulsive sources using weakly non-  
 923 linear ray theory. *Geophysical Journal International*, *200*(3), 1347–1361. doi:  
 924 <https://doi.org/10.1093/gji/ggu479>
- 925 Marty, J. (2019). The IMS infrasound network: current status and technological  
 926 developments. In *Infrasound monitoring for atmospheric studies* (pp. 3–62).  
 927 Springer. doi: [https://doi.org/10.1007/978-3-319-75140-5\\_1](https://doi.org/10.1007/978-3-319-75140-5_1)
- 928 McFarlane, N. (1987). The effect of orographically excited gravity wave drag on  
 929 the general circulation of the lower stratosphere and troposphere. *Journal of*  
 930 *Atmospheric Sciences*, *44*(14), 1775–1800. doi: [https://doi.org/10.1175/1520-0469\(1987\)044\(1775:TEOOEG\)2.0.CO;2](https://doi.org/10.1175/1520-0469(1987)044(1775:TEOOEG)2.0.CO;2)
- 931  
 932 Melton, B. S., & Bailey, L. F. (1957). Multiple signal correlators. *Geophysics*, *22*(3),  
 933 565–588. doi: <https://doi.org/10.1190/1.1438390>
- 934 Miller, A., Fritts, D., Chapman, D., Jones, G., Limon, M., Araujo, D., ... others  
 935 (2015). Stratospheric imaging of polar mesospheric clouds: A new window  
 936 on small-scale atmospheric dynamics. *Geophysical Research Letters*, *42*(14),  
 937 6058–6065. doi: <https://doi.org/10.1002/2015GL064758>
- 938 Nippress, A., Green, D. N., Marcillo, O. E., & Arrowsmith, S. J. (2014). Generating  
 939 regional infrasound celerity-range models using ground-truth information and  
 940 the implications for event location. *Geophysical Journal International*, *197*(2),  
 941 1154–1165. doi: <https://doi.org/10.1093/gji/ggu049>
- 942 Orsolini, Y. J., Limpasuvan, V., Pérot, K., Espy, P., Hibbins, R., Lossow, S.,  
 943 ... Murtagh, D. (2017). Modelling the descent of nitric oxide during  
 944 the elevated stratopause event of January 2013. *Journal of Atmospheric*  
 945 *and Solar-Terrestrial Physics*, *155*, 50–61. doi: [https://doi.org/10.1016/](https://doi.org/10.1016/j.jastp.2017.01.006)  
 946 [j.jastp.2017.01.006](https://doi.org/10.1016/j.jastp.2017.01.006)
- 947 Pancheva, D., Mukhtarov, P., Hall, C., Meek, C., Tsutsumi, M., Pedatella, N., &

- 948 Nozawa, S. (2020). Climatology of the main (24-h and 12-h) tides observed by  
 949 meteor radars at svalbard and tromsø: Comparison with the models CMAM-  
 950 DAS and WACCM-X. *Journal of Atmospheric and Solar-Terrestrial Physics*,  
 951 *207*, 105339. doi: <https://doi.org/10.1016/j.jastp.2020.105339>
- 952 Pilger, C., Ceranna, L., Ross, J. O., Vergoz, J., Le Pichon, A., Brachet, N., ...  
 953 Mialle, P. (2018). The European Infrasound Bulletin. *Pure and Applied*  
 954 *Geophysics*, *175*(10), 3619–3638. doi: [10.1007/s00024-018-1900-3](https://doi.org/10.1007/s00024-018-1900-3)
- 955 Podglajen, A., Le Pichon, A., Garcia, R. F., G erier, S., Millet, C., Bedka, K., ...  
 956 Hertzog, A. (2022). Stratospheric balloon observations of infrasound waves  
 957 from the January 15 2022 Hunga eruption, Tonga. *Geophysical Research Let-*  
 958 *ters*, e2022GL100833. doi: [10.1029/2022GL100833](https://doi.org/10.1029/2022GL100833)
- 959 Rapp, M., & L ubken, F.-J. (2004). Polar mesosphere summer echoes (PMSE): Re-  
 960 view of observations and current understanding. *Atmospheric chemistry and*  
 961 *physics*, *4*(11/12), 2601–2633. doi: <https://doi.org/10.5194/acp-4-2601-2004>
- 962 Renkowitz, T., Tsutsumi, M., Laskar, F. I., Chau, J. L., & Latteck, R. (2018). On the  
 963 role of anisotropic MF/HF scattering in mesospheric wind estimation. *Earth,*  
 964 *Planets and Space*, *70*(1), 1–16. doi: [https://doi.org/10.1186/s40623-018-0927-  
 965 \*0\*](https://doi.org/10.1186/s40623-018-0927-0)
- 966 Sabatini, R., Snively, J. B., Baily, C., Hickey, M. P., & Garrison, J. L. (2019). Nu-  
 967 merical modeling of the propagation of infrasonic acoustic waves through the  
 968 turbulent field generated by the breaking of mountain gravity waves. *Geo-*  
 969 *physical Research Letters*, *46*(10), 5526–5534. doi: [https://doi.org/10.1029/](https://doi.org/10.1029/2019GL082456)  
 970 [2019GL082456](https://doi.org/10.1029/2019GL082456)
- 971 Sassi, F., Liu, H.-L., Ma, J., & Garcia, R. R. (2013). The lower thermosphere during  
 972 the northern hemisphere winter of 2009: A modeling study using high-altitude  
 973 data assimilation products in WACCM-X. *Journal of Geophysical Research:*  
 974 *Atmospheres*, *118*(16), 8954–8968. doi: <https://doi.org/10.1002/jgrd.50632>
- 975 Sch afer, B., Baumgarten, G., & Fiedler, J. (2020). Small-scale structures in noc-  
 976 tilucent clouds observed by lidar. *Journal of Atmospheric and Solar-Terrestrial*  
 977 *Physics*, *208*, 105384. doi: <https://doi.org/10.1016/j.jastp.2020.105384>
- 978 Selvaraj, D., Patra, A., Chandra, H., Sinha, H., & Das, U. (2014). Scattering cross  
 979 section of mesospheric echoes and turbulence parameters from gadanki radar  
 980 observations. *Journal of Atmospheric and Solar-Terrestrial Physics*, *119*,  
 981 162–172. doi: <https://doi.org/10.1016/j.jastp.2014.08.004>
- 982 Shaw, T. A., & Shepherd, T. G. (2008). Raising the roof. *Nature geoscience*, *1*(1),  
 983 12–13. doi: <https://doi.org/10.1038/ngeo.2007.53>
- 984 Singer, W., Latteck, R., & Holdsworth, D. (2008). A new narrow beam doppler  
 985 radar at 3 MHz for studies of the high-latitude middle atmosphere. *Advances*  
 986 *in Space Research*, *41*(9), 1488–1494. doi: [https://doi.org/10.1016/j.asr.2007.  
 987 \*.10.006\*](https://doi.org/10.1016/j.asr.2007.10.006)
- 988 Siskind, D. E., Harvey, V. L., Sassi, F., McCormack, J. P., Randall, C. E., Hervig,  
 989 M. E., & Bailey, S. M. (2021). Two- and three-dimensional structures of the  
 990 descent of mesospheric trace constituents after the 2013 sudden stratospheric  
 991 warming elevated stratopause event. *Atmospheric Chemistry and Physics*,  
 992 *21*(18), 14059–14077. doi: [10.5194/acp-21-14059-2021](https://doi.org/10.5194/acp-21-14059-2021)
- 993 Smets, P. S. M., & Evers, L. G. (2014). The life cycle of a sudden stratospheric  
 994 warming from infrasonic ambient noise observations. *Journal of Geophys-*  
 995 *ical Research: Atmospheres*, *119*(21), 12–084. doi: [https://doi.org/10.1002/](https://doi.org/10.1002/2014JD021905)  
 996 [2014JD021905](https://doi.org/10.1002/2014JD021905)
- 997 Smith, A. K. (2012). Global dynamics of the MLT. *Surveys in Geophysics*, *33*(6),  
 998 1177–1230. doi: <https://doi.org/10.1007/s10712-012-9196-9>
- 999 Smith, S. A., Fritts, D. C., & Vanzandt, T. E. (1987). Evidence for a saturated spec-  
 1000 trum of atmospheric gravity waves. *Journal of Atmospheric Sciences*, *44*(10),  
 1001 1404–1410. doi: [https://doi.org/10.1175/1520-0469\(1987\)044<1404:EFASSO>2.0](https://doi.org/10.1175/1520-0469(1987)044<1404:EFASSO>2.0.CO;2)  
 1002 [.CO;2](https://doi.org/10.1175/1520-0469(1987)044<1404:EFASSO>2.0.CO;2)

- 1003 Stocker, T. F., Qin, D., Plattner, G.-K., Tignor, M. M., Allen, S. K., Boschung, J.,  
 1004 ... Midgley, P. M. (2014). Climate Change 2013: The physical science basis.  
 1005 working group I contribution to the fifth assessment report of IPCC the inter-  
 1006 governmental panel on climate change. In (p. 741–866). Cambridge University  
 1007 Press. doi: 10.1017/CBO9781107415324.020
- 1008 Strelnikov, B., Eberhart, M., Friedrich, M., Hedin, J., Khaplanov, M., Baumgarten,  
 1009 G., ... Pautet, P.-D. (2019). Simultaneous in situ measurements of small-  
 1010 scale structures in neutral, plasma, and atomic oxygen densities during the  
 1011 WADIS sounding rocket project. *Atmospheric Chemistry and Physics*, 19(17),  
 1012 11443–11460. doi: 10.5194/acp-19-11443-2019
- 1013 Tsuda, T. (2014). Characteristics of atmospheric gravity waves observed using the  
 1014 MU (Middle and Upper atmosphere) radar and GPS (Global Positioning Sys-  
 1015 tem) radio occultation. *Proceedings of the Japan Academy, Series B*, 90(1),  
 1016 12–27. doi: <https://doi.org/10.2183/pjab.90.12>
- 1017 van Caspel, W. E., Espy, P. J., Ortland, D. A., & Hibbins, R. E. (2022). The mid-  
 1018 to high-latitude migrating semidiurnal tide: Results from a mechanistic tide  
 1019 model and superdarn observations. *Journal of Geophysical Research: Atmo-*  
 1020 *spheres*, 127(1), e2021JD036007. doi: <https://doi.org/10.1029/2021JD036007>
- 1021 Vera Rodriguez, I., Näsholm, S. P., & Le Pichon, A. (2020). Atmospheric wind and  
 1022 temperature profiles inversion using infrasound: An ensemble model context.  
 1023 *The Journal of the Acoustical Society of America*, 148(5), 2923–2934. doi:  
 1024 <https://doi.org/10.1121/10.0002482>
- 1025 Vorobeva, E., De Carlo, M., Le Pichon, A., Espy, P. J., & Näsholm, S. P. (2021).  
 1026 Benchmarking microbarom radiation and propagation model against infra-  
 1027 sound recordings: a vespagram-based approach. *Annales Geophysicae*, 39(3),  
 1028 515–531. doi: <https://doi.org/10.5194/angeo-39-515-2021>
- 1029 Waugh, D. W., & Polvani, L. M. (2010). Stratospheric polar vortices. In *The strato-*  
 1030 *sphere: Dynamics, transport, and chemistry* (p. 43–57). American Geophysical  
 1031 Union (AGU). doi: <https://doi.org/10.1002/9781118666630.ch3>
- 1032 Waugh, D. W., Sobel, A. H., & Polvani, L. M. (2017). What is the polar vortex and  
 1033 how does it influence weather? *Bulletin of the American Meteorological Soci-*  
 1034 *ety*, 98(1), 37–44. doi: <https://doi.org/10.1175/BAMS-D-15-00212.1>
- 1035 Waxler, R., & Assink, J. (2019). Propagation modeling through realistic atmo-  
 1036 sphere and benchmarking. In *Infrasound monitoring for atmospheric studies*  
 1037 (pp. 509–549). Springer. doi: [https://doi.org/10.1007/978-3-319-75140-5\\_15](https://doi.org/10.1007/978-3-319-75140-5_15)
- 1038 Welch, P. (1967). The use of fast fourier transform for the estimation of power spec-  
 1039 tra: a method based on time averaging over short, modified periodograms.  
 1040 *IEEE Transactions on audio and electroacoustics*, 15(2), 70–73. doi:  
 1041 [10.1109/TAU.1967.1161901](https://doi.org/10.1109/TAU.1967.1161901)
- 1042 Wicker, W., Polichtchouk, I., & Domeisen, D. I. V. (2023). Increased vertical  
 1043 resolution in the stratosphere reveals role of gravity waves after sudden  
 1044 stratospheric warmings. *Weather and Climate Dynamics*, 4(1), 81–93. doi:  
 1045 [10.5194/wcd-4-81-2023](https://doi.org/10.5194/wcd-4-81-2023)
- 1046 Zhang, J., Limpasuvan, V., Orsolini, Y. J., Espy, P. J., & Hibbins, R. E. (2021).  
 1047 Climatological westward-propagating semidiurnal tides and their composite re-  
 1048 sponse to sudden stratospheric warmings in SuperDARN and SD-WACCM-X.  
 1049 *Journal of Geophysical Research: Atmospheres*, 126(3), e2020JD032895. doi:  
 1050 <https://doi.org/10.1029/2020JD032895>